Geophysical identification, characterization, and monitoring of preferential groundwater flow paths in fractured media

by

Tanguy J. S. Robert

Civil Engineer (M.Sc. equivalent) in Mining and Geology, University of Liège, 2007

Submitted to the Department ArGEnCo on March 6, 2012

in partial fulfillment of the requirements for the degree of

Doctor of Philosophy

at the University of Liège, Belgium

Jury

Frédéric Nguyen (Supervisor)	Pr., Dr., Ir., University of Liège, Department ArGEnCo, GEO^3, Applied Geophysics
Serge Brouyère (President)	Dr., Ir., University of Liège, Department ArGEnCo, GEO^3, Hydrogeology and Environmental Geology
Frédéric Collin	Pr., Dr., Ir., University of Liège, Department ArGEnCo, GEO^3, Geomechanics and Engineering Geology
Hans-Balder Havenith	Pr., Dr., Ir., University of Liège, Department of Geology Environmental Geology
Olivier Kaufmann	Pr., Dr., Ir., University of Mons, Faculty of Engineering, Department of Fundamental and Applied Geology
René Therrien	Pr., Dr., Ir., Université Laval, Québec, Canada Géologie et Génie Géologique
Andreas Kemna	Pr., Dr., Ir., University of Bonn, Germany Steinmann-Institute, Applied Geophysics

“When in doubt, smooth”

Sir Harold Jeffreys

Abstract

This thesis investigates fractured zones leading to preferential groundwater flow paths. In this context, we used the electrical resistivity tomography (ERT) and the self-potential (SP) methods to identify, characterize, monitor, and finally model preferential flow in hydraulically-active fractured zones at a scale representative of real world applications.

From an experimental point of view, we first identified the magnitude of self-potential signature, a -15 mV anomaly that could be associated with preferential groundwater flow in a shallow quartzite aquitard whereas the streaming potential theory was originally developed for porous media. This signature was confirmed experimentally in limestone aquifers at greater depths. The joint use of surface ERT and SP allowed the identification of water-bearing fractured areas which were electrically more conductive, presenting contrasts from 1 to 10 and which were hydraulically-active presenting negative SP anomalies ranging from -10 to -30 mV. We were also able to correlate hydraulic heads and SP gradients during a low and a high groundwater level period leading to interesting perspectives in understanding the dynamics of complex groundwater flow systems. Finally, a preferential flow and rapid transport path, over 10 m/h, was highlighted in a 20 m deep fractured and karstified limestone valley by monitoring a salt tracer test with only surface ERT. This methodology was being mostly used for relatively shallow and homogeneous aquifers up to now. Such information is crucial to set up new monitoring wells or to define the sampling rates of classic tracer test.

From a methodological point of view, we quantitatively assessed the efficiency of blocky and minimum-gradient-support regularizations in electrical imaging to recover sharp interfaces on numerical benchmarks and with field data. The usefulness of resolution indicators such as the cumulative sensitivity matrix and the resolution matrix were also assessed in this context. We demonstrated that noise characterization is crucial in time-lapse inversion and may supplant the choice of the time-lapse inversion scheme, calling for a systematic analysis of reciprocal measurements (or a subset of them). We also showed that, when using data differences in an inversion scheme, the data error, as estimated by time-lapse reciprocal measurements, depends on the mean measured resistance. These error characterization studies should always be performed if one wants to avoid wrong interpretations about the hydrodynamics. We further showed that focused inversion techniques (blocky inversion, minimum-gradient-support) may offer great perspectives when recovering model changes in time-lapse inversion.

Finally, ERT and SP were jointly used to conceptualize a physically-based and spatially distributed hydrogeological model, in particular to characterize the preferential flow paths. Predicted hydraulic heads and SP-derived hydraulic heads using the water table model showed a clear correlation, leading to perspectives in terms of hydrogeological model calibration. Further experiments are however needed to fully estimate the streaming potential apparent coupling coefficient, but the use of the full SP signals for hydrogeological model calibration is a clear perspective to this work.

Biography

The author, Tanguy Robert, was born in Malmedy, Belgium in November 25, 1983. He began his studies at the University of Liège in September 2001. He obtained a Civil Engineer (M.Sc. equivalent) degree in Mining and Geology in July 2007 and began working as a Research Engineer in the Hydrogeology and Environmental Geology Group of the University of Liège in August 2007. In January 2008, he received a Grant from the F.R.I.A., a branch of the F.N.R.S, to start a Ph.D. under the supervision of Professor Frédéric Nguyen at the University of Liège in the Applied Geophysics Group.

The interest of the author to geophysics came with his work for his Master thesis where he conducted electrical resistivity tomography and self-potential surveys to locate a preferential groundwater flow path in fractured quartzites of eastern Belgium. Since then, his researches focus on the geophysical identification, characterization and monitoring of preferential groundwater flow and solute transport paths in fractured and/or karstified media. He is also interested in groundwater flow and solute transport modeling, particularly in using streaming potential signals as an additional source of groundwater flow model calibration. Another growing research topic of the author is the geophysical characterization and monitoring of landfills.

The author currently lives in Noville-les-Bois, Belgium with his wife, Catherine, his daughter, Esme, and his cat, Starbuck.

Education

- Civil Engineer (M.Sc. equivalent) in Mining and Geology, University of Liège, 2007.

Employment

- Ph.D. student, Applied Geophysics Group, University of Liège, since January 2008.
- Research Engineer in the Hydrogeology and Environmental Geology Group, University of Liège, from August 2007 to December 2007.

Awards

- Fernand Pisart mobility Grant, University of Liège, Academic year 2007-2008.
- Award of Excellence for a total immersion in Germany awarded by the German Ministry of Culture as part of the Expo 2000, July 2000.

Languages

- French and German, mother tongues
- English

Refereed Publications

- **Robert, T.**, D. Caterina, J. Deceuster, O. Kaufmann, and F. Nguyen, *A salt tracer test monitored with surface ERT to detect preferential flow and transport paths in fractured/karstified limestones*, Geophysics, 77 (2), B55-B67, 2012.
- **Robert, T.**, A. Dassargues, S. Brouyère, O. Kaufmann, V. Hallet, and F. Nguyen, *Assessing the contribution of electrical resistivity tomography (ERT) and self-potential (SP) methods for a water well drilling program in fractured/karstified limestones*, Journal of Applied Geophysics, 75 (1), 42-53, 2011.

Publications in preparation

- Caterina, D., J. Beaujean, **T. Robert**, and F. Nguyen, *Image appraisal tools for electrical resistivity tomography*, Abstract accepted for the Near Surface Geophysics Special Issue on Geotechnical Assessment and Geoenvironmental Engineering, June 2013.
- **Robert, T.**, A. Dassargues, S. Brouyère, O. Kaufmann, V. Hallet, and F. Nguyen, *Electrical properties of the Dinant Synclinorium calcareous formations*.
- Nguyen, F., A. Kemna, **T. Robert**, T. Hermans, D. Caterina, and A. Flores-Orozco, *Inversion of multi-temporal geoelectrical data sets: insights from several case studies*, Abstract submitted for the Near Surface Geophysics Special Issue on Geoelectrical Monitoring, 2012.

Conference abstracts and presentations*

- **Robert, T.***, D. Caterina, J. Deceuster, O. Kaufmann, and F. Nguyen, *A salt tracer test monitored with surface ERT to detect preferential flow and transport paths in fractured/karstified limestones*, GELMON 2011, 1st International Workshop on Geoelectrical Monitoring, Vienna, Austria, December 2, 2011.
- Nguyen, F., A. Kemna, **T. Robert***, T. Hermans, D. Caterina, and A. Flores-Orozco, *Inversion of multi-temporal geoelectrical data sets: insights from several case studies*, GELMON 2011, 1st International Workshop on Geoelectrical Monitoring, Vienna, Austria, December 1, 2011.
- Hermans, T., M. Daoudi, A. Vandenbohede, **T. Robert***, D. Caterina, and F. Nguyen, *Comparison of temperature estimates from heat transport model and electrical resistivity tomography during a shallow heat injection and storage experiment*, GELMON 2011, 1st International Workshop on Geoelectrical Monitoring, Vienna, Austria, November 30, 2011.
- **Robert, T.***, R. Therrien, J.-M. Lemieux, and F. Nguyen, *Improving groundwater flow model conceptualisation and calibration with electrical resistivity tomography and self-potential methods*, Modelcare 2011, Leipzig, Germany, September 19, 2011.
- **Robert, T.***, R. Therrien, J.-M. Lemieux, and F. Nguyen. *Improving Groundwater Flow Model Conceptualisation and Calibration with ERT and Self-potential Methods*, Near Surface 2011, 17th European Meeting of Environmental and Engineering Geophysics, Leicester, United Kingdom, September 14, 2011.
- Hermans, T., D. Caterina, R. Martin, A. Kemna, **T. Robert**, and F. Nguyen, *How to incorporate prior information in geophysical inverse problems: deterministic and geostatistical approaches*, Near Surface 2011, 17th European Meeting of Environmental and Engineering Geophysics, Leicester, United Kingdom, September 13, 2011.
- Caterina, D., J. Beaujean, **T. Robert**, and F. Nguyen, *Image appraisal tools for electrical resistivity tomography*, SAGEEP 2011, Symposium on the Application of Geophysics to Engineering and Environmental Problems, Charleston, South Carolina USA, April 12, 2011.

- **Robert, T.***, R. Therrien, J.-M. Lemieux, and F. Nguyen, *Improved automatic calibration of groundwater flow models using self-potential measurements*, 2nd International HydroGeoSphere User Conference, Hanover, Germany, April 11, 2011.
- **Robert, T.***, D. Caterina, J. Deceuster, O. Kaufmann, and F. Nguyen, *A Saline Tracer Test Monitored with ERT to Detect Preferential Flow/Transport Paths in Limestones*, Near Surface 2010, 16th European Meeting of Environmental and Engineering Geophysics, Zurich, Switzerland, September 7, 2010.
- **Robert, T.***, A. Dassargues, and F. Nguyen, *Electrical resistivity tomography and self-potential case studies for fractured aquifer characterization and monitoring*, EGU General Assembly 2010, Vienna, Austria, May 4, 2010.
- Caterina, D., J. Beaujean, **T. Robert**, and F. Nguyen, *Image Appraisal Tools for Electrical Resistivity Tomography*, Poster, Ph.D. Student Day ENVITAM and UNITER Graduate Schools, Namur, Belgium, January 12, 2010.
- **Robert, T.***, and F. Nguyen, *Electrical resistivity tomography and self-potential methods as a tool for fractured aquifer characterization and monitoring*, Poster, Ph.D. Student Day ENVITAM and UNITER Graduate Schools, Namur, Belgium, January 12, 2010.
- **Robert, T.***, A. Dassargues, S. Brouyère, O. Kaufmann, V. Hallet, and F. Nguyen, *Using Electrical Resistivity Tomography and Self-potential Methods for Wells Implementations in Fractured Limestones*, Near Surface 2011, 15th European Meeting of Environmental and Engineering Geophysics, Dublin, Ireland, September 9, 2009.
- **Robert, T.***, *Détection de cavités et de racines d'altération par tomographie électrique*, Journées de Spéléologie Scientifique, Han-sur-Lesse, Belgium, November 15, 2008.

Reports

- Brouyère, S., J. Gesels, P. Goderniaux, P. Jamin, **T. Robert**, L. Thomas, A. Dassargues, J. Bastien, F. Vanwittenberge, A. Rorive, F. Dossin, J.-L. Lacour, D. Le Madec, P. Nogarède, and V. Hallet, Caractérisation hydrogéologique et support à la mise en œuvre de la Directive Européenne 2000/60 sur les masses d'eau souterraine en Région Wallonne (Projet Synclin'EAU), *délivrable D.3.12 - partie RWM021*, Convention RW et SPGE-Aquapole (in French), 2009.

- Brouyère, S., J. Gesels, P. Goderniaux, P. Jamin, **T. Robert**, L. Thomas, A. Dassargues, J. Bastien, F. Vanwittenberge, A. Rorive, F. Dossin, J.-L. Lacour, D. Le Madec, P. Nogarède, and V. Hallet, Caractérisation hydrogéologique et support à la mise en œuvre de la Directive Européenne 2000/60 sur les masses d'eau souterraine en Région Wallonne (Projet Synclin'EAU), *délivrable D.3.12 - partie RWM011*, Convention RW et SPGE-Aquapole (in French), 2009.
- Brouyère, S., J. Gesels, P. Goderniaux, P. Jamin, **T. Robert**, L. Thomas, A. Dassargues, J. Bastien, F. Vanwittenberge, A. Rorive, F. Dossin, J.-L. Lacour, D. Le Madec, P. Nogarède, and V. Hallet, Caractérisation hydrogéologique et support à la mise en œuvre de la Directive Européenne 2000/60 sur les masses d'eau souterraine en Région Wallonne (Projet Synclin'EAU), *délivrable D.3.12 - partie RWM012*, Convention RW et SPGE-Aquapole (in French), 2009.
- Brouyère, S., J. Gesels, P. Goderniaux, P. Jamin, **T. Robert**, L. Thomas, A. Dassargues, J. Bastien, F. Vanwittenberge, A. Rorive, F. Dossin, J.-L. Lacour, D. Le Madec, P. Nogarède, and V. Hallet, *délivrable D.3.52 et D.4.5 - Rapport sur les interactions avec les eaux de surface (volet quantitatif et qualitatif)*, Convention RW et SPGE-Aquapôle (in French), 2009.
- **Robert, T.**, and F. Nguyen, *Rapport des prospections géophysiques sur le site de Châtelet*, Projet PolluSol2 (in French), 2009.
- Brouyère, S., J. Gesels, P. Goderniaux, P. Jamin, **T. Robert**, L. Thomas, A. Dassargues, J. Bastien, F. Vanwittenberge, A. Rorive, F. Dossin, J.-L. Lacour, D. Le Madec, P. Nogarède, and V. Hallet, Caractérisation hydrogéologique et support à la mise en œuvre de la Directive Européenne 2000/60 sur les masses d'eau souterraine en Région Wallonne (Projet Synclin'EAU), *délivrable D.4.1 - Rapport relatif aux échantillonnages complémentaires des éléments majeurs*, Convention RW et SPGE-Aquapole (in French), 2008.
- Nguyen, F., and **T. Robert**, Caractérisation hydrogéologique et support à la mise en œuvre de la Directive Européenne 2000/60 sur les masses d'eau souterraine en Région Wallonne (Projet Synclin'EAU), *Rapport des prospections géophysiques*, Convention RW et SPGE-Aquapole (in French), 2007.

Acknowledgements

The first years of my University path as a Civil Engineer student were not easy. I was maybe too young – 17 years old – when I started or not mature enough. However, I was able to move forward with the help and support of my family and future wife that I know now for more than 10 years. I would like to thank them because without them, I would not be who and where I am now.

I first met Frédéric in 2007 when he taught us inverse modeling. He just arrived at the University of Liège as a Professor. I asked him to perform some geophysics in a site I was investigating for my Master Thesis work. The results of this study – presented in this dissertation – were very encouraging and I was very happy of this personal initiative. I believe that Frédéric was quite happy too since he asked me if I was interested in a Ph.D. I would like to thank him for giving me this opportunity but also for his availability from the early beginning of this work to the very end of it.

Before starting this Ph.D., we had to find the funds… Here, I would like to thank Alain Dassargues and Serge Brouyère for hiring me in the Hydrogeology Group some months. I spent a lot of time doing fieldworks on this Synclin’Eau project, especially with Julie and Laurent. Thanks to them, I know now the Hoyoux and Samson valleys really well, especially the locations of small restaurants, or of the cheese factory… Both valleys are so splendid that I now often go cycling there.

During the time I was on the Synclin’Eau project, I applied to the F.R.I.A. Grant which I obtained and I could finally start my Ph.D. in January 2008. I would like to thank the F.R.I.A. and the jury of the commission for giving me this chance. I would also like to thank Aquale and G-Tec for their support with the F.R.I.A. project.

This work would not have been possible without the support and help of all my colleagues from GEO^3. A lot of you – as well as students – spent time with me on fieldworks and when I remember all the geophysical surveys I conducted for the Synclin’Eau project or for this salt tracer test where I had to sleep in a car in the middle of nowhere during the cold nights of winter… well, I would just like to thank you for being there when I most needed it. I must also say that it was – and I hope it will still be – a pleasure to work in such nice conditions.

I also had the chance to spend three great months in Québec, Canada in the team of René Therrien at Université Laval. I was there with my wife and daughter and also with Sam and Audrey. We had such a great time, even with the cold, and if the opportunity arises again, I'll jump on it. There, I met "La famille" and we spent a lot of good time together. Tobias gave me his recipe for his amazing Blitz Schokoladen Kuchen, Jalil made me laugh so often, Jillaume introduced me to local beers, and I took a lot of pleasure speaking with Fabien which is a fan of cycling just like me. Sam was often conspiring with the others to make jokes and I must say that I was sometimes a really easy target. I also discovered the traditional Quebecois dish "La Poutine" which I missed since my return in Belgium. I would like to thank René, Jean-Michel, and their both families for lending me all the babies' stuff I needed. I hope Esme did not drool too much on Flavie's toys ;-).

With the encouragements of Frédéric, I travelled a lot to present my research. Dublin, Québec, Zürich, Leicester, Leipzig, Vienna, and Bonn were very nice destinations and I hope that in the future, I will be able to continue traveling around the world. In all these conferences, I met a lot of great people and I'm looking forward for seeing them in the next conferences or workshops. With all these presentations I've made but also with the doctoral courses I attended, I improved a lot of my skills including English, writing, and effective communication which are now very helpful in all parts of my life.

This Thesis took a lot of a time in my life but I'm very pleased that I was still able to move forward in my personal life. As an example, we moved in our new house two months ago. Since the start of the Ph.D., we got a cat which was named Starbuck after the character of Kara Thrace in Battlestar Galactica. Then, I got married with Catherine. We decided very early to have a baby and I was filled with joy when she announced me that she was finally pregnant after almost 2 years of waiting. The whole pregnancy went very well and finally, our little Esme was born on June 13, 2010. It was – and still is – one of the best days of my life.

Table of contents

1. Introduction 17
    1.1. Problem outline and motivation 17
    1.2. State of the art 18
    1.3. Objectives of this thesis 20
    1.4. Organization of the manuscript 20
2. Electrical resistivity tomography 27
    2.1. Principles 27
    2.2. Electrode configuration 28
    2.3. Data acquisition and associated issues 29
    2.4. Inversion 32
        2.4.1. Objective function 34
        2.4.2. Data misfit 34
        2.4.3. Model constraint 36
        2.4.4. Image appraisal 38
        2.4.5. Time-lapse inversion 41
3. Self-potential 51
    3.1. Theory and principles 51
    3.2. Streaming potential 53
    3.3. Data acquisition and associated issues 56
4. Studied sites in the Dinant Synclinorium 65
    4.1. Physical background 65
    4.2. Geological background 66
    4.3. Hydrogeological background 68
        4.3.1. Flow properties 70
        4.3.2. Transport properties 71
    4.4. Groundwater geochemistry 72
        4.4.1. The Carboniferous limestone aquifers 72
        4.4.2. The late Famennian sandstone aquifers 73
    4.5. The Stavelot Massif 74

5.1. Geoelectrical signatures of a preferential flow path in fractures 89
  5.1.1. Introduction 89
  5.1.2. Methods 90
  5.1.3. Results 91
  5.1.4. Conclusions 91
5.2. Outcrops analysis 95
5.3. Joint interpretation of ERT and SP data for well positioning 102
5.4. Comparison of different model constraints in DC electrical data inversion for the characterization of fractured aquifers 103
  5.4.1. The synthetic case study 104
  5.4.2. The real case study 107
6. Characterization and monitoring 123
6.1. ERT and SP monitoring of seasonal variations of hydraulic gradients 124
6.2. A salt tracer test monitored with surface ERT 139
6.3. Groundwater flow direction from an SP map 141
6.4. Time-lapse noise characterization and comparison of different time-lapse strategies 143
  6.4.1. Background resistivity model 144
  6.4.2. Time-lapse data error characterization 145
  6.4.3. Time-lapse inversion results using resistances as data 146
  6.4.4. Time-lapse inversion results using resistances differences as data 147
7. Modeling flow 159
7.1. Model conceptualization 160
7.2. Model precalibration using geophysical and hydrogeological data 162
8. Conclusions and perspectives 179

1. Introduction

1.1. Problem outline and motivation

Groundwater systems globally provide 25 to 40% of the world's drinking water (UNO 2nd world water development report, 2006) and water supply is expected to become a crucial issue in many regions, including ours. Fractured media constitute adequate drinking water exploitation areas because they can enhance well productivity. However, they also lead to potential contamination paths because groundwater flow and solute transport are channeled through them. Preferential flow and transport also play a major role in many other contexts (Berkowitz, 2002) such as petroleum reservoir exploitation, geothermal reservoir exploitation and heat storage, or mining and mineralization processes (in situ leaching and location of ore bodies). From a hydrogeological point of view, the identification and characterization of more fractured areas in hard rock aquifers are major issues (e.g., Michalski and Britton, 1997; Berkowitz, 2002; Eaton, 2006) in understanding those complex systems and to propose reliable predictions.

To build conceptual flow and transport models, hydrogeologists often rely on scarce data, compared to the modeled area and heterogeneity, and on their expertise including prior knowledge about fractures. However, as argued by several authors (e.g., Berkowitz, 2002; Eaton, 2006), such approaches largely rely on extrapolation and subjective considerations which in turn might impact interpretation.

The work presented in this thesis focus on bringing relevant information using geophysical methods for the hydrogeological modeling of fractured aquifers. The following subsection briefly overview the different methods existing to characterize fractures in aquifers.

1.2. State of the art

Sources of fractures information go from core samples (laboratory scale) to aerial photographs or satellite images (large basin scale). Between these two diametrically opposed scales, one can also use geological outcrops, hydrogeological pumping and tracer tests, and geophysics (which can be multi-scale) in order to infer hydrogeological properties about fractured areas. Geological outcrops allow direct observations and measurements of the fractures network (e.g., length, spacing, aperture, and orientation) (e.g., Hancock, 1985; Hurst and Rosvoll, 1991; Davis et al., 2006; Lemieux et al., 2006; 2009) but they are only partially and locally representative of the subsurface (e.g., Eaton, 2006). Moreover, geological outcrops are often scarce if not missing in many regions, including the ones investigated in this work.

Boreholes information coming, for example, from core samples often constitutes the only alternative to visualize the subsurface. However, compared to outcrops, core samples are much more local and at the scale of the watershed, they are not representative. Moreover, due to logistical and financial constraints, drillings are not always possible everywhere.

Aerial photographs, topographical maps, teledetection, and satellite images can provide a wide amount of information for extrapolating some geological features such as fractures or giving the general orientations of the main fractures (e.g., Parsons and Yearley, 1986; Karimoune et al., 1990; Crippen and Blom, 1992; Massonet et al., 1993; Clark and Wilson, 1994; Calais et al., 2008; Poncelet and Cornet, 2010). However, they lack in-depth information.

When boreholes are present, authors often try to quantify geological information in terms of hydrodynamic properties (e.g., Setterholm et al., 1991; Muldoon et al., 2001; Runkel et al., 2006; Lemieux et al., 2006) by conducting, for example, pumping tests, tracer tests, and connectivity tests (e.g., Novakowski et al., 1985; Paillet, 1998; Mauldon, 1998; Odling et al., 1999; Berkowitz et al., 2000; Bonnet et al., 2001; Sanford et al., 2002; Le Borgne et al., 2004; 2006a; 2006b; Illman and Tartakovsky, 2006; Hao et al., 2008; Blessent et al., 2011). These are mostly realized at very local scales, except maybe for some tracer tests (e.g., Brouyère et al., 2009a, b, and c) and are moreover limited in number, given the costs of new drillings.

In the past decade, the use of geophysics as a complementary tool to characterize fractures or fractured areas has been increasingly growing with geophysical methods including seismic, DC resistivity, electromagnetic, ground penetrating radar, and self-potential (e.g., Day-Lewis et al., 2003; Krishnamurthy et al., 2003; Porsani et al., 2005; Rozycki et al., 2006; Vasconcelos and Grechka, 2007; Yadav and Singh, 2007; Suski et al., 2008; Wishart et al., 2006; 2008; 2009; Dorn et al., 2012; Robert et al., 2011; 2012). Geophysical methods have the advantage of being integrative and non-invasive while providing in-depth information. However, they are indirect information subject to larger uncertainties than hard data such as boreholes or outcrops. More recently, there is an increasing interest in using geophysical data to directly constrain predictions of hydrogeological model (e.g., Titov et al., 2005; Jardani et al., 2007; Straface et al., 2007; Bolève et al., 2009; Jardani and Revil, 2009) or to target directly the desired hydrogeological properties (e.g., Börner et al., 1996; Legchenko et al., 2002; Vouillamoz et al., 2002; Kemna et al., 2004; Boucher et al., 2006; Girard et al., 2007; Hördt et al., 2007; Legchenko et al., 2008).

Among the possible geophysical methods, we focused in this work on two geo-electrical methods, the electrical resistivity tomography (ERT) and the self-potential (SP) methods. ERT allows mapping contrasts of electrical resistivity of the subsurface (e.g., Sasaki, 1994) that can be interpreted in terms of hydrogeological facies (e.g., Vereecken et al., 2006). Indeed, water-bearing fractured areas are expected to have greater electrical conductivity than the host rock. SP can further allow the discrimination of the fractures content (e.g., clay or water) since it is sensitive to groundwater flow (e.g., Corwin and Hoover, 1979; Sill, 1983; Fournier, 1989; Aubert and Atangana, 1996; Revil et al., 1999; Revil et al., 2005). These methods also offer the possibility to monitor subsurface processes at the scale of a watershed which is more difficult to achieve with geophysical methods such as the ground-penetrating radar which is generally used in ideal conditions (i.e., a resistive soil) and at a lower scale (e.g., Day-Lewis et al., 2003; Doetsch et al., 2012). This is almost impossible to achieve with methods such as seismic (i.e., for hydrogeological purpose) or electromagnetic given the scale and resolution. To our knowledge, there are few to no references using electromagnetic at the watershed scale for monitoring purpose.

1.3. Objectives of this thesis

The objective of this thesis was to contribute in the characterization of fractured aquifers using DC electrical resistivity tomography and self-potential with a view to constrain hydrogeological models at a scale relevant of real world applications. This was achieved through the development of electrical resistivity tomography for the static and dynamic characterization of fractured areas and through the development of self-potential which is directly sensitive to fluxes within those fractured areas.

1.4. Organization of the manuscript

Past the present introduction (**chapter 1**), we first present the electrical resistivity tomography method (**chapter 2**) and the self-potential technique (**chapter 3**) that are used throughout the thesis.

Then, we focus on the presentation of the investigated sites, located both in Belgium, in the Stavelot Massif and in the Dinant Synclinorium, in terms of geological, hydrogeological, and physico-chemical backgrounds (**chapter 4).**

In **chapter 5**, we will first identify the geoelectrical signatures of preferential groundwater flow paths (section 5.1). Then, we will assess the contribution of the joint use of ERT and SP in a drilling program (section 5.3 published in Journal of Applied Geophysics, 75 (1), 42-53, 2011) and we will present a comparative study on image appraisal tools and model constraints for fractured aquifer characterization.

Chapter 6 is related to the monitoring of natural (section 6.1) and forced (section 6.2, published in Geophysics, 77 (2) B55-B67, 2012) subsurface processes with SP and ERT, respectively, whereas section 6.3 presents the results of an SP mapping validating the groundwater flow direction found in section 6.2. We will close this chapter by presenting a comparative study on time-lapse inversion strategies, focusing on data error characterization.

Chapter 7 integrates the geophysical information to conceptualize and then precalibrate a groundwater flow model of a calcareous valley. Conclusions and perspectives are finally presented in **chapter 8**.

References

Aubert, M., and Q. Y. Atangana, 1996, *Self-Potential Method in Hydrogeological Exploration of Volcanic Areas*, Ground Water, 34 (6), 1010-1016.

Berkowitz, B., O. Bour, P. Davy, and N. Odling, 2000, *Scaling of fracture connectivity in geological formations*, Geophysical Research Letters, 27 (14), 2061–2064.

Berkowitz, B., 2002, *Characterizing flow and transport in fractured geological media: A review*, Advances in Water Resources, 25 (8-12), 861-884.

Blessent, D., R. Therrien, and J.-M. Lemieux, 2011, *Inverse modeling of hydraulic tests in fractured crystalline rock based on a transition probability geostatistical approach*, Water Resources Research, 47 (12), W12530, doi:10.1029/2011WR011037.

Bolève, A., A. Revil, F. Janod, J. L. Mattiuzzo, and J. J. Fry, 2009, *Preferential fluid flow pathways in embankment dams imaged by self-potential tomography*, Near Surface Geophysics, 7 (5-6), 447-462.

Bonnet, E., O. Bour, N. E. Odling, P. Davy, I. Main, P. Cowie, and B. Berkowitz, 2001, *Scaling of fracture systems in geological media*, Review of Geophysics, 39 (3), 347–383.

Börner, F.D., J. R. Schopper, and A. Weller, 1996, *Evaluation of transport and storage properties in the soil and groundwater zone from induced polarization measurements*, Geophysical Prospecting, 44 (4), 583-601.

Boucher, M., J. F. Girard, A. Legchenko, J. M. Baltassat, N. Dörfliger, and K. Chalikakis, 2006, *Using 2D inversion of magnetic resonance soundings to locate a water-filled karst conduit*, Journal of Hydrology, 330 (3-4), 413-421.

Brouyère, S., J. Gesels, P. Goderniaux, P. Jamin, T. Robert, L. Thomas, A. Dassargues, J. Bastien, F. Vanwittenberge, A. Rorive, F. Dossin, J.-L. Lacour, D. Le Madec, P. Nogarède, and V. Hallet, 2009a, Caractérisation hydrogéologique et support à la mise en œuvre de la Directive Européenne 2000/60 sur les masses d'eau souterraine en Région Wallonne (Projet Synclin'EAU), *délivrable D.3.12 - partie RWM021*, Convention RW et SPGE-Aquapole (in French).

Brouyère, S., J. Gesels, P. Goderniaux, P. Jamin, T. Robert, L. Thomas, A. Dassargues, J. Bastien, F. Vanwittenberge, A. Rorive, F. Dossin, J.-L. Lacour, D. Le Madec, P. Nogarède, and V. Hallet, 2009b, Caractérisation hydrogéologique et support à la mise en œuvre de la Directive Européenne 2000/60 sur les masses d'eau souterraine en Région Wallonne (Projet Synclin'EAU), *délivrable D.3.12 - partie RWM011*, Convention RW et SPGE-Aquapole (in French).

Brouyère, S., J. Gesels, P. Goderniaux, P. Jamin, T. Robert, L. Thomas, A. Dassargues, J. Bastien, F. Vanwittenberge, A. Rorive, F. Dossin, J.-L. Lacour, D. Le Madec, P. Nogarède, and V. Hallet, 2009c, Caractérisation hydrogéologique et support à la mise en œuvre de la Directive Européenne 2000/60 sur les masses d'eau souterraine en Région Wallonne (Projet Synclin'EAU), *délivrable D.3.12 - partie RWM012*, Convention RW et SPGE-Aquapole (in French).

Calais, E., N. d'Oreye, J. Albaric, A. Deschamps, D. Delvaux, J. Déverchère, C. Ebinger, Richard W. Ferdinand, F. Kervyn, A. S. Macheyeki, A. Oyen, J. Perrot, E. Saria, B. Smets, S. Stamps and C. Wauthier, 2008, *Strain accommodation by slow slip and dyking in a youthful continental rift, East Africa*, Nature, 456, doi:10.1038/nature07478.

Clark, C. D. and C. Wilson, 1994, *Spatial analysis of lineaments*, Computers et Geosciences, 20 (7-8), 1237-1258.

Crippen, R. E. and R. G. Blom, 1992, *The first visual observations of fault movements from space – the 1992 Landers earthquake*, EOS, Transactions of the American Geophysical Union, 73, 364.

Corwin, R. F., and D. B. Hoover, 1979, *The self-potential method in geothermal exploration*, Geophysics, 44 (2), 226-245.

Davis, J. M., N. D. Roy, P. S. Mozley, and J. S. Hall, 2006, *The effect of carbonate cementation on permeability heterogeneity in fluvial aquifers: An outcrop analog study*, Sedimentary Geology, 184 (3-4), 267-280.

Day-Lewis, F. D., J. W. Lane, Jr., J. M. Harris, and S. M. Gorelick, 2003, *Time-lapse imaging of saline-tracer transport in fractured rock using difference-attenuation radar tomography*, Water Resources Research, 39 (10), 1290, doi:10.1029/2002WR001722.

Doetsch, J., N. Linde, M. Pessognelli, A.G. Green, and T. Guenther, 2012, *Constraining 3-D electrical resistance tomography with GPR reflection data for improved aquifer characterization*, Journal of Applied Geophysics, 78, 68-76.

Dorn, C., N. Linde, J. Doetsch, T. Le Borgne, and O. Bour, 2012, Fracture imaging within a granitic rock aquifer using multiple-offset single-hole and cross-hole GPR reflection data, Journal of Applied Geophysics, 78, 123-132.

Eaton, T. T., 2006, *On the importance of geological heterogeneity for flow simulation*, Sedimentary Geology, 184 (3-4), 187-201.

Fournier, C., 1989, *Spontaneous potentials and resistivity surveys applied to hydrogeology in a volcanic area: case history of the Chaîne des Puys (Puy-de-Dôme, France)*, Geophysical Prospecting, 37 (6), 647-668.

Girard, J. F., M. Boucher, A. Legchenko, and J. M. Baltassat, 2007, *2D magnetic resonance tomography applied to karstic conduit imaging*, Journal of Applied Geophysics, 63 (3-4), 103-116.

Hancock, P. L., 1985, *Brittle microtectonics: principles and practice*, Journal of Structural Geology, 7 (3-4), 437-457.

Hao, Y., T.-C. J. Yeh, J. Xiang, W. A. Illman, K. Ando, K.-C. Hsu, and C.-H. Lee, 2008, *Hydraulic Tomography for Detecting Fracture Zone Connectivity*, Ground Water, 46 (2), 183-192.

Hördt, A., R. Blaschek, A. Kemna, and N. Zisser, 2007, *Hydraulic conductivity estimation from induced polarisation data at the field scale - the Krauthausen case history*, Journal of Applied Geophysics, 62 (1), 33-46.

Hurst A. and K. Rosvoll, 1991, *Permeability variations in sandstones and their relationship to sedimentary structures*, In: Lake L. W., Carroll H. B. Jr. and Wesson T. C. (Ed.), Reservoir Characterisation II, Academic Press, San Diego, California, 166-196.

Illman, W. A., and D. M. Tartakovsky, 2006, *Asymptotic Analysis of Cross-Hole Hydraulic Tests in Fractured Granite*, Ground Water, 44 (4), 555-563.

Jardani, A., A. Revil, A. Bolève, A. Crespy, J.-P. Dupont, W. Barrash, and B. Malama, 2007, *Tomography of the Darcy velocity from self-potential measurements*, Geophysical Research Letters, 34, L24403, doi:10.1029/2007GL031907.

Jardani, A., and A. Revil, 2009, *Stochastic joint inversion of temperature and self-potential data*, Geophysical Journal International, 179 (1), 640-654.

Karimoune, S., A. Ozer, and M. Erpicum, 1990, *Les modelés éoliens de la région de Zinder (Niger méridional): Etude de photo-géomorphologie. Note préliminaire. Apports de la télédétection à la lutte contre la sécheresse*, Coll. Actualité Scientifique Univ. Francophones, Ed. AUPELF-UREF, J. Libbey Eurotext, Paris, 145-161.

Kemna, A., A. M. Binley, and L. Slater, 2004, *Cross-borehole IP imaging for engineering and environmental applications*, Geophysics, 69 (1), 97-105.

Krishnamurthy, N. S., D. Kumar, V. Ananda Rao, S. C. Jain, and S. Ahmed, 2003, *Comparison of surface and sub-surface geophysical investigations in delineating fracture zones*, Current Science, 84 (9), 1242-1246.

Le Borgne T., O Bour., J-R. De Dreuzy, P. Davy, and F. Touchard, 2004, *Equivalent mean flow models relevant for fractured aquifers: Insights from a pumping tests scaling interpretation*, Water Resources Research, 40, WO5112, doi:10.1029/2003WR002436.

Le Borgne T., O. Bour, F. L. Paillet, and J-P. Caudal, 2006a, *Assessment of preferential flow path connectivity and hydraulic properties at single-borehole and cross-borehole scales in a fractured aquifer*, Journal of Hydrology, 328 (1-2), 347-359.

Le Borgne, T., F. Paillet, L, O. Bour, and J-P. Caudal, 2006b, Cross borehole flowmeter tests for transient heads in heterogeneous aquifers, Ground Water, 44 (3), 444-452.

Legchenko, A., J.-M. Baltassat, A. Beauce, and J. Bernard, 2002, *Nuclear magnetic resonance as a geophysical tool for hydrogeologists*, Journal of Applied Geophysics, 50 (1-2), 21-46.

Legchenko, A., M. Ezersky, J. F. Girard, J. M. Baltassat, M. Boucher, C. Camerlynck, and A. Al-Zoubi, 2008, *Interpretation of magnetic resonance soundings in rocks with high electrical conductivity*, Journal of Applied Geophysics, 66 (3-4), 118-127.

Lemieux, J.-M., R. Therrien, and D. Kirkwood, 2006, *Small scale study of groundwater flow in a fractured carbonate-rock aquifer at the St-Eustache quarry, Québec, Canada*, Hydrogeology Journal, 14 (4), 603-612.

Lemieux, J.-M., D. Kirkwood, and R. Therrien, 2009, *Fracture network analysis of the St-Eustache quarry, Quebec, Canada, for groundwater resources management*, Canadian Geotechnical Journal, 46 (7), 828-841.

Massonnet, D., M. Rossi, C. Carmona, F. Adragna, G. Peltzer, K. Feigl, and T. Rabaute, 1993, *The displacement field of the Landers earthquake mapped by radar interferometry*, Nature, 364, 138-142.

Mauldon M., 1998, *Estimating mean fracture trace length and density from observations in convex windows*, Rock Mechanics and Rock Engineering, 31 (4), 201-216.

Michalski A. and R. Britton, 1997, *The role of bedding planes in the hydrogeology of sedimentary bedrock - evidence from the Newark Basin*, New Jersey, Ground Water 35 (2), 318-327.

Muldoon M. A., J. A. Simo and K. R. Bradbury, 2001, *Correlation of hydraulic conductivity with stratigraphy in a fractured-dolomite aquifer, northeastern Wisconsin, USA*, Hydrogeology Journal, 9 (6), 570-583.

Odling N. E., P. Gillespie, B. Bourgine, C. Castaing, J.-P. Chiles, N. P. Christensen, E. Fillion, A. Genter, C. Olsen, L. Thrane, R. Trice, E. Aarseth, J. J. Walsh, and J. Watterson, 1999, *Variations in fracture system geometry and their implications for fluid flow in fractured hydrocarbon reservoirs*, Petroleum Geoscience, 5, 373-384.

Novakowski K. S., G. B. Evans, D. A. Lever, and K. G. Raven, 1985, *A field example of measuring hydrodynamic dispersion in a single fracture*, Water Resources Research, 21 (8), 1165-1174.

Paillet F., 1998, *Flow modelling and permeability estimation using borehole flow logs in heterogeneous fractured formations*, Water Resources Research, 34 (5), 997-1010.

Parsons, A. J. and R. J. Yearley, 1986, *An analysis of geologic lineaments seen on LANDSAT MSS imagery*, International Journal of Remote Sensing, 7 (12), 1773-1782.

Poncelet, N. and Y. Cornet, 2010, *Transformée de Hough et détection de linéaments sur images satellitaires et modèles numériques de terrain*, Bulletin de la Société Géographique de Liège, 54, 145-156.

Porsani, J. L., V. R. Elis, and F. Y. Hiodo, 2005, *Geophysical investigations for the characterization of fractured rock aquifers in Itu, SE Brazil*, Journal of Applied Geophysics, 57 (2), 119-128.

Revil, A., P. A. Pezard, and P. W. J. Glover, 1999, *Streaming potential in porous media. 1. Theory of the zeta potential*, Journal of Geophysical Research, 104(B9), 20021-20031, doi:10.1029/1999JB900089.

Revil, A., P. Leroy, and K. Titov, 2005, *Characterization of transport properties of argillaceous sediments: Application to the Callovo-Oxfordian argillite*, Journal of Geophysical Research, 110 (B6), B06202, doi:10.1029/2004JB003442.

Robert, T., A. Dassargues, S. Brouyère, O. Kaufmann, V. Hallet, and F. Nguyen, 2011, *Assessing the contribution of electrical resistivity tomography (ERT) and self-potential (SP) methods for a water well drilling program in fractured/karstified limestones*, Journal of Applied Geophysics, 75 (1), 42-53.

Robert, T., D. Caterina, J. Deceuster, O. Kaufmann, and F. Nguyen, 2012, *A salt tracer test monitored with surface ERT to detect preferential flow and transport paths in fractured/karstified limestones*, Geophysics, 77 (2), B55-B67.

Rozycki, A., J. M. Ruiz Fonticiella, and A. Cuadra, 2006, *Detection and evaluation of horizontal fractures in earth dams using the self-potential method*, Engineering Geology, 82 (3), 145-153.

Runkel, A. C., R. G. Tipping, E. C. Alexander Jr, and S. C. Alexander, 2006, *Hydrostratigraphic characterization of intergranular and secondary porosity in part of the Cambrian sandstone aquifer system of the cratonic interior of North America: Improving predictability of hydrogeologic properties*, Sedimentary Geology, 184 (3-4), 281-304.

Sanford W. E., P. G. Cook, and J. C. Dighton, 2002, *Analysis of a vertical dipole tracer test in highly fractured rock*, Ground Water, 40 (5), 535-542.

Sasaki, Y., 1994, *3-D resistivity inversion using the finite-element method*, Geophysics, 59 (12), 1839-1848.

Setterholm D. R., A. C. Runkel, J. M. Cleland, R. G. Tipping, J. M. Mossler, R. Kanivetsky, and H. C. Hobbs, 1991, *Geologic factors affecting the sensitivity of the Prairie du Chien-Jordan aquifer*, Minnesota Geological Survey Open-File Report 91-5, 29 pp.

Sill, W. R., 1983, Self-potential modeling from primary flows, Geophysics, 48 (1), 76-86.

Straface, S., F. Carmine, S. Troisi, E. Rizzo, and A. Revil, 2007, An Inverse Procedure to Estimate Transmissivity from Heads and SP Signals, Ground Water, 45 (4), 420-428.

Suski, B., F. Ladner, L. Baron, F. D. Vuataz, F. Philippossian, and K. Holliger, 2008, *Detection and characterization of hydraulically active fractures in a carbonate aquifer: results from self-*

potential, temperature and fluid electrical conductivity logging in the Combioula hydrothermal system in the southwestern Swiss Alps, Hydrogeology Journal, 16 (7), 1319-1328.

Titov, K. V., A. Levitski, P. K. Konosavski, A. V. Tarasov, Y. T. Ilyin, and M. A. Bues, 2005, *Combined application of surface geoelectrical methods for groundwater-flow modeling: A case history*, Geophysics, 70 (5), H21-31.

Vasconcelos, I., and V. Grechka, 2007, Seismic characterization of multiple fracture sets at Rulison Field, Colorado, Geophysics, 72 (2), B19-B30.

Vereecken H., A. Binley, G. Cassiani, A. Revil, and K. Titov, 2006, *Applied Hydrogeophysics*, Nato Science Series, IV Earth and Environmental Sciences, 71, Springer.

Vouillamoz, J.-M., M. Descloitres, J. Bernard, P. Fourcassier, and L. Romagny, 2002, *Application of integrated magnetic resonance sounding and resistivity methods for borehole implementation. A case study in Cambodia*, Journal of Applied Geophysics, 50 (1-2), 67-81.

Wishart, D. N., L. D. Slater, and A. E. Gates, 2006, *Self potential improves characterization of hydraulically-active fractures from azimuthal geoelectrical measurements*, Geophysical Research Letters, 33 (17), L17314, doi:10.1029/2006GL027092.

Wishart, D. N., L. D. Slater, and A. E. Gates, 2008, *Fracture anisotropy characterization in crystalline bedrock using field-scale azimuthal self potential gradient*, Journal of Hydrology, 358 (1-2), 35-45.

Wishart, D. N., L. D. Slater, D. L. Schnell, and G. C. Herman, 2009, *Hydraulic anisotropy characterization of pneumatic-fractured sediments using azimuthal self potential gradient*, Journal of Contaminant Hydrology, 103 (3-4), 134-144.

Yadav, G. S., and S. K. Singh, 2007, *Integrated resistivity surveys for delineation of fractures for ground water exploration in hard rock areas*, Journal of Applied Geophysics, 62 (3), 301-312.

2. Electrical resistivity tomography

2.1. Principles

Electrical resistivity tomography (ERT) is a method used to image the bulk electrical resistivity distribution of the subsurface. The electrical resistivity is an intrinsic property of material that can be used to infer subsurface properties. An in-depth review of electrical properties of rocks can be found in Guéguen and Palciauskas (1994) or Schön (2004) whereas a full description of electrical methods can be found in Telford et al. (1990) and Ward (1990).

In a wide range of geological situations, water-bearing rocks or sediments can be considered as a saturated or partly saturated porous media where the electrical conduction is mainly realized thanks to the movement of dissolved ions subject to an electrical field. However, when clayey materials are present, another type of conduction also plays a role and it is related to the surface conductivity of minerals. For completeness, a third type of conduction (electronic conduction) which involves electrons can be observed in areas with minerals such as sulfides, oxides or graphite. In most cases, this type of conduction can be neglected, except in areas where such mineralization occurred (pyrite for example).

Electrical resistivity of rocks or sediments depends on several parameters. The water content of the medium is an important parameter since the electrical conduction is mainly electrolytic. Therefore, porosity which can be increased with fractures and karsts, and water saturation are important parameters in the electrical conduction in sedimentary rocks. The electrical resistivity of groundwater which depends on the total amount of dissolved solids (named hereafter TDS) plays an important role as the presence or absence of clay minerals in the investigated rocks.

Acquiring one ERT data requires injecting a known electrical current into the soil by imposing a known electrical potential difference between two electrodes connected to the ground and measuring the resulting electrical potential distribution at another pair of electrodes. Two pairs of electrodes called current and potential electrodes are used for this.

Given Ohm’s law, a value of electrical resistance is calculated and assigned to the specific quadripole of electrodes (current and potential electrodes) that was used for the acquisition. This process is repeated automatically a large number (typically hundreds to thousands) of times to acquire a complete data set of electrical resistances (typically up to a thousand data points for a profile with 64 electrodes).

The electrical resistance is not an intrinsic property of the subsurface since it depends on the whole volume that is crossed by the electrical current lines. The intrinsic property which is the electrical resistivity is obtained by inverting the resistances.

2.2. Electrode configuration

Every ERT data is associated with a particular configuration of electrodes also known as an electrode array. Among the different possible configurations, we used the Wenner Alpha, the Wenner Schlumberger and the dipole-dipole arrays which are all four active electrodes arrays (Figure 2.1). The resolving power and the limitations of the different configurations can be found in Athanasiou et al. (2007), Dahlin and Zhou (2004), and Stummer et al. (2004), for example.

The Wenner Alpha array is known for its good signal-to-noise ratio and is therefore often used for its robustness. This configuration of electrodes offers a good vertical resolution (i.e., horizontal structures) whereas it has a poor lateral or horizontal resolution (i.e., vertical structures). This means that this array is suitable to image horizontal structures for example in layered aquifers or to detect the bedrock limit. Another disadvantage of this array is linked to its depth of investigation that is moderate compared to the two others arrays (Wenner Schlumberger and dipole-dipole).

The dipole-dipole array is generally used when a good lateral resolution is needed to image vertical or nearly vertical structures such as sharp fractured zones. Unlike the Wenner Alpha array, it has generally a lower signal-to-noise ratio. This means that great cautions are needed before and during the data acquisition procedure to maintain the noise at the lowest level as possible. Its depth of investigation is better than the Wenner Alpha array.

The Wenner Schlumberger array has characteristics in between the Wenner Alpha and the dipole-dipole array. This electrode configuration is generally used when prior information about the electrical structures is scarce or missing.

The signal-to-noise ratio may be related to the value of the geometrical factor K that multiplies the electrical resistance to obtain an apparent resistivity value. The latter is the resistivity that gives the same electrical resistance with the same electrode configuration under the assumption of a homogeneous electrical resistivity distribution. Electrical resistances are often converted into apparent resistivities in inversion softwares such as Res2Dinv (Loke and Barker, 1996). Therefore, even a small error in the electrical resistance can give a large error in the apparent resistivity if K is large.

The geometrical factors for the Wenner Alpha, the Wenner Schlumberger and the dipole-dipole arrays are respectively given by

$$\mathrm{K} = 2\pi\mathrm{a} \tag{2.1}$$

$$\mathrm{K} = \pi\mathrm{n}(\mathrm{n}+1)\mathrm{a} \tag{2.2}$$

$$\mathrm{K} = \pi\mathrm{n}(\mathrm{n}+1)(\mathrm{n}+2)\mathrm{a} \tag{2.3}$$

where a is the dipole length and n the spacing factor that multiplies a (Figure 2.1). From these equations, we can see that the dipole-dipole array has a larger K than the Wenner Schlumberger array and the Wenner Alpha array. Since K is proportional to n^3 for the dipole-dipole array and n^2 for the Wenner Schlumberger array, we strictly limited the spacing factor to 6 when we designed the measurement sequences in order to find a compromise between a good sensitivity and noisy data.

2.3. Data acquisition and associated issues

Data quality is of critical importance in data inversion. Therefore, great care must be taken to set up ERT profiles and to acquire the data in order to maximize the signal-to-noise ratio. This can be achieved by reducing the noise level and by increasing the signal.

Reducing the noise level is not an easy task since it is generally site dependent. However, this can be achieved by combining several recommendations. Since ERT is a method that requires injecting electrical current and measuring electrical potential, it is crucial to improve the electrical contact between the soil and the electrodes (i.e., the contact resistance). Hammering the stainless steel electrodes at a depth of about 40 cm already allows a good improvement of the contact resistance (Figure 2.2). Further watering the electrodes with salty water can also help improving the contact resistance, especially in dry areas. Doing so, we almost always obtained contact resistances in the range of some hundred Ω. However, when field conditions are not ideal (e.g., a dry soil with a lot of small stones), the contact resistance can reach a few thousands Ω and measurements could be noisy.

Another way to reduce the noise level is to integrate the signal over a larger time window by selecting a higher electrical current injection time window. This is particularly useful when high frequency noise is present.

Improving the signal-to-noise ratio can be done by increasing the signal by repeating the measurement several times (i.e., by stacking several signals) until the repetition error reaches the desired level. The number of stacks is site dependent but we generally used 3 to 6 stacks with a quality factor of 1%. This quality factor also known as the repetition error corresponds to the standard deviation value of the measurement. A low quality factor means a highly reproducible data.

Increasing the signal could also be achieved by injecting a higher current intensity into the soil. This can be done by two different ways depending on the acquisition device that is used. First, a higher known intensity can be selected by imposing a higher voltage between the current electrodes but this has some drawbacks such as the saturation of the measurement range. Second, a chosen potential can be acquired between the potential electrodes while the input current is modulated to achieve the desired potential. The latter has some advantages since it is possible to constrain the readings to a certain value and as a consequence, avoid small potential values (e.g., < 1 mV).

Another precaution we took concerns the design of the measurement sequences. We generally tried to avoid making a potential measurement with an electrode that was previously used to inject current into the soil as it is recommended by Dahlin (2000), for example. This is particularly useful with the dipole-dipole array.

All these recommendations may sound obvious and certainly cost time during the data acquisition but data quality should always be preferred when it is possible otherwise inversion results could be difficult to interpret (see section 2.4.2).

Since the inverse electrical problem is ill-posed (LaBrecque et al., 1996), a good estimate of the true data error is crucial to prevent the misinterpretation of the inverted model. In fact, incorrect noise estimates could lead to a gross smoothing of the model when the standard deviation is overestimated. Inversely, noise underestimation tends to create artifacts in the resulting image. Furthermore, the increase in the error level limits the resolution of the electrical structures. Such noise can arise from a lot of different factors such as experimental or numerical problems (e.g., Slater et al., 2000; Zhou and Dahlin, 2003).

Repeatability tests or reciprocal measurements (swapping current and potential electrodes) are two ways to measure data errors. However, repetition errors (commonly used as a data quality indicator) are generally measures of precision and not accuracy. The reciprocal error is defined as:

$$e_{N/R} = R_N - R_R \tag{2.4}$$

where R_N is the normal resistance measurement and R_R is the reciprocal one. As interchanging the electrode locations should not affect the measured resistances (Parasnis, 1988), $e_{N/R}$ is an estimate of data noise and is being used by many authors (e.g., Slater et al., 2000; Slater et al., 2002; Koestel et al., 2008) to estimate the true data error.

Slater et al. (2000) assumed that the true error can be approximated by the line which encompass all errors in the ($|R|$, $|e_{N/R}|$) plane. This line has for equation:

$$|e| = a + bR \tag{2.5}$$

where a is the absolute resistance error component (Ω), b the relative resistance error component (dimensionless) and R the mean transfer resistance (Ω). Koestel et al. (2008) used an extension of this methodology which consists of subdividing the range of mean transfer resistances into logarithmically equally sized bins. For each bin, the standard deviation (s_{bin}) of the reciprocal error $e_{N/R}$ in that bin is calculated. The error model parameters a and b are then determined by fitting the right-hand side of Eq. (2.2) to s_{bin} and define the standard deviation value of the reciprocal error.

We compared both approaches and we obtained similar but not identical error model parameters (Robert et al., 2011). Generally, the Slater et al. (2000) approach gives slightly higher parameters than the Koestel et al. (2008) approach. The latter is also less subjective since the line which encompass all errors in the ($|R|$, $|e_{N/R}|$) plane generally depends on the practitioner that positions it. In this work, whenever we collected the full reciprocal data set, we used the reciprocal errors directly as individual errors. Otherwise, we estimated the error model parameters with one of the two previous approaches.

2.4. Inversion

Assume a data vector $\mathbf{d} = (d_1, d_2, \ldots, d_N)^T$ containing N data and a model vector $\mathbf{m} = (m_1, m_2, \ldots, m_M)^T$ containing M model parameters. Assume that a given forward problem can be written in the form

$$\mathbf{d} = f(\mathbf{m}) \tag{2.6}$$

where f is the forward operator of the problem. This forward operator can be in some cases an ordinary differential equation or partial differential equation and, in other cases, a linear or nonlinear system of algebraic equations (Aster et al., 2005).

The forward problem consists in calculating some observations ($\mathbf{d}$) or data knowing the model parameters ($\mathbf{m}$). The inverse problem consists in retrieving the model parameters ($\mathbf{m}$) that explain some measured observations ($\mathbf{d}$). In electrical resistivity tomography, the model is the electrical resistivity distribution of the subsurface whereas the data set is composed of a series of measured electrical resistances that are each associated with a specific quadripole of electrodes. In ERT, log transformed data and parameters are generally taken in order to take into account the wide range of electrical resistivity that occurs in the subsurface and to ensure positivity. As an example, a compact limestone presents resistivity value of several thousands Ω.m whereas a water-bearing fractured limestone can present resistivity value in the range of some Ω.m. Therefore, data and model in ERT are

$$d_i = \ln R_i \tag{2.7}$$

$$m_j = \ln \sigma_j \tag{2.8}$$

where i = 1, 2, …, N and j = 1, 2, …, M and where R_i is the electrical resistance measured with a quadripole i and σ_j the electrical conductivity assigned to the cell j.

In practice, solving inverse problems requires the knowledge of how much noise affects the data. Assume a vector $\mathbf{e} = (e_1, e_2, \ldots, e_N)^T$ containing the N associated errors that affect $\mathbf{d}$, then the problem can be rewritten as

$$\mathbf{d} = f(\mathbf{m}) + \mathbf{e} \tag{2.9}$$

The inverse problem is generally solved by minimizing an objective function that is dependent of the data discrepancy vector $\mathbf{r}$ that is the difference between the data vector and the model response (the simulated data vector):

$$\mathbf{r} = \mathbf{d} - f(\mathbf{m}) \tag{2.10}$$

Therefore, noise estimation is crucial to prevent the algorithm inverting noise and as a consequence, bringing so-called artifacts in the inverted model.

The DC electrical forward model is solved using a finite-element method to predict the resistance given the position and intensity of known current sources. Specific details on its implementation can be found in Kemna (2000). ERT inversion is a non-linear discrete problem where the model is composed of M model parameters, corresponding to the electrical resistivity values of the different finite elements. The inversion is solved using an iterative optimization algorithm where the best model is searched given some constraints and within an acceptable data residual limit. This limit is generally deduced from data errors characterization.

Ill-posed problems including ERT inversion are inherently difficult. In geological media, they are even more difficult. If we defined the best solution of an inverse problem as the model that fits to the data given a defined error criterion, it may not exist geologically or physically. This can occur if the mathematical model is approximate, for example with a too restrictive assumption in the governing equation (e.g., Nguyen et al., 2007). It can also occur if the resulting image models noise if the error criterion is only poorly estimating its true value.

If the best solution does exist, it may also not be unique. This means that an infinite number of solutions can fit to the data equally. A well-known example of this is the equivalence and suppression principles in vertical electrical sounding (VES). In addition to the mathematical non-uniqueness, there is an intrinsic non-uniqueness in terms of interpretation since resistivity values often overlap between rock and sediments types as a function of porosity, water content, salinity and the presence of clayey minerals.

ERT inversion is an ill-conditioned inverse problem that leads to instability of the solution. An ill-conditioned problem is characterized by the fact that a small change in the data (e.g., a small increase of noise) can lead to strong changes in the resulting model. To stabilize the inversion process, regularization is generally used (Tikhonov and Arsenin, 1977). Regularization consists in adding some constraints that bias the solution. This also means that, given some a priori information, we can choose a regularization technique that biases the solution in a way that it satisfies this a priori information too (see section 2.4.3).

In the following sections, we present the objective function that is minimized in electrical resistivity tomography. For clarity, we will separate the discussion related to the data misfit and the model constraint in two different sections.

2.4.1. Objective function

The objective function that we want to minimize can be written as (Kemna, 2000)

$$\Psi(\mathbf{m}) = \Psi_d(\mathbf{m}) + \lambda\Psi_m(\mathbf{m}) \tag{2.11}$$

where $\Psi_d(\mathbf{m})$ is the chi-squared measure of the data misfit, $\Psi_m(\mathbf{m})$ is a model objective function containing the desired model characteristics or the desired model constraint, λ is a real, positive number called regularization parameter and $\mathbf{m}$ is the vector $(m_1, m_2, \ldots, m_M)^T$ containing the M model parameters.

2.4.2. Data misfit

If we assume a set of N measured data written in a vector $\mathbf{d} = (d_1, d_2, \ldots, d_N)^T$ and N associated errors $\mathbf{e} = (e_1, e_2, \ldots, e_N)^T$ then the chi-squared measure of the data misfit is defined as

$$\Psi_d(\mathbf{m}) = \sum_{i=1}^{N} \frac{|d_i - f_i(\mathbf{m})|^2}{|\varepsilon_i|^2} \tag{2.12}$$

where f_i is the finite element forward operator. It is assumed that each data is contaminated by uncorrelated Gaussian noise with zero mean and individual standard deviation ε_i. This standard deviation value can be estimated from the individual reciprocal errors or from the error characterization since

$$\varepsilon_i = \Delta \ln R_i \sim \frac{\Delta R_i}{R_i} = \frac{e_i}{R_i} \tag{2.13}$$

The root mean squared or RMS error can be written as

$$\varepsilon^{RMS}(\mathbf{m}) = \sqrt{\frac{\Psi_d(\mathbf{m})}{N}} \tag{2.14}$$

A stopping criterion is usually taken on the RMS error. In this work, we stopped the inversion process once the RMS error converges toward the standard deviation value of the reciprocal errors distribution. The expected value of the chi-square variable is N.

Another way to calculate the data misfit is to use a robust or L_1 norm instead of the L_2 norm. The function related to the data misfit becomes

$$\Psi_d(\mathbf{m}) = \sum_{i=1}^{N} \frac{|d_i - f_i(\mathbf{m})|}{|\varepsilon_i|} \tag{2.15}$$

The L_1 norm solution is a solution that is less affected by data outliers (discordant observations) than the L_2 norm solution, because each term of the data misfit function are not squared, as it is in the chi-squared measure of the data misfit (L_2 norm). However, it requires a supplementary computational effort since the L_1 norm is non-differentiable. In this case, an iterative reweighted least-squares (IRLS) algorithm is used (e.g., Aster et al., 2005). Moreover, both strategies lead to similar results when outliers are not present. However, if one suspects some outliers in the data set, this strategy will be more effective. We always used a robust data constraint in this Ph.D. thesis.

2.4.3. Model constraint

Different types of model constraints exist and should be used given some prior knowledge about the electrical structures distribution. Among the most used ones, we can cite the smoothness constraint (deGroot-Hedlin and Constable, 1990; Constable et al., 1987), the blocky inversion (Farquharson and Oldenburg, 1998; Loke et al., 2003), and the minimum gradient support approach (Blaschek et al., 2008; Portniaguine and Zhdanov, 1999). Blaschek et al. (2008) compared these three different approaches that are summarized below.

The widely used smoothness constraint can be written as

$$\Psi_{\mathrm{m}}(\mathbf{m}) = \iint ||\boldsymbol{\nabla}\mathbf{m}||^2 \mathrm{dxdz} \tag{2.16}$$

where $\boldsymbol{\nabla}$ is the 2D gradient operator.

An inversion with this conventional smoothness constraint is also known as Occam's inversion. Here, $\Psi_{\mathrm{m}}(\mathbf{m})$ is the integral over the L_2 norm of the model gradient (deGroot-Hedlin and Constable, 1990). As a result, the inverted electrical structures vary in a smooth manner and it is impossible to produce images with sharp gradients.

An alternative consists in the blocky inversion (e.g., Farquharson and Oldenburg, 1998; Loke et al., 2003) where $\Psi_{\mathrm{m}}(\mathbf{m})$ is the integral over the L_1 norm of the model gradient

$$\Psi_{\mathrm{m}}(\mathbf{m}) = \iint ||\boldsymbol{\nabla}\mathbf{m}|| \mathrm{dxdz} \tag{2.17}$$

Since the L_1 norm only increases linearly with the model gradient, an inversion performed with this model constraint also known as a robust model constraint or blocky inversion, produces sharper structures than the conventional smoothness constraint inversion. Indeed, the penalty for larger gradient is smaller in the blocky inversion than in the Occam's inversion.

A third approach that is also investigated in this thesis is known as the minimum gradient support (MGS) approach which seeks to limit the number of parameters contrasts (in our case, it limits the occurrence of electrical resistivity contrasts), independently of their magnitude (Portniaguine and Zhdanov, 1999). The function can be written as

$$\Psi_{\mathrm{m}}(\mathbf{m}) = \iint \frac{\boldsymbol{\nabla}\mathbf{m}\cdot\boldsymbol{\nabla}\mathbf{m}}{\boldsymbol{\nabla}\mathbf{m}\cdot\boldsymbol{\nabla}\mathbf{m} + \beta^2} \mathrm{dxdz} \tag{2.18}$$

where β is a small, real, positive number according to Portniaguine and Zhdanov (1999).

Using a small β leads to very blocky electrical images where zones where no parameter variation occurs are separated with sharp contrasts. Indeed, under this condition, the functional acts like a step function (Blaschek et al., 2008) as it can be seen from

$$\lim_{\beta\to 0} \frac{\nabla\mathbf{m}\cdot\nabla\mathbf{m}}{\nabla\mathbf{m}\cdot\nabla\mathbf{m}+\beta^2} = \begin{cases} 0 \text{ for } \nabla\mathbf{m} = 0 \\ 1 \text{ for } \nabla\mathbf{m} \neq 0 \end{cases} \tag{2.19}$$

Indeed, very small variations are penalized in the same way as very large ones. In contrary, using large β leads to smooth images analog to the resulting images obtained with the conventional smoothness-constraint. Indeed, under this condition, the functional is proportional to the L_2 norm as it can be seen from

$$\lim_{\beta\gg} \frac{\nabla\mathbf{m}\cdot\nabla\mathbf{m}}{\nabla\mathbf{m}\cdot\nabla\mathbf{m}+\beta^2} \approx \frac{\nabla\mathbf{m}\cdot\nabla\mathbf{m}}{\beta^2} \infty \nabla\mathbf{m}\cdot\nabla\mathbf{m} \tag{2.20}$$

Blaschek et al. (2008) explored different ranges of β and they found that using a moderate β allows obtaining electrical images with sharp contrasts but also that this allows for the electrical resistivity to vary in a smooth manner within the different zones.

According to Blaschek et al. (2008), "*parameter gradients with a steep slope tend to be unstable, because a small decrease in the parameter gradient (with little effect on the data misfit) leads to a large decrease in the contribution to the regularization term where the slope is steeper*". The main difference between the L_1 and L_2 norm inversion is their behavior for different parameter gradient values. Basically, higher gradients are more stable with the L_1 norm whereas smaller gradient are more stable with the L_2 norm (Blaschek et al., 2008). In the MGS function, the parameter gradients stability depends on β. As a consequence, by varying β, the ranges of the different regions of stability can be changed and this is the main advantage of the MGS inversion compared to the L_1 and L_2 norm inversions.

In this section, we presented isotropic inversion. In some cases, it can be helpful to bias the inverted model with anisotropy. For example, a homogeneous tabular aquifer will present horizontal layers of different electrical resistivity whereas a fault zone or a fractured area could present more vertical limits with host rocks.

To impose anisotropy to the inverted model, we can rewrite Eq. (2.16) as

$$\Psi_m(\mathbf{m}) = \alpha_x \iint ||\nabla_x\mathbf{m}||^2 dxdz + \alpha_z \iint ||\nabla_z\mathbf{m}||^2 dxdz \tag{2.21}$$

where $\nabla_{x} = \frac{\delta}{\delta x}$ and $\nabla_{z} = \frac{\delta}{\delta z}$ are the gradient operators in the x and z direction, and α_x and α_z are two real numbers. The case where both α_x and α_z are equal corresponds to an isotropic inversion. To accentuate horizontal or vertical structures in the inverted model, we must respectively increase or decrease the ratio α_x/α_z.

2.4.4. Image appraisal

When interpreting a geophysical image that results from data inversion, Oldenburg and Li (1999) listed a few questions to check for image appraisal: "*(1) Which features in the recovered model emulate those in the true earth? (2) What confidence do we have in the existence of the features? (3) What is the level of detail that can be responsibly inferred? (4) Are there artifacts at depth, which if interpreted, would lead to misleading interpretations?*".

Answering these questions is not an easy task since there are all interrelated. However, several quantities such as the resolution, the sensitivity or the depth of investigation of ERT can be investigated in order to appraise electrical images.

The model resolution matrix can be defined as "*the lens or filter through which the inversion sees the study region*" (Day-Lewis et al., 2005) and some authors (Alumbaugh and Newman, 2000 ; Friedel, 2003 ; Oldenborger and Routh, 2009; Ramirez, 1995) used this matrix as an image appraisal tool. However, the computation time of the model resolution matrix is quite high (Kemna, 2000) and the cumulative sensitivity matrix ($\mathbf{S}$) is therefore often preferred. This matrix can be written as

$$\mathbf{S} = \sum_{i=1}^{n} \left[\frac{(J)_{ij}}{\varepsilon_i}\right]^2 = \mathrm{diag}(\mathbf{J}^T \mathbf{W}_\mathbf{d}^T \mathbf{W}_\mathbf{d} \mathbf{J}) \qquad (2.22)$$

where $\mathbf{J}$ is the Jacobian matrix and $\mathbf{W_d}$ the data weighting matrix (containing the data errors). The cumulative sensitivity matrix gives directly an idea about the sensitivity of measurements subject to changes in the electrical structures. Areas with poor sensitivity are generally considered as less reliable. Indeed, if a change occurs in these areas, this will barely modify the surface data. This matrix was successfully used as an image appraisal tool in Nguyen et al. (2009) and Robert et al. (2011; 2012).

Different approaches to quantify depth of investigation have been introduced so far and a concise summary of these methods can be found in Barker (1989). Some concepts were associated with a depth to which the data are particularly sensitive (e.g., Edwards, 1977; Evjen, 1938; Roy, 1972; Roy and Apparao, 1971) whereas other authors (e.g., Apparao et al., 1992; Van Nostrand, 1953) used a series of forward modeling to see if sufficient changes in the predicted data were retrieved by adding or not a specific feature at depth. Such methodologies have some advantages regarding survey design but they cannot easily quantify the depth of investigation of an electrical image resulting from field data inversion (Oldenburg and Li, 1999).

Oldenburg and Li (1999) introduced a new definition of the depth of investigation that is "*the depth below which the data are no longer sensitive to the physical property*" (here, the electrical resistivity). Their approach was to alter the model objective function $\Psi_{\mathrm{m}}(\mathbf{m})$ and observe the differences between several resulting images. Then, areas that are no longer constrained by field data are deduced from the locations where large differences occur between the different inverted models. To do this, they chose to alter the reference model $\mathbf{m_0}$.

In order to use the methodology of Oldenburg and Li (1999), an additional term must be introduced in the model objective function $\Psi_{\mathrm{m}}(\mathbf{m})$:

$$\Psi_{\mathrm{m}} = \alpha \iint (\mathbf{m} - \mathbf{m_0})^2 \,\mathrm{dxdz} + \iint ||\boldsymbol{\nabla}\mathbf{m}||^2 \mathrm{dxdz} \tag{2.23}$$

where α is a real, positive number. The second term in Eq. (2.23) is the conventional smoothness constraint.

Assume that the background reference model $\mathbf{m_0}$ is a homogeneous half-space with a value corresponding to the mean apparent resistivity (the mean value of the field data) and that α is large enough to consider the first term of the previous equation as sufficiently important in the minimization. Consider also two different constant reference models $\mathbf{m_{1r}}$ and $\mathbf{m_{2r}}$ and the associated inverted models $\mathbf{m_1}$ and $\mathbf{m_2}$. Then, a depth of investigation (DOI) index can be defined as

$$\mathbf{R}(\mathrm{x,z}) = \frac{\mathbf{m_1}(\mathrm{x,z}) - \mathbf{m_2}(\mathrm{x,z})}{\mathrm{m_{1r}} - \mathrm{m_{2r}}} \tag{2.24}$$

At locations where the two different inversions produce the same model parameters independently from the value used for the reference model, the DOI index $\mathbf{R}$ will approach zero. These parts of the inverted model can be assigned with a high credibility since there are constrained by field data rather than the choice of the reference model. On the contrary, at locations where the two different inversions result in large differences, $\mathbf{R}$ will approach unity. These areas must be assigned with a low credibility since the inverted model reproduces the reference model and is no longer constrained by field data.

An alternative scaled index was also defined by Oldenburg and Li (1999) in order to reduce the effect of the choice of reference models or the choice of α (see also Marescot et al., 2003). It is defined as

$$\mathbf{R}_{\mathbf{scaled}}(x, z) = \frac{\mathbf{R}(x,z)}{R_{max}} \tag{2.25}$$

where R_{max} is the maximum value of the DOI index. Marescot et al. (2003) also showed that the DOI index methodology presents better results using a conventional smoothness constraint inversion. Generally, the highest differences in the model parameters linked to the choice of the reference model value occur at depth. However, using a blocky inversion, these strong differences can occur close to the surface and the DOI index map becomes difficult to interpret. We also saw similar results in Robert et al. (2011). In the case of a blocky inversion (or any other focused inversion scheme), it might be preferable using the resolution or cumulative sensitivity matrix to estimate the depth of investigation even if the choice of the cutoff value is more difficult within these approaches.

According to Oldenburg and Li (1999), the choice of a cutoff value of the DOI index is not crucial since “*once the DOI index begins its increase, it does so rather quickly*”. The use of a specified cut-off value (0.1 or 0.2 as recommended by the authors) to filter the electrical image is quite “*extreme and not physical since our ability to see into the earth diminishes gradually with depth*”. An efficient way to use this index is to compare the inverted model with the corresponding DOI index image in order to see which parts of the electrical features are really linked with field data.

This methodology is quite simple to use since it only requires running two different inversions that only differ by the reference model value. In this thesis, we generally expected strong electrical resistivity contrasts. Therefore, we used the two-sided approach which consists in taking as reference model values a tenth or ten times the value of $\mathbf{m_0}$ (corresponding to the mean value of the apparent resistivity distribution).

Several authors used successfully this index to estimate the depth of investigation of their electrical images, especially in studies where strong electrical contrasts where expected such as permafrost studies (e.g., Hilbich et al., 2009; Marescot et al., 2003) or fractured zones delineation (Robert et al., 2011). Oldenborger et al. (2007) also extended the DOI index in the third dimension by defining the volume of investigation (VOI) index.

2.4.5. Time-lapse inversion

Time-lapse measurements can be used to obtain information about dynamic changes of subsurface properties in comparison of static geophysical surveys. Changes in a subsurface property such as the electrical resistivity can then be used to infer information about subsurface processes. In hydrogeophysics, this concerns domains such as groundwater flow, solute transport, variation in the moisture content, water or pollutant infiltration, and sea water intrusion among many others. Time-lapse ERT has been increasingly used to monitor these processes (e.g., Binley et al., 2002; Hermans et al., 2012; Kemna et al., 2002, Miller et al., 2008; Nguyen et al., 2009; Robert et al., 2012).

Acquiring time-lapse ERT data sets consists in collecting the same ERT sequence many times. Advances in the ERT instrumentation including multi-channel acquisition have made it possible to obtain large data sets in a smaller amount of time and therefore increasing the temporal resolution of ERT monitoring. As an example, the acquisition of 1000 dipole-dipole data points with an ABEM SAS1000 Lund Imaging system (1 recording channel) took approximately 3 h whereas it only takes ½ h with the ABEM LS Terrameter (12 recording channels), all parameters being the same. These new equipments also allow better signal-to-noise ratio because the repeatability of measurements has improved.

Once the different measurements composing the time-lapse data sets are collected, the changes in the electrical resistivity distribution are calculated by inverting the data using several time-lapse strategies that are described below.

Rewriting Eq. (2.11) with a matrix formulation of Eq. (2.12) – data misfit – and Eq. (2.16) – model constraint – gives

$$\Psi(\mathbf{m}) = ||\mathbf{W_d}(\mathbf{d} - \mathrm{f}(\mathbf{m}))||^2 + \lambda||\mathbf{Rm}||^2 \tag{2.26}$$

where $\mathbf{R}$ is a matrix evaluating the (first-order) roughness of $\mathbf{m}$. Adding a reference model in the inversion – see Eq. (2.23) – can be written, still with a matrix formulation, as

$$\Psi(\mathbf{m}) = ||\mathbf{W_d}(\mathbf{d} - \mathrm{f}(\mathbf{m}))||^2 + \lambda(||\mathbf{Rm}||^2 + \alpha||(\mathbf{m} - \mathbf{m}_0)||^2) \tag{2.27}$$

where $\mathbf{m_0}$ can be any reference model.

Note that we can also use

$$\Psi(\mathbf{m}) = ||\mathbf{W_d}(\mathbf{d} - \mathrm{f}(\mathbf{m}))||^2 + \lambda(||\mathbf{R}(\mathbf{m} - \mathbf{m_0})||^2 + \alpha||(\mathbf{m} - \mathbf{m}_0)||^2) \tag{2.28}$$

if we want to simultaneously smooth the model changes and keep the changes tied to $\mathbf{m_0}$.

The first time-lapse strategy consists in performing independent inversions using Eq. (2.26) and then subtracting resulting models to obtain an image highlighting the changes in the electrical resistivity distribution between different time periods. One advantage with this method is that it is not necessary to possess the same data set (i.e., data may be missing) even if it is not recommended. Indeed, if two surveys have different resolutions or if the parameterization of the data is not identical, artifacts may appear with model subtraction. As pointed out by Miller et al. (2008), "*as long as the noise assumptions are chosen appropriately for the respective data sets, model differencing should provide stable results*". Concerning the parameterization, the use of the same mesh between the background model and later models should also improve the stability of the solution in terms of artifacts.

The second time-lapse strategy still consists in independent inversions but this time, adding as a reference model the background inverted model, by using Eq. (2.27). The background resistivity model (t = 0) is obtained by a standard inversion and is then used as a reference model for the inversion of later time (t > 0) data sets. Miller et al. (2008) refer to this method as a cascaded time-lapse inversion approach. According to them, "*this should effectively localize the model differences within the region that is supported by the data because all others regions will revert to the base (background) model*". This methodology is more practical than the model subtraction approach. Indeed, the convergence of the inversion algorithm is faster since the prior and reference models are already closer to the final solution than a simple homogeneous half-space.

Daily et al. (2002) and then LaBrecque and Yang (2000) proposed a third strategy by inverting directly the differences in the data or data residues ($\mathbf{d} - \mathbf{d_0}$) to find the model perturbations ($\mathbf{m} - \mathbf{m_0}$). This approach also used by Kemna et al. (2002) and Miller et al. (2008), for example, can be written in a matrix formulation as

$$\Psi_{\mathrm{diff}}(\mathbf{m}) = ||\mathbf{W_d}[(\mathbf{d} - \mathbf{d_0}) - (\mathrm{f}(\mathbf{m}) - \mathrm{f}(\mathbf{m_0}))]||^2 + \lambda||\mathbf{R}(\mathbf{m} - \mathbf{m_0})||^2 \qquad (2.29)$$

where $\mathbf{d_0}$ and $\mathbf{d}$ denote data sets collected at times t = 0 and t > 0, respectively, and where $\mathbf{m_0}$ and $\mathbf{m}$ corresponds to the inverted models at times t = 0 and t > 0, respectively.

Eq. (2.29) is exactly the same as Eq. (2.26) excepting that we invert the data residues ($\mathbf{d} - \mathbf{d_0}$), instead of a data set $\mathbf{d}$, to obtain the model perturbations ($\mathbf{m} - \mathbf{m_0}$), instead of the resistivity model $\mathbf{m}$. With this approach, it is crucial to estimate the appropriate noise level of every time-lapse data set. Otherwise, data differencing could accentuate the noise in the data difference. As a consequence, this methodology could be very effective in the case of data sets with constant noise levels over time.

Hereafter, we will refer to these approaches by using the terms "*independent inversion*", "*cascaded inversion*", and "*data difference inversion*", respectively. We will see in section 6.4 that the noise characterization is the most crucial point in time-lapse inversion as it was already pointed out by Miller et al. (2008). Results from LaBrecque et al. (1996) concerning the under or overestimation of the noise levels are still valid for time-lapse inversion (see section 2.1.3).

The choice of the regularization approach (L_2 norm, L_1 norm, MGS, anisotropy) will also have an effect on the resulting time-lapse image. Every model constraint presented above in section 2.4.3 can be applied on the model perturbations ($\mathbf{m} - \mathbf{m_0}$) instead of the resistivity model $\mathbf{m}$. As an example, the MGS approach (with a small β) will limit the occurrences of changes in electrical resistivity but will also restrict the variations of these changes inside the different zones. The choice of a model constraint is therefore still related with the knowledge of a priori information as it was the case for static inversion.

Previous regularization approaches (L_2 norm, L_1 norm, MGS, anisotropy) are applied on the spatial dimension. In some cases, it might be useful to apply a regularization in the time domain too, for example when prior information is known about the rate at which the processes we monitor occur. In order to take such information into account, we can add a second model-constraint term in the general objective function which is given by Eq. (2.11) and this will give

$$\Psi(\mathbf{m}) = \Psi_{\mathrm{d}}(\mathbf{m}) + \lambda\Psi_{\mathrm{m},\,\mathrm{R}^3}(\mathbf{m}) + \mu\Psi_{\mathrm{m},\,\mathrm{Time}}(\mathbf{m}) \qquad (2.30)$$

where the first and second terms still relate to the data misfit and the model constraint (in the spatial dimension), respectively but where the third term is a model constraint in the time domain (μ being the corresponding regularization parameter). As an example, the total model constraint can be in the form of

$$\Psi_{\mathrm{m}}(\mathbf{m}) = ||\mathbf{W}_{\mathbf{m}}(\mathbf{m} - \mathbf{m}_{\mathbf{0}}) + \frac{1}{\mathrm{v}}(\mathbf{m} - \mathbf{m}_{\mathbf{0}})||^2 \qquad (2.31)$$

where the first term corresponds to the smoothing of spatial changes and the second term to a regularization using prior information about the rate of the process since the parameter v can be seen as a velocity. Therefore, if we want to monitor a salt tracer test in an aquifer where diffusion is the main transport mechanism, then we can use a low velocity assumption, e.g., v=0.1. In contrary, in a fractured aquifer where strong hydraulic gradients are present, the main mechanism of solute transport might be advection and the assumption of a high velocity, e.g., v=0.5, might be more adequate.

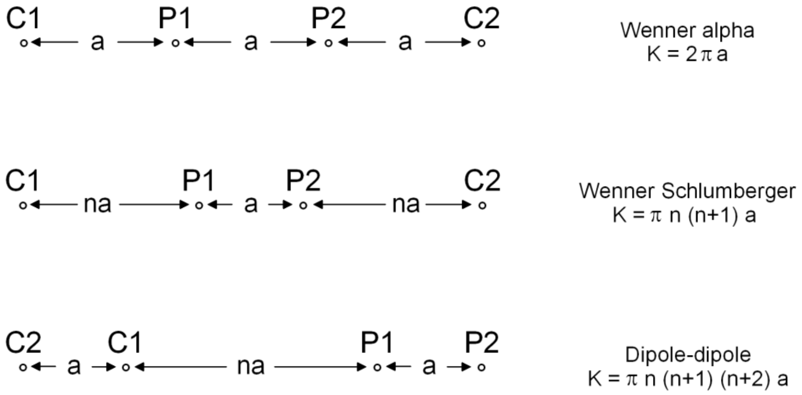

Figure 2.1: The geometrical factor (K) multiplies the electrical resistance to obtain an apparent electrical resistivity. This apparent resistivity is the resistivity that gives the same electrical resistance with the same electrode configuration under the assumption of a homogeneous electrical resistivity distribution. Electrical resistances are generally converted into apparent resistivities in inversion softwares such as Res2Dinv (Loke and Barker, 1996). Therefore, even a small error in the resistance can give a large error in the apparent resistivity if the geometrical factor is large. Note that C1 and C2 are the current electrodes whereas P1 and P2 are the potential electrodes.

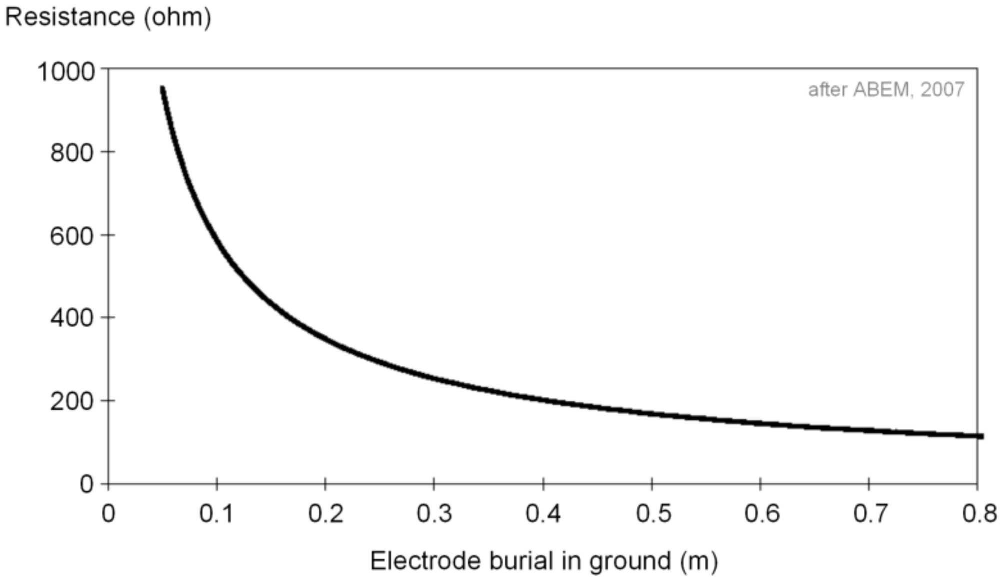

Figure 2.2: Generally a depth of 40 cm is enough to bury the electrode in the soil since the theoretical relation between electrode burial and the contact resistance (ABEM, 2007) reaches an asymptote near 40 cm.

References

ABEM, 2007, *Instruction manual, Terrameter SAS 1000 / 4000*, 147 pp, ABEM Instrument AB, Sweden.

Alumbaugh, D. L., and G. A. Newman, 2000, *Image appraisal for 2-D and 3-D electromagnetic inversion*, Geophysics, 65 (5), 1455-1467.

Apparao, A., Rao, T. G., Sastry, R. S., and Sarma, V. S., 1992, *Depth of detection of buried conductive targets with different electrode arrays in resistivity prospecting*, Geophysical Prospecting, 40, 749–760.

Aster, R. C., B. Borchers, and C. H. Thurber, 2005, *Parameter Estimation and Inverse Problems*, In International Geophysics Series, volume 90, Elsevier Academic Press, Amsterdam, 301 pp.

Athanasiou, E. N., P. I. Tsourlos, C. B. Papazachos, and G. N. Tsokas, 2007, *Combined weighted inversion of electrical resistivity data arising from different array types*, Journal of Applied Geophysics, 62 (2), 124-140.

Barker, R. D., 1989, *Depth of investigation of collinear symmetrical four-electrode arrays*, Geophysics, 54 (8), 1031-1037.

Blaschek, R., A. Hordt, and A. Kemna, 2008, *A new sensitivity-control led focusing regularization scheme for the inversion of induced polarization data based on the minimum gradient support*, Geophysics, 73 (2), F45-F54.

Binley, A., G. Cassiani, R. Middleton, and P. Winship, 2002, *Vadose zone flow model parameterisation using cross-borehole radar and resistivity imaging*, Journal of Hydrology, 267 (3-4), 147-159.

Constable, S. C., R. L. Parker, and C. G. Constable, 1987, *Occam's inversion: A practical algorithm for generating smooth models from electromagnetic sounding data*, Geophysics, 52 (3), 289-300.

Daily, W., A. Ramirez, D. LaBrecque, and J. Nitao, 1992, *Electrical resistivity tomography of vadose water movement*, Water Resources Research, 28 (5), 1429-1442.

Day-Lewis, F. D., K. Singha, and A. M. Binley, 2005, *Applying petrophysical models to radar travel time and electrical resistivity tomograms: Resolution-dependent limitations*, Journal of Geophysical Research, 110, B08206, doi:10.1029/2004JB003569.

Dahlin, T., 2000, *Short note on electrode charge-up effects in DC resistivity data acquisition using multi-electrode arrays*, Geophysical Prospecting, 48 (1), 181-187.

Dahlin, T., and B. Zhou, 2004, *A numerical comparison of 2D resistivity imaging with 10 electrode arrays*, Geophysical Prospecting, 52 (5), 379-398.

deGroot-Hedlin, C., and S. Constable, 1990, *Occam's inversion to generate smooth, two-dimensional models from magnetotelluric data*, Geophysics, 55 (12), 1613-1624.

Edwards, L. S., 1977, *A modified pseudosection for resistivity and induced-polarization*, Geophysics, 42, 1020-1036.

Evjen, H. M., 1938, *Depth factor and resolving power of electrical measurements*, Geophysics, 3, 78-95.

Farquharson, C. G., and D. W. Oldenburg, 1998, *Non-linear inversion using general measures of data misfit and model structure*, Geophysical Journal International, 134 (1), 213-227.

Friedel, S., 2003, *Resolution, stability and efficiency of resistivity tomography estimated from a generalized inverse approach*, Geophysical Journal International, 153 (2), 305-316.

Guéguen, Y., and V. Palciauskas, 1994, *Introduction to the Physics of Rocks*, 294 pp., Princeton University Press, Princeton, New Jersey.

Hermans, T., A. Vandenbohede, L. Lebbe, and F. Nguyen, 2012, *A shallow geothermal experiment in a sandy aquifer monitored using electric resistivity tomography*, Geophysics, 77 (1), B11-B21.

Hilbich, C., L. Marescot, C. Hauck, M. H. Loke, and R. Mäusbacher, 2009, *Applicability of Electrical Resistivity Tomography Monitoring to coarse blocky and ice-rich permafrost landforms*, Permafrost and Periglacial Processes, 20, 269-284.

Kemna, A., 2000, *Tomographic inversion of complex resistivity : theory and application*, PhD Thesis, University of Bochum, 196 pp.

Kemna, A., J. Vanderborght, B. Kulessa, and H. Vereecken, 2002, *Imaging and characterisation of subsurface solute transport using electrical resistivity tomography (ERT) and equivalent transport models*, Journal of Hydrology, 267 (3-4), 125-146.

Koestel, J., A. Kemna, M. Javaux, A. Binley, and H. Vereecken, 2008, *Quantitative imaging of solute transport in an unsaturated and undisturbed soil monolith with 3D ERT and TDR*, Water Resources Research, 44, W12411, doi:10.1029/2007WR006755.

LaBrecque, D. J., M. Miletto, W. Daily, A. Ramirez, and E. Owen, 1996, *The effects of noise on Occam's inversion of resistivity tomography data*, Geophysics, 61 (2), 538-548.

LaBrecque, D. J., and X. Yang, 2000, *Difference inversion of ERT data: a fast inversion method for 3-D in-situ monitoring*, Proc. Symp. Appl. Geophys. Engng Environ. Problems, Environ. Engng Geophys. Soc., 723–732.

Loke, M. H., I. Acworth, and T. Dahlin, 2003, *A comparison of smooth and blocky inversion methods in 2D electrical imaging surveys*, Exploration Geophysics, 34 (3), 182-187.

Loke, M. H., and R. D. Barker, 1996, *Rapid least-squares inversion of apparent resistivity pseudosections by a quasi-Newton method*, Geophysical Prospecting, 44 (1), 131-152.

Marescot, L., M. H. Loke, D. Chapellier, R. Delaloye, C. Lambiel, and E. Reynard, 2003, *Assessing reliability of 2D resistivity imaging in mountain permafrost studies using the Depth Of Investigation index method*, Near Surface Geophysics, 1, 57-67.

Miller, C. R., P. S. Routh, T. R. Brosten, and J. P. McNamara, 2008, *Application of time-lapse ERT imaging to watershed characterization*, Geophysics, 73 (3), G7-G17.

Nguyen, F., S. Garambois, D. Chardon, D. Hermitte, O. Bellier, and D. Jongmans, 2007, *Subsurface electrical imaging of anisotropic formations affected by a slow active reverse fault, Provence, France*, Journal of Applied Geophysics, 62 (4), 338-353.

Nguyen, F., A. Kemna, A. Antonsson, P. Engesgaard, O. Kuras, R. Ogilvy, J. Gisbert, S. Jorreto, and A. Pulido-Bosch, 2009, *Characterization of seawater intrusion using 2D electrical imaging*, Near Surface Geophysics, 7 (5-6), 377-390.

Oldenborger, G. A., P. S. Routh, and M. D. Knoll, 2007, *Model reliability for 3D electrical resistivity tomography: Application of the volume of investigation index to a time-lapse monitoring experiment*, Geophysics, 72 (4), F167-F175.

Oldenborger, G. A., and P. S. Routh, 2009, *The point-spread function measure of resolution for the 3D electrical resistivity experiment*, Geophysical Journal International, 176 (2), 405-414.

Parasnis, D. S., 1988, *Reciprocity theorems in geoelectric and geoelectromagnetic work, Geoexploration*, 25 (3), 177-198.

Portniaguine, O., and M. S. Zhdanov, 1999, *Focusing geophysical inversion images*, Geophysics, 64 (3), 874-887.

Ramirez, A. L., W. D. Daily, and R. L. Newmark, 1995, *Electrical Resistance Tomography for Steam Injection Monitoring and Process Control*, Journal of Environmental and Engineering Geophysics, 1 (A), 39-51.

Robert, T., A. Dassargues, S. Brouyère, O. Kaufmann, V. Hallet, and F. Nguyen, 2011, *Assessing the contribution of electrical resistivity tomography (ERT) and self-potential (SP) methods for a water well drilling program in fractured/karstified limestones*, Journal of Applied Geophysics, 75 (1), 42-53.

Robert, T., D. Caterina, J. Deceuster, O. Kaufmann, and F. Nguyen, 2012, *A salt tracer test monitored with surface ERT to detect preferential flow and transport paths in fractured/karstified limestones*, Geophysics, 77 (2), B55-B67.

Roy, A., and A. Apparao, 1971, *Depth of investigation in direct current methods*, Geophysics, 36 (5), 943-959.

Roy, A., 1972, *Depth of investigation in Wenner, three-electrode and dipole-dipole DC resistivity methods*, Geophysical Prospecting, 20, 329-340.

Schön, J. H., 2004, *Physical Properties of Rocks, Fundamentals and Principles of Petrophysics*, In Handbook of geophysical exploration, Seismic exploration, volume 18, edited by Helbig, K., and S. Treitel, 600 pp., Elsevier, Amsterdam.

Slater, L., A. M. Binley, W. Daily, and R. Johnson, 2000, *Cross-hole electrical imaging of a controlled saline tracer injection*, Journal of Applied Geophysics, 44 (2-3), 85-102.

Slater, L., A. Binley, R. Versteeg, G. Cassiani, R. Birken, and S. Sandberg, 2002, *A 3D ERT study of solute transport in a large experimental tank*, Journal of Applied Geophysics, 49 (4), 211-229.

Stummer, P., H. Maurer, and A. G. Green, 2004, *Experimental design: Electrical resistivity data sets that provide optimum subsurface information*, Geophysics, 69 (1), 120-139.

Telford, W. M., L. P. Geldart and R. E. Sheriff, 1990, *Applied Geophysics (Second Edition)*,Cambridge University Press, Cambridge, 770pp.

Tikhonov, A. N., and V. A. Arsenin, 1977, *Solution of ill-posed problems*, Winston & Sons, Washington.

Ward, S. H., 1990, *Resistivity and Induced Polarization Methods*, In Geotechnical and environmental geophysics - Investigations in Geophysics No. 5, edited by Ward, S. H., pp. 169-189, SEG.

Van Nostrand, R. G., 1953, *Limitations on resistivity methods as inferred from the buried sphere problem*, Geophysics, 18, 423–433.

Zhou, B., and T. Dahlin, 2003, *Properties and effects of measurement errors on 2D resistivity imaging surveying*, Near Surface Geophysics, 1 (3), 105-117.

3. Self-potential

3.1. Theory and principles

Self-potential (SP) is a geophysical method but the term also relates to the results of physical mechanisms that occur in the earth. This electrical method is passive because it does not require the injection of an electrical current in the ground as the electrical resistivity method. SP consists in passive measurements of the (self) electrical potential at, or slightly below, the ground surface or in boreholes.

Self-potentials are associated with different forcing mechanisms whose causes can be external (e.g., electromagnetic induction or human activities) or internal (e.g., chemical, thermal, or hydraulic gradients). Since human activities could add a high amount of noise in SP signal, highly anthropized areas do not constitute favorable playing fields for this technique.

Self-potentials are the results of the coupling between electrical and non-electrical flows/forces in the subsurface (Figure 3.1). One famous force/flux pair is Ohm’s law where the forces are the electrical potential gradients and where the conjugated flux is the electrical current density. Other examples of force/flux pairs are hydraulic gradients and fluid flow (Darcy’s law), chemical gradients and solute transport (Fick’s law), and thermal gradients and heat flow (Fourier’s law).

From Figure 3.1, we can see that it is possible to have contributions to any of the fluxes from any non-conjugated forces. In the case of electrical fluxes, self-potentials can have contributions from all four forces – electrical, hydraulic, chemical, and thermal gradient – and the associated mechanisms are called Ohm’s law, electrokinetic effect, electro-diffusion, and finally Seebeck effect which is clearly not of importance in this work.

The electrokinetic effect is the result of the transport, with groundwater flow, of an excess of electrical charges (ions) that exists at the pore scale (e.g., Ishido and Mizutani, 1981; Revil et al., 1999). As a consequence, self-potentials can be used to obtain information about groundwater flow (e.g., Corwin and Hoover, 1979; Sill, 1983; Fournier, 1989; Aubert and Atangana, 1996; Revil et al., 1999; Revil et al., 2005). The electro-diffusion is the result of the electro-chemical transport of ions due to gradients of their concentrations (e.g., Revil and Leroy, 2004; Maineult et al., 2004; 2005).

A third force creating self-potentials is related to redox reactions that can occur in the subsurface. Under a redox potential gradient, electrons that are liberated with redox reactions can flow through a metallic conductor (e.g., Sato and Mooney, 1960; Corry, 1985, Revil et al., 2009; 2010). In natural media, self-potentials associated with redox reactions can be measured in areas where metallic sulfide minerals (e.g., pyrite) dissemination occurred (e.g., Sato and Mooney, 1960; Corry, 1985) or where a burden metallic body is corroded (e.g., Castermant et al., 2008) as well as in landfills where redox fronts can appear with waste decomposition mechanisms (e.g., Naudet et al., 2003; 2004; Naudet and Revil, 2005; Arora et al., 2007, Linde and Revil, 2007) or in areas with others types of redox fronts (e.g., Maineult et al., 2006).

The total electrical current density $\mathbf{j}$ in A.m^{-2} can be written as the contribution of many mechanisms

$$\mathbf{j} = \sum_i \mathrm{j}_i \tag{3.1}$$

where j_i are for example the contributions of the four forces mentioned previously (see Figure 3.1).

If we are interested in only one of the mechanisms such as the electrokinetic effect, we can rewrite Eq. (3.1) as

$$\mathbf{j} = \mathbf{j}_c + \mathbf{j}_k \tag{3.2}$$

where $\mathbf{j}_k$ is the streaming current density related to hydraulic forcing and $\mathbf{j}_c$ is the familiar conduction current that can be written as

$$\mathbf{j}_c = \boldsymbol{\sigma}\mathbf{E} \tag{3.3}$$

where $\boldsymbol{\sigma}$ is the electrical conductivity of the subsurface (S.m^{-1}) and $\mathbf{E}$ the electrical field (V.m^{-1}) which can be written as the negative gradient of the electrical (self) potential field φ (V)

$$\mathbf{E} = -\boldsymbol{\nabla}\varphi \tag{3.4}$$

The familiar equation of current conservation is

$$\boldsymbol{\nabla} \cdot \mathbf{j} = 0 \tag{3.5}$$

Substituting Eq. (3.2) into Eq. (3.5) and then, separating the forcing from the electrical response gives

$$\boldsymbol{\nabla} \cdot (-\boldsymbol{\sigma}\boldsymbol{\nabla}\varphi) = \boldsymbol{\nabla} \cdot \mathbf{j_k} \tag{3.6}$$

showing that the streaming current density related to hydraulic forcing acts as a source of self-potentials.

Developing the left-hand term of Eq. (3.6) and considering Eq. (3.4) leads to an interesting point that one needs always keeping in mind when interpreting SP signals

$$\boldsymbol{\nabla}^2\varphi = \frac{\boldsymbol{\nabla}\boldsymbol{\sigma}}{\boldsymbol{\sigma}} \cdot \mathbf{E} - \frac{1}{\boldsymbol{\sigma}}\boldsymbol{\nabla} \cdot \mathbf{j_k} \tag{3.7}$$

Indeed, we can see in Eq. (3.7) that contrasts of electrical resistivity can be viewed as secondary sources of electrical current (first term of right-hand side of this equation). Moreover, primary sources – here, linked to groundwater flow – are also influenced by the electrical conductivity of the subsurface since the higher the electrical conductivity, the lower the amplitude of the SP anomalies. As a consequence, any SP profile needs to be interpreted with its corresponding electrical image whenever it is possible.

3.2. Streaming potential

Streaming potentials are the electrical self-potentials associated to the electrokinetic effect and are the result of the transport – with groundwater flow – of an excess of electrical charges – cations or anions – that exists at the pore scale (e.g., Ishido and Mizutani, 1981; Revil et al., 1999). This phenomenon can be explained by the Helmholtz-Smoluchowski equation and the electrical double layer (EDL).

At the pore scale, a small electrical potential is created with the drag of an excess of electrical charges with the fluid flow (Figure 3.2). This electrical potential is a function of the so-called zeta-potential ξ (in V) which can be defined as "*the potential at the distance from the pore wall where the electrical charge can be dragged with the fluid*" (Minsley, 2007). This distance – here named s – corresponds to the location of a shear plane that delimits two zones. The Helmholtz layer, situated near the pore wall, contains charges that are tightly bound to the surface of the minerals and this, for a distance $\mathrm{d} < \mathrm{s}$. The diffuse layer, situated at a distance $\mathrm{d} > \mathrm{s}$, corresponds to the area where the excess of charges can be dragged with the fluid movement since the electrical charges are not bound to minerals anymore. These layers create what we call the electrical double layer. The electrical potential that exists between the surface of the minerals and any point in the pore decays exponentially as a function of d.

The familiar Helmholtz-Smoluchowski equation governing streaming potentials at the pore scale is

$$\Delta\varphi = \frac{\varepsilon\,\xi}{\eta\,\sigma_f}\Delta P \tag{3.8}$$

where $\Delta\varphi$ is the electrical self-potential (in V), ε the electrical permittivity (in F.m^{-1}), η the fluid viscosity (Pa.s), σ_f the fluid electrical conductivity (S.m^{-1}), and ΔP the applied pore pressure (in Pa). ΔP can be written in terms of hydraulic gradient since it is equal to $\rho_f\, g\, \Delta h$, where ρ_f is the fluid density (kg.m^{-3}), g the acceleration due to gravity on Earth (m.s^{-2}), and Δh the difference in hydraulic heads.

Rewriting Eq. (3.8) in terms of hydraulic heads gives

$$\Delta\varphi = \frac{\varepsilon\,\xi}{\eta\,\sigma_f}\rho_f\, g\, \Delta h \tag{3.9}$$

or simply

$$\Delta\varphi = C'\,\Delta h \tag{3.10}$$

with

$$C' = \frac{\varepsilon\,\xi}{\eta\,\sigma_f}\rho_f\, g \tag{3.11}$$

Eq. (3.10) corresponds to the water table model that was used by many authors to image the water table distribution from SP signals (e.g., Fournier, 1989; Birch, 1993; 1998; Revil et al., 2003; Linde et al., 2007) or to monitor the drawdown/elevation of the water table during a pumping test (e.g., Rizzo et al., 2004) or an infiltration test (e.g., Revil et al., 2002). To apply Eq. (3.10), one needs to estimate the value of the (apparent) coupling coefficient C' that is defined in Eq. (3.11). This can be done in laboratory or in the field by measuring the SP signal between two points where the hydraulic head is known.

Even if Eq. (3.10) is a simple semi-empirical approximation of the reality since homogeneous electrical and hydraulic conductivity distributions are assumed, it is a convenient tool to understand the dynamics of groundwater systems. However, several authors used the full SP signals through different inversion schemes to find the Darcy velocities (e.g., Jardani et al., 2007) or to constrain the pattern of groundwater flow (e.g., Jardani et al., 2008). Bolève et al. (2009) used self-potential tomography to image preferential flow paths in an embankment dam. To do so, they used the new formulation of the electrokinetic effect developed by Revil and Leroy (2004) and Revil et al. (2005) which can be written as

$$\mathbf{j_k} = -\mathrm{Q_v}\,\mathbf{u} \tag{3.12}$$

where $\mathrm{Q_v}$ is the excess of electrical charges (C.m^{-3}) balancing the surface charge at the mineral/water interface and $\mathbf{u}$ is the Darcy velocity (m.s^{-1}) equal to

$$\mathbf{u} = -\,\mathbf{K}\,\boldsymbol{\nabla}\mathrm{h} \tag{3.13}$$

where K is the hydraulic conductivity of the medium (m.s^{-1}) and h the hydraulic head (m). The excess of charge $\mathrm{Q_v}$ is related to the streaming coupling coefficient C’ that is defined by Eq. (3.11)

$$\mathrm{C}' = \frac{\delta\varphi}{\delta\mathrm{h}} = -\frac{\mathrm{Q_v\,K}}{\sigma} \tag{3.14}$$

Therefore, the knowledge of C’ leads to the knowledge of $\mathrm{Q_v}$. Eq. (3.11) also shows that the coupling coefficient C’ depends on the fluid electrical conductivity and the higher the fluid electrical conductivity, the lower the coupling coefficient. This means that changes in hydraulic heads will result in stronger SP signals in the case of a purer water that is less electrically conductive. Other parameters such as the groundwater geochemistry including the temperature, pH, and salinity or hardness will also influence the coupling coefficient as it is shown in Darnet (2003). The new formulation of the electrokinetic effect also shows that the excess of charge depends on the hydraulic conductivity.

A great perspective of this new formulation will be to use the full SP signal in addition to ERT surveys to calibrate the hydraulic conductivity parameters of groundwater flow models.

3.3. Data acquisition and associated issues

The self-potential method consists in measuring the steady state and natural potentials existing on the ground surface (e.g., Fournier 1989) and SP profiling consists in moving one electrode along a profile while another electrode (called the base electrode) is left as a reference at a fixed SP station. The interval between every point depends on the objectives of the survey.

The amplitude of SP signals ranges from some mV up to some V depending the underlying effect. When dealing with mV which is generally the case when the electrokinetic effect is the dominant contribution of the signal, the expression ''improving the signal-to-noise ratio'' takes all its sense and measuring SP signals involves strong precautions.

A first and obvious general precaution before recording one SP measurement is to wait until the signal is stable. This stabilization is generally a matter of seconds. To estimate if a signal is stable or not, a general rule is that this signal does not change more than 15% of its value anymore (e.g., Corwin and Hoover, 1979; Naudet, 2004).

Sometimes, SP signals do not remain stable, especially when the distance from the base electrode increases. To fix this problem, we selected a new base electrode position on the profile every 40 m. Measurements need then to be corrected and reported to the first reference point. This involves an accurate measurement of the new reference position in both the old and new reference systems, as well as the stability of the new base position.

The distance of 40 meters that is used between two successive base electrode positions is guided by results in the field. Indeed, we saw that in some sites, the noise level increases with the distance from the base electrode (Figure 3.3). This phenomenon is clearly site-dependent since it is not retrieved everywhere.

Among more specific precautions, the use of a high internal impedance voltmeter (> 10^7 Ω) is essential to measure accurately low values of electrical potential (mV). 'Heavy duty' voltmeters are also recommended because of the heavy conditions that may occur during fieldworks (low or high temperature, humidity, mud...).

Except in some cases, stainless steel electrodes must be avoid for SP measurements since they will be polarized. Non polarizable electrodes (e.g., Petiau 2000) are then recommended. In this work, we used SDEC PMS 9000 (Pb/PbCl2) non polarizable electrodes from SDEC France. For further details on lead-lead chloride electrodes, see Petiau (2000). We also took another precaution by using only shielded electrical cables.

Like any electrical methods, the improvement of the electrical contact with the soil is crucial. This improvement can be achieved by digging holes (about 30 cm) and by filling these holes with an electrically conductive mud. In this work, we used a mud composed of NaCl saturated water and bentonite as suggested by many authors (e.g., Revil et al., 2002; Rizzo et al., 2004) and by the constructor of the non polarizable electrodes we used (SDEC France). This precaution also avoids measuring bio-potential due to plants roots.

Following these precautions and recommendations could improve, to a certain point, the signal-to-noise ratio and allow a better interpretation of the measured SP signals.

Knowing if a specific SP anomaly is physically related or is simply due to noise in the measured data, involves the estimation of the data noise level. This can be achieved by measuring the SP signal in several holes around the main SP station. In this study, we generally used from 3 to 5 measurements per station. The SP signal of a particular SP station is then the average value of these 3 to 5 measurements and the calculation of the standard deviation around this average value gives an estimation of the noise level. The base drift can generally be neglected given the short time that is needed to acquire an SP profile (Figure 3.4).

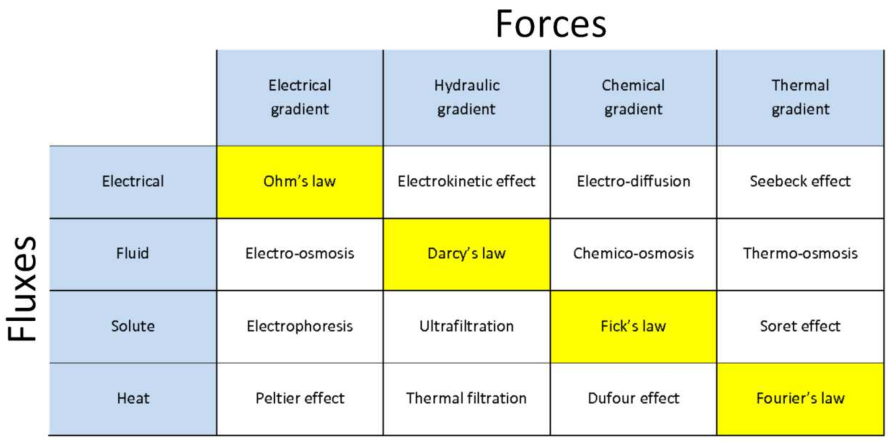

Forces

Fluxes

	Electrical gradient	Hydraulic gradient	Chemical gradient	Thermal gradient
Electrical	Ohm's law	Electrokinetic effect	Electro-diffusion	Seebeck effect
Fluid	Electro-osmosis	Darcy's law	Chemico-osmosis	Thermo-osmosis
Solute	Electrophoresis	Ultrafiltration	Fick's law	Soret effect
Heat	Peltier effect	Thermal filtration	Dufour effect	Fourier's law

Figure 3.1: With this coupled forces and fluxes table (from Minsley, 2007), we can see that self-potentials are the results of coupling between electrical (Ohm's law) and non-electrical flow and forces (electrokinetic effect, electro-diffusion, and Seebeck effect) in the earth. Streaming potentials are the results of only two couplings, namely Ohm's law and the electrokinetic effect.

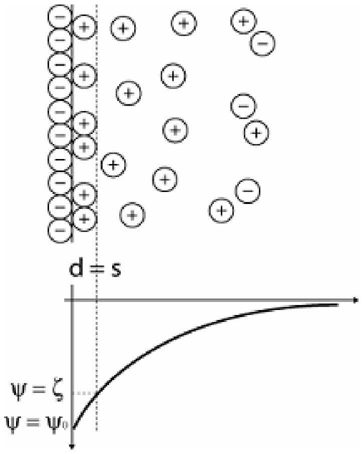

Figure 3.2: Schematic of the electrical double layer (from Minsley, 2007). At the pore scale, surface of minerals are generally not electrically neutral because of isomorphic substitutions that can occur in the minerals. The surface of the mineral – here negatively charged – is balanced by fixed opposite – here positive – ions within the Helmholtz layer (at a distance d < s), and a diffuse layer of ions farther from the interface (at a distance d > s) where the charges can be dragged with groundwater flow. The distance d = s corresponds to the shear plane that delimits both layers. The potential decays exponentially in the diffuse layer as a function of d. The potential at the distance d = s is called the zeta-potential.

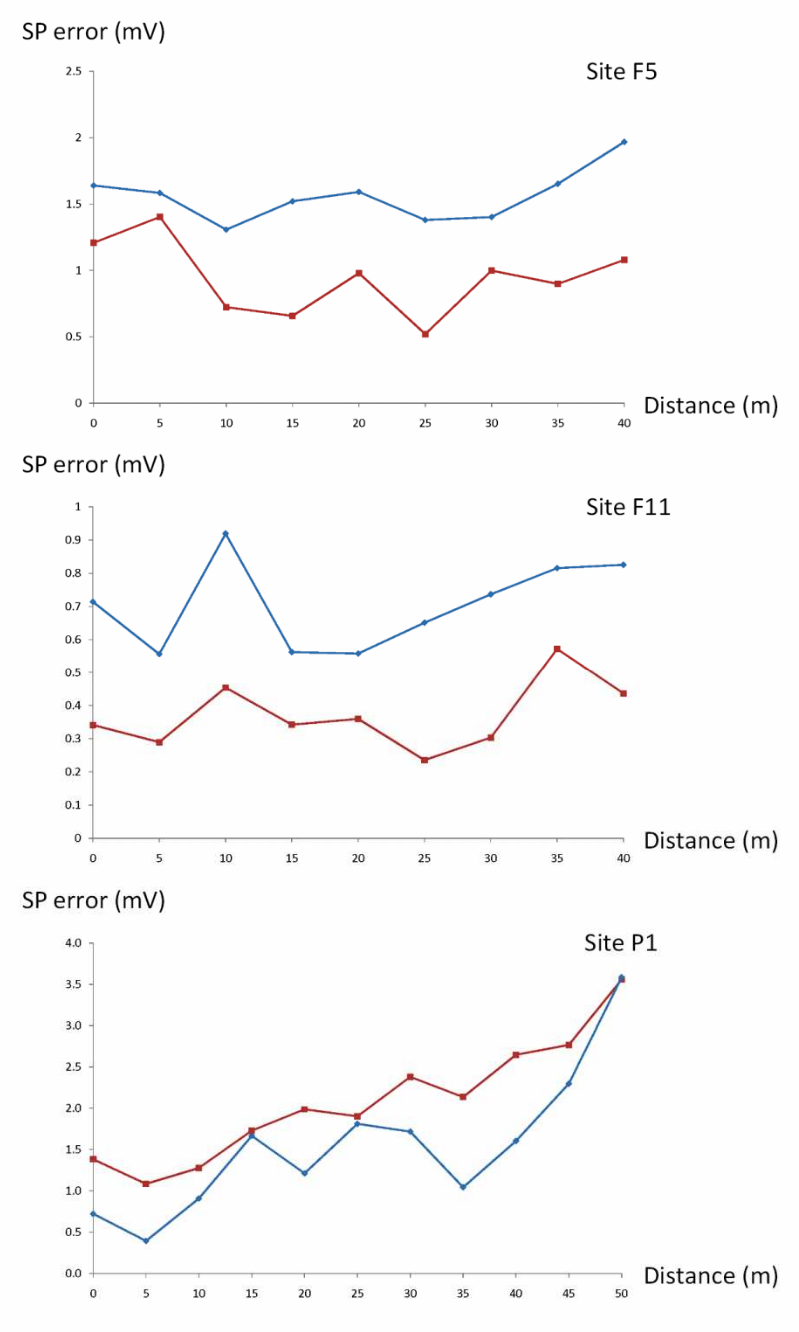

Figure 3.3: The noise level in the measured SP signal can sometimes increase with the distance from the base electrode. This phenomenon is site-dependent since it is retrieved only in site P1 even if these 3 sites are similar (carboniferous limestones of the Dinant and Namur Synclinoriums of southern Belgium). The blue (red) curve represents the mean (standard deviation) value of the combined SP errors per position. Selecting a new base electrode position after a certain distance (e.g., 40 m) could, in some cases, improve the signal-to-noise ratio.

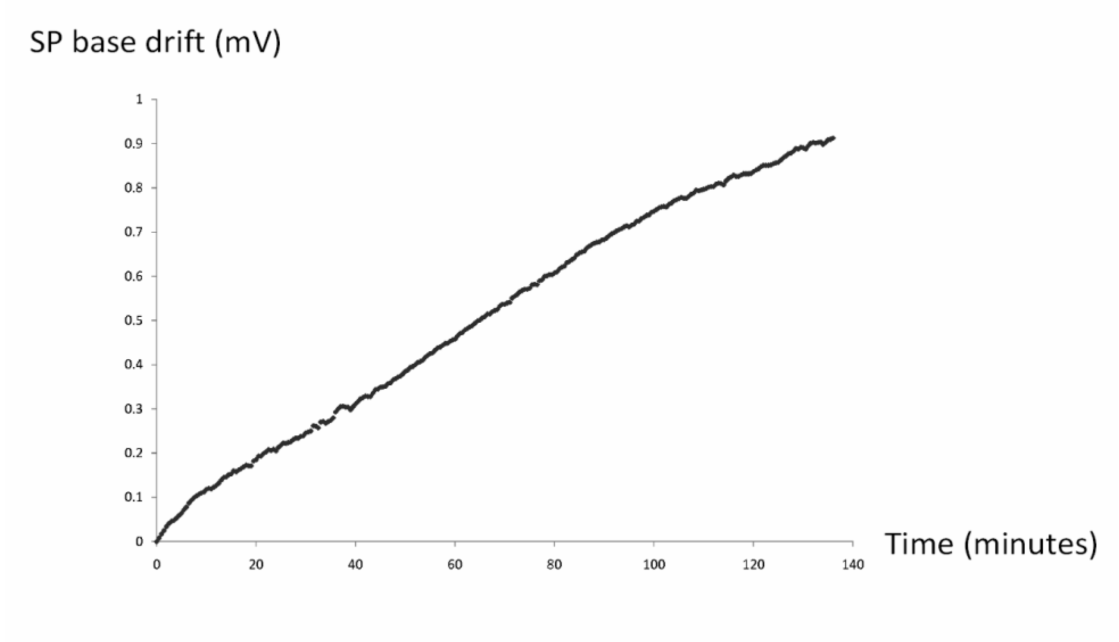

Figure 3.4: The natural drift that exists in the base electrode position needs to be taking into account when surveys are long (typically more than several hours). Our results showed that the drift is a bit less than 0.5 mV/h. The duration of our measurements was always less than 2 hours and the base drift was therefore neglected.

References

Arora, T., N. Linde, A. Revil, and J. Castermant, 2007, *Non-intrusive characterization of the redox potential of landfill leachate plumes from self-potential data*, Journal of Contaminant Hydrology, 92 (3-4), 274-292.

Aubert, M., and Q. Y. Atangana, 1996, *Self-Potential Method in Hydrogeological Exploration of Volcanic Areas*, Ground Water, 34 (6), 1010-1016.

Birch, F. S., 1993, *Testing Fournier's Method for Finding Water Table from Self-Potential*, Ground Water, 31 (1), 50-56.

Birch, F. S., 1998, *Imaging the Water Table by Filtering Self-Potential Profiles*, Ground Water, 36 (5), 779-782.

Bolève, A., A. Revil, F. Janod, J.L. Mattiuzzo, and J. J. Fry, 2009, *Preferential fluid flow pathways in embankment dams imaged by self-potential tomography*, Near Surface Geophysics, 7 (5-6), 447-462.

Castermant, J., C. A. Mendonça, A. Revil, F. Trolard, G. Bourrié, and N. Linde, 2008, *Redox potential distribution inferred from self-potential measurements associated with the corrosion of a burden metallic body*, Geophysical Prospecting, 56 (2), 269-282.

Corry, C. E., 1985, *Spontaneous polarization associated with porphyry sulfide mineralization*, Geophysics, 50 (6), 1020-1034.

Corwin, R. F., and D. B. Hoover, 1979, *The self-potential method in geothermal exploration*, Geophysics, 44 (2), 226-245.

Darnet, M., 2003, *Caractérisation et suivi de circulations de fluides par la mesure de Potentiels Spontanés (PS)*, Thèse de doctorat de l'Université Louis Pasteur – Strasbourg I (Spécialité Géophysique) (in French).

Fournier, C., 1989, *Spontaneous potentials and resistivity surveys applied to hydrogeology in a volcanic area: case history of the Chaîne des Puys (Puy-de-Dôme, France)*, Geophysical Prospecting, 37 (6), 647-668.

Ishido, T., and H. Mizutani, 1981, *Experimental and Theoretical Basis of Electrokinetic Phenomena in Rock-Water Systems and Its Applications to Geophysics*, Journal of Geophysical Research, 86(B3), 1763–1775, doi:10.1029/JB086iB03P01763.

Jardani, A., A Revil, A. Bolève, J. P. Dupont, W. Barrash, B. Malama, 2007, *Tomography of the Darcy velocity from self-potential measurements*, Geophysical Research Letters 34, L24403, doi:10.1029/2007GL031907.

Jardani, A., A Revil, A. Bolève, and J. P. Dupont, 2008, *Three-dimensional inversion of self-potential data used to constrain the pattern of groundwater flow in geothermal fields*, Journal of Geophysical Research, 113, B09204, doi:10.1029/2007JB005302.

Linde, N., and A. Revil, 2007, *Inverting residual self-potential data for redox potentials of contaminant plumes*, Geophysical Research Letters 34, L14302, doi:10.1029/2007GL030084.

Linde, N., A. Revil, A. Bolève, C. Dagès, J. Castermant, B. Suski, and M. Voltz, 2007, *Estimation of the water table throughout a catchment using self-potential and piezometric data in a Bayesian framework*, Journal of Hydrology, 334 (1-2), 88-98.

Maineult, A., Y. Bernabé, and P. Ackerer, 2004, *Electrical response of flow, diffusion and advection in a laboratory sandbox*, Vadoze Zone Journal, 3, 1180-1192.

Maineult, A., Y. Bernabé, and P. Ackerer, 2005, *Detection of advected concentration and pH fronts from self-potential measurements*, Journal of Geophysical Research, 110, B11205, doi:10.1029/2005JB003824.

Maineult, A., Y. Bernabé, and P. Ackerer, 2006, *Detection of advected, reacting redox fronts from self-potential measurements*, Journal of Contaminant Hydrology, 86 (1-2), 32-52.

Minsley, B. J., 2007, *Modeling and Inversion of Self-Potential Data*, Ph.D. Thesis of the Massachusetts Institute of Technology, Department of Earth, Atmospheric, and Planetary Sciences.

Naudet, V., A. Revil, J.-Y. Bottero, and P. Bégassat, 2003, *Relationship between self-potential (SP) signals and redox conditions in contaminated groundwater*, Geophysical Research Letters, 30 (21), 2091, doi:10.1029/2003GL018096.

Naudet, V., 2004, *Les méthodes de résistivité électrique et de potentiel spontané appliquées aux sites contaminés*, Thèse de doctorat de l'Université Paul Cézanne, Faculté de Droit, d'Économie et des Sciences d'Aix-Marseille III, 2004AIX30046 (in French).

Naudet, V., A. Revil, E. Rizzo, J.-Y. Bottero, and P. Bégassat, 2004, *Groundwater redox conditions and conductivity in a contaminant plume from geoelectrical investigations*, Hydrology and Earth System Sciences, 8 (1), 8-22.

Naudet, V., and A. Revil, 2005, *A sandbox experiment to investigate bacteria-mediated redox processes on self-potential signals*, Geophys. Res. Lett., 32 (11), L11405, doi:10.1029/2005GL022735.

Petiau, G., 2000, *Second generation of lead-lead chloride electrodes for geophysical applications*, Pure Applied Geophysics, 157, 357-382.

Revil, A., P. A. Pezard, and P. W. J. Glover, 1999, *Streaming potential in porous media. 1. Theory of the zeta potential*, Journal of Geophysical Research, 104(B9), 20021-20031, doi:10.1029/1999JB900089.

Revil, A., D. Hermitte, M. Voltz, R. Moussa, J.-G. Lacas, G. Bourrié, and F. Trolard, 2002, *Self-potential signals associated with variations of the hydraulic head during an infiltration experiment*, Geophysical Research Letters, 29 (7), doi:10.1029/2001GL014294.

Revil, A., V. Naudet, J. Nouzaret, and M. Pessel, 2003, *Principles of electrography applied to self-potential electrokinetic sources and hydrogeological applications*, Water Resources Research, 39 (5), 1114, doi:10.1029/2001WR000916.

Revil, A., and P. Leroy, 2004, *Constitutive equations for ionic transport in porous shales*, Journal of Geophysical Research, 109 (B3), B03208, doi:10.1029/2003JB002755.

Revil, A., P. Leroy, and K. Titov, 2005, *Characterization of transport properties of argillaceous sediments: Application to the Callovo-Oxfordian argillite*, Journal of Geophysical Research, 110 (B6), B06202, doi:10.1029/2004JB003442.

Revil, A., F. Trolard, G. Bourrié, J. Castermant, A. Jardani, and C. A. Mendonça, 2009, *Ionic contribution to the self-potential signals associated with a redox front*, Journal of Contaminant Hydrology, 109 (1-4), 27-39.

Revil, A., C. A. Mendonça, E. A. Atekwana, B. Kulessa, S. S. Hubbard, and K. J. Bohlen, 2010, *Understanding biogeobatteries: Where geophysics meets microbiology*, Journal of Geophysical Research, 115, G00G02, doi:10.1029/2009JG001065.

Rizzo, E., B. Suski, A. Revil, S. Straface, and S. Troisi, 2004, *Self-potential signals associated with pumping-tests experiments*, Journal of Geophysical Research, 109, B10203, doi:10.1029/2004JB003049.

Sato, M., and H. M. Mooney, 1960, *The electrochemical mechanism of sulphide self-potentials*, Geophysics, 25 (1), 226-249.

Sill, W. R., 1983, *Self-potential modeling from primary flows*, Geophysics, 48 (1), 76-86.

4. Studied sites in the Dinant Synclinorium

In this chapter, we describe the physical, geological and hydrogeological backgrounds of the Dinant Synclinorium, focusing on the Hoyoux River watershed where geophysical data was acquired in the context of this work. We then analyze the groundwater geochemistry of the different aquifers in relationship with the geoelectrical surveys results (sections 5, 6, and 7). We also briefly describe the physical, geological, hydrogeological and geochemical backgrounds of the Stavelot Massif where another test site (see Robert, 2007) lies.

During this Ph.D. thesis, we participated in the Synclin'Eau project (European Directive 2000/60/EC) whose main objective was to obtain a better state of knowledge about groundwater in the Dinant Synclinorium area. Our participation to this project allowed us to obtain useful information in the framework of this thesis. Details about the Synclin'Eau project can be seen in Brouyère et al. (2008; 2009a; 2009b; 2009c). However, the most significant characterization results are given hereafter.

4.1. Physical background

The Dinant Synclinorium is a geological structure located in the central part of the Walloon Region of Belgium (Figure 4.1), in the Liège and Namur Provinces (Figure 4.2). This geological structure can be assimilated with a region called Condroz. It is limited in the north by the Hesbaye Plateau, mainly composed of chalks and in the south by the Famenne depression, mainly composed of shales.

The Condroz region has a unique characteristic in terms of topography. This area is a succession of valleys and crests oriented in an E – W to NE – SW direction, which is the result of the differential erosion of the calcareous rocks and sandstones. Since they are less soluble, harder, and therefore less erodible than limestones, sandstones occupy topographical crests whereas limestones lie in the main valleys.

Another consequence of the better solubility of limestones can be seen with the numerous presence of paleokarsts filled with Ternary sediments (generally clay and sand). The karstic activity is still present and results in a high number of dolines or sinkholes, stream losses and resurgences, and caves. Therefore, the presence of karstic conduits cannot be neglected within the calcareous valleys. Section 5.2 presents pictures of limestone outcrops where karstic phenomena are present.

The investigated area is entirely located within the Meuse River watershed, more precisely in the Hoyoux River watershed which has an area of about 230 km² (Figure 4.3). Rivers are mainly located in the main calcareous valleys, even if some of these are dry valleys (Figure 4.5). As a consequence, the main drainage direction is the same as the geological structures direction, that is NE – SW.

The Hoyoux River (Figure 4.5) creates a transversal valley through the main synclinorium structure. This river flows from the south to the north near the city of Huy where it reaches the confluence with the Meuse River. It crosses therefore all other smaller rivers that are present in the calcareous valleys.

Altitudes range from approximately 320 meters on the ridges of the Hoyoux River watershed to 100 meters in the vicinity of the confluence with the Meuse River near the city of Huy. The difference in elevation between the bottom of the calcareous valleys and the sandstones crests is about 60 meters.

4.2. Geological background

The geology inside the Hoyoux River watershed is mainly a succession of calcareous synclines and sandstones anticlines (Figure 4.5 and Figure 4.6). The succession of synclines and anticlines is the result of the Variscan Orogeny that folded the area in this characteristic structure. Full details about the local geology can be found in Bultynck et al. (2001b) and Poty et al. (2001), or in French, in Boulvain and Pingot (2012).

The geological formations that are present in the Hoyoux River watershed can be separated in two categories:

- Primary formations from early Devonian to Namurian which constitute the bedrock and,
- Ternary formations, mostly sand and clay that can overlay the Primary bedrock or more often, fill paleokarsts.

The main aquifers lie within the Primary bedrock, essentially within the Carboniferous limestones and the late Famennian sandstones. Geological formations were gathered together to create mega units that present the same hydrogeological behavior (Figure 4.4). Therefore, in this work, we will always refer to these mega units when we use the term "*formation*" if nothing else is specified. We followed the classifications and appellations used in the Hydrogeological Map of Wallonia (see also section 4.3). In the following description of these units, we will only mention the principal characteristic for clarity.

Early Devonian is composed of silty formations, sandstones and quartzites that are occasionally separated with shaly layers. These formations are the result of detritic sedimentation and are only present in the northern part of the Hoyoux River watershed.

Frasnian – Givetian formations are characterized by a deeper marine environment related to a strong marine transgression that happened during Frasnian and Givetian. This results in more calcareous formations, generally limestones and dolomites but also shales and calcareous sandstones. During late Frasnian, a marine regression started and Famennian corresponds to this important regression episode. As a consequence, Famennian – Frasnian formations are essentially composed of shales. All these formations are mostly present in the northern part of the watershed but can be locally retrieved elsewhere due to fault activity. Early Devonian, Frasnian – Givetian, and Famennian – Frasnian formations were not investigated during this Ph.D. thesis.

Late Famennian formations coincide with the sandstone anticlines that are major aquifers in southern Belgium because they are locally highly fractured. These sandstones have generally calcareous cementation. An early Tournaisian shale formation separates late Famennian sandstone anticlines and late Tournaisian – Visean calcareous synclines. These late Tournaisian – Visean calcareous formations are the result of a marine carbonated sedimentation. These calcareous rocks – limestones that can be locally dolomitized – form major fractured aquifers. Indeed, they are locally highly fractured and Visean limestones are extremely soluble which leads to numerous karstic phenomena as evidenced by the presence of numerous dolines or sinkholes in some areas. Formations from late Famennian to Visean are present everywhere in the Hoyoux River watershed except in the northern part.

Finally, Namurian formations which are less present in the watershed, are the result of sedimentation in a coastal environment. Sometimes, these Namurian formations, generally composed of shales with some sandstone intercalation, can occupy the heart of some synclines. These formations were not investigated during this Ph.D. thesis.

To summarize, the Hoyoux River watershed is mainly composed of late Tournaisian – Visean calcareous synclines and late Famennian sandstone anticlines that are separated by an early Tournaisian shale layer. In this Ph.D. thesis, we mainly investigated the calcareous synclines with geophysics but we need information about the sandstone anticlines and the shale layer to conceptualize the groundwater flow model of a typical calcareous syncline (section 7.1).

4.3. Hydrogeological background

In this section, we used the same convention as the one used in the Hydrogeological Map of Wallonia (e.g., Hallet et al., 2000). Geological formations are gathered together to form mega units – hydrogeological units – that possess the same hydrodynamic properties such as the permeability. According to this convention, three different appellations are used:

- An aquifer is a permeable hydrogeological unit that contains enough water to be supplied,
- An aquitard is a semi-permeable hydrogeological unit that allows groundwater flow at low velocity,
- An aquiclude is a hydrogeological unit with very low hydraulic conductivity and in which, it is impossible at present to economically exploit water.

The geological description (see previous section) was already performed using these mega units. Among the hydrogeological units present in the Hoyoux River watershed, we describe below only the formations that were investigated during our geophysical surveys, which are the late Famennian sandstones, the early Tournaisian shales, and the late Tournaisian – Visean limestones forming the succession of synclines and anticlines that is characteristic of the region.

The late Famennian sandstones occupy the topographical crests and are related to anticlines. These sandstones are generally fractured and weathered and form therefore good aquifers. The early Tournaisian aquiclude is a succession of shale and limestone layers. The shale layers are quite impermeable and form hydraulic barriers between the late Famennian sandstones and the late Tournaisian – Visean limestones. The latter occupy the valleys and are related with synclines. They are locally highly fractured and karstified and form therefore one of the major aquifers of southern Belgium. About 52% of the Belgian drinking water is extracted from these Carboniferous limestones (Delloye et al., 2011).

In the central part of the Hoyoux River watershed, the Carboniferous limestones are not separated by the late Famennian sandstone anticlines anymore due to the submergence of the folds. Therefore, in these areas where sites F6, F7 and, F12 are situated (Figure 4.5), hydrogeological limits are not well defined in contrary of well-defined synclines such as the ones where sites F3, F5, F10 and, F11 are situated.

The Hoyoux River is either in equilibrium with groundwater (in the southern part) or is draining the different calcareous valleys toward it (Brouyère et al., 2009a; 2009b; 2009c). This implies that the main groundwater flow direction in the calcareous synclines is along the geological structures direction, that is NE – SW. A second flow direction, perpendicular to the main flow direction, is related to the flanks of these valleys (Figure 4.7).

In the sandstone anticlines, the water table is quite shallow – generally a few meters deep – and groundwater flow follows the topography (Brouyère et al., 2009a; 2009b; 2009c). As a consequence, groundwater flows from the sandstone crests directly toward the calcareous valleys, in a NW – SE direction. However, the impermeable shale layers separating both aquifers act as hydraulic barriers, excepting in locations where these shales are more fractured. Numerous springs are then present along these impermeable shale units. Water then runoffs on this impermeable unit and infiltrates again in the calcareous valleys. The hydrodynamics of a typical succession of sandstone crests and calcareous valleys is presented in Figure 4.8.

4.3.1. Flow properties

Strong hydraulic gradients are generally present in well-defined calcareous valleys, with about 1% for the main hydraulic gradients along the geological structures direction and between 0.5 and 2% for the hydraulic gradients related to the flanks of the valleys. In large and not well-defined calcareous synclines, these values are sometimes one to two orders of magnitude lower.

A statistical analysis of pumping tests results was performed within the Dinant Synclinorium (Brouyère et al., 2009a; 2009b; 2009c) in order to estimate the variability of hydraulic conductivity values for both the sandstone and calcareous aquifers. Results showed that the hydraulic conductivity in the late Famennian sandstones ranges between $7x10^{-7}$ and $5x10^{-4}$ m/s. The variation of hydraulic conductivity is then over 3 orders of magnitude. Higher values are generally related with more fractured areas.

For the Carboniferous limestones, the variation of hydraulic conductivity is higher with about 6 orders of magnitude and values range between $4x10^{-10}$ and $2.5x10^{-3}$ m/s. This heterogeneity is characteristic of fractured aquifers with low primary porosity. Another statistical analysis also showed that the hydraulic conductivity was dependent on the topography with higher values retrieved in the valleys and lower values retrieved in the flanks. The bottoms of the calcareous valleys are generally more fractured since they are related with the syncline fold axis where higher stresses exist.

New piezometers were drilled in zones with little hydrogeological data including our studied sites (all in Carboniferous limestone aquifers). Pumping tests were then realized and analyzed to estimate the hydraulic conductivity of these zones which are mostly fractured zones according to our geophysical surveys (see section 5.3). The water table elevation, the hydraulic conductivity as well as other geographical information for each piezometer are given in Table 4.1.

In these investigated sites, the water table depth ranges between 8 and 44 m below surface but in some piezometers, this depth could reach up to 100 m (if not more). This is a characteristic of karstic aquifers. In the Hoyoux River watershed, the water table depth increases from south to north. This is a consequence of the Meuse River that flows in the north and that imposes a base level to groundwater in the Dinant Synclinorium aquifers.

Finally, the early Tournaisian shale unit possesses lower hydraulic conductivity with a mean value of about 10^{-7} m/s. However, these shales can be locally permeable where fractured zones exist. This unit is considered as an aquiclude and is almost not exploited for drinking water supply in contrary of the Carboniferous limestones and the late Famennian sandstones.

Here, fractures or karsts play an important role in groundwater flow since they lead to preferential paths. It is therefore crucial to develop methods to locate and characterize these fractures and karsts or more generally, a fractured area in order to better understand these aquifers.

4.3.2. Transport properties

Classic tracer tests were performed in both the late Famennian sandstone and the late Tournaisian – Visean calcareous aquifers (Brouyère et al., 2009a; 2009b; 2009c). These tests allowed us to quantify some transport properties such as the first arrival velocity and the longitudinal dispersivity.

Two tests were performed in the Dolembreux site (Caterina, 2007), in a sandstone crest. A tracer solution was injected in a piezometer whereas the tracer was recovered in a pumping well that is used for drinking water supply. The distance between the injection piezometer and the recovery well was 50 m for the first test and 70 m for the second test. The first arrival velocity is clearly below 1 m/h with values of about 0.1 m/h and the longitudinal dispersivity is about 20 m.

Nine tracer tests were realized in calcareous valleys to estimate transport properties within a karstic system and to relate losses with resurgences. The tracer solutions were injected directly in known losses whereas they were recovered in different known resurgences. The distance between the injection and recovery points covered by these tests ranges from 650 to 8000 m. The first arrival velocity is extremely variable in these karstic systems but it is generally higher in the calcareous valleys than in the sandstone crests with values ranging between 3.8 and 226 m/h. The longitudinal dispersivity is also highly variable with values ranging between 4 and 90 m.

4.4. Groundwater geochemistry

We collected more than 200 groundwater samples from wells, piezometers, and springs to characterize the groundwater geochemistry of the different hydrogeological units that compose the investigated area (Figure 4.9). We collected these samples twice, during summer 2007 and winter 2007-2008, to study eventual seasonal changes in the groundwater physico-chemical parameters. In this section, we will only summarize the information concerning two hydrogeological units, the late Famennian sandstones and the Carboniferous limestones. For full details about this study, see Brouyère et al. (2008).

We collected 145 groundwater samples in both aquifers with 110 for the Carboniferous limestones and 35 for the late Famennian sandstones. Many physico-chemical parameters were analyzed including the pH, the temperature, the specific electrical conductivity and, the total hardness. Major ions concentrations were also analyzed in order to define a mean physico-chemical characteristic of each mega unit.

Some slight seasonal variations seem to exist for some parameters such as the pH, but no clear seasonal variations were highlighted for the specific electrical conductivity and the total hardness (Figure 4.10). The temperature varies between 9 and 12°C depending the site, but seasonal changes in the same sites are very low – about 0.1°C in site F11 (Figure 4.12). Therefore, changes in temperature or in the groundwater composition should not affect a long term (and even more, a short term) geoelectrical monitoring since corresponding changes in bulk electrical resistivity would be of 0.2% (e.g., Hayley et al., 2007).

Since there is no significant difference between samples from different seasons, we will only focus on results from one season – summer – in the rest of this section.

4.4.1. The Carboniferous limestone aquifers

Groundwater dissolved minerals in the Carboniferous limestone aquifers are mainly composed of calcium and magnesium carbonates. The main characteristics of these aquifers are their relatively high electrical conductivity and their high total hardness. We estimated a representative groundwater composition which is presented in Table 4.2.

The pH is around 7.5 and therefore, Carboniferous limestone groundwater is neutral to basic. However, the range of values goes from 7 to 8.5 approximately. This indicates more basic groundwater.

The specific electrical conductivity (at 25°C) is generally comprised between 330 and 1100 µS/cm. The mean value is approximately equal to 670 µS/cm with a standard deviation value of 170 µS/cm. In terms of specific electrical resistivity, this corresponds to values ranging between 9 and 30 Ω.m. The knowledge of this parameter is extremely useful to derive the electrical formation factor from ERT images and so, to obtain information about the porosity (here, mostly fractures and karsts).

The total hardness is high with values ranging between 15 and 55°fr. Indeed, the mean value is approximately equal to 35°fr with a standard deviation value of about 10°fr. This is not surprising since it is a characteristic of carbonated aquifers (strong concentrations of calcium and magnesium).

We acquired new samples in the framework of this work in August 2009 in all new piezometers drilled in summer 2008. Groundwater was pumped with a flow rate of 2 m^3/h during half an hour till the measured parameters were stable. The temperature and the specific electrical conductivity were then taken using the YSI 650 MDS multi parameters probe. The temperature ranges between 9 and 12°C and Figure 4.12 presents the electrical resistivity values for each study site. This new data set was essential to estimate the electrical formation factor at the sites where geophysics was performed, in order to estimate the degree of fracturation (Robert et al., In preparation).

4.4.2. The late Famennian sandstone aquifers

The late Famennian sandstones contain also carbonated minerals since the cementation around the silicate grains is carbonated. Therefore, it is not surprising that groundwater in these sandstone aquifers possess characteristics of carbonated aquifers. The mean composition of a late Famennian sandstone aquifer is presented in Table 4.2.

The pH is around 7 and therefore, late Famennian sandstone groundwater is more neutral compared to Carboniferous limestone groundwater.

The specific electrical conductivity has a mean value of about 455 µS/cm and a standard deviation value of about 125 µS/cm. Since the distribution of this parameter is Gaussian, 96% of the samples present values of specific electrical conductivity between 205 and 705 µS/cm. In comparison with the Carboniferous limestone aquifers, this parameter is almost divided by two.

The total hardness is also almost divided by two compared to the Carboniferous limestone aquifers. Values range between 8 and 36°fr. The mean value and the standard deviation values are approximately equal to 22 and 7°fr, respectively. With such values, groundwater can still be characterized as hard, even if it is less than for the Carboniferous limestones.

According to these results, the discriminating parameters between both aquifers are the pH, the electrical conductivity and, the total hardness which is related to the concentrations of calcium, magnesium, and carbonates.

4.5. The Stavelot Massif

The Stavelot Massif is a geological structure situated in the eastern part of the Walloon Region of Belgium, in the Liège Province (Figure 4.2). This geological structure can be assimilated with the north-eastern part of the Ardennes and comprises the High Fens plateau. Altitudes range from about 300 m up to 694 m, the highest point of Belgium.

The Stavelot Massif is mostly composed of quartzites and phyllades from Cambrian and Ordovician (Figure 4.13). It is separated in two parts by the Malmedy Graben that has a SW – NE direction. The Malmedy Graben is filled with Permian pudding stones that are considered as an aquifer (Figure 4.14). The Stavelot Massif underwent two orogenies, the Caledonian and the Variscan orogenies. Thus, the tectonics of the Stavelot Massif is quite difficult to describe since it is highly folded and fractured. Further geological information or description about the Stavelot Massif can be found in Bultynck et al. (2001a) and Verniers et al. (2001) or in French, in Boulvain and Pingot (2012), Geukens (1986; 1999), and Vandenven (1990).

Our test site is situated in a village outside the town of Malmedy and the local geology is only composed of Cambrian quartzites of the Deville group and more precisely of the Bellevaux geological formation (Dv2). Since this site is lying next to the Malmedy Graben, the entire area is extremely fractured, as it can be evidenced in nearby outcrops. The topography in the area is extremely steep as it can be evidenced in Figure 4.14 and Figure 4.15.

From a hydrogeological point of view, the Cambrian quartzites of the Deville group are part of the Cambrian – Ordovician aquiclude. However, this hydrogeological unit can be locally highly fractured and therefore contains aquifer layers.

Two different aquifers – a shallow aquifer in the weathered bedrock and a much deeper aquifer related to fractured areas – exist (Figure 4.14). The deep aquifer is constrained by the Warche River and by the Amblève River that flow nearby (Figure 4.14 and Figure 4.15). In this work, we only investigated the upper shallow aquifer in the weathered bedrock.

A spring draining this shallow aquifer is present in our test site and in April 2008, we analyzed a groundwater sample. We measured the specific electrical conductivity at 70 µS/cm, the pH at 5.9, and the total hardness at 2°fr. Therefore, groundwater can be described as electrically resistive, acidic, and very soft.

These low values of the different physico-chemical parameters are in good agreement with the groundwater geochemical analysis results of Robert (2007) where we acquired and analyzed 45 groundwater samples in springs and wells of the area. These results present a specific electrical conductivity ranging between 30 and 180 µS/cm. The total hardness ranges between 0.6 and 5.2°fr whereas the pH ranges between 3.7 and 7.

The shallow aquifer that we investigated responds directly to rainfall events since local drinking water exploitations (mostly drains) generally contain mud when violent rainfall events occur.

The hydraulic gradients associated to the shallow and the deeper aquifers are in relation with the topography. Therefore, in our site, where a spring is present, groundwater flows from SE toward NW in the direction of the Warche River (Figure 4.14). This spring drains groundwater from several fractures upstream. We performed a geoelectrical survey – electrical resistivity tomography and self-potential – to identify the geophysical signature of this shallow preferential flow path (Robert, 2007; section 5.1).

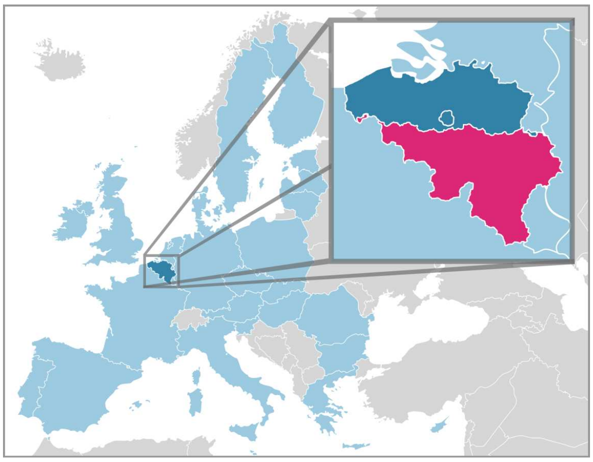

Figure 4.1: The area investigated in this work lies in southern Belgium (in red), more precisely in the Walloon Region of Belgium (Ssolbergj, 2008).

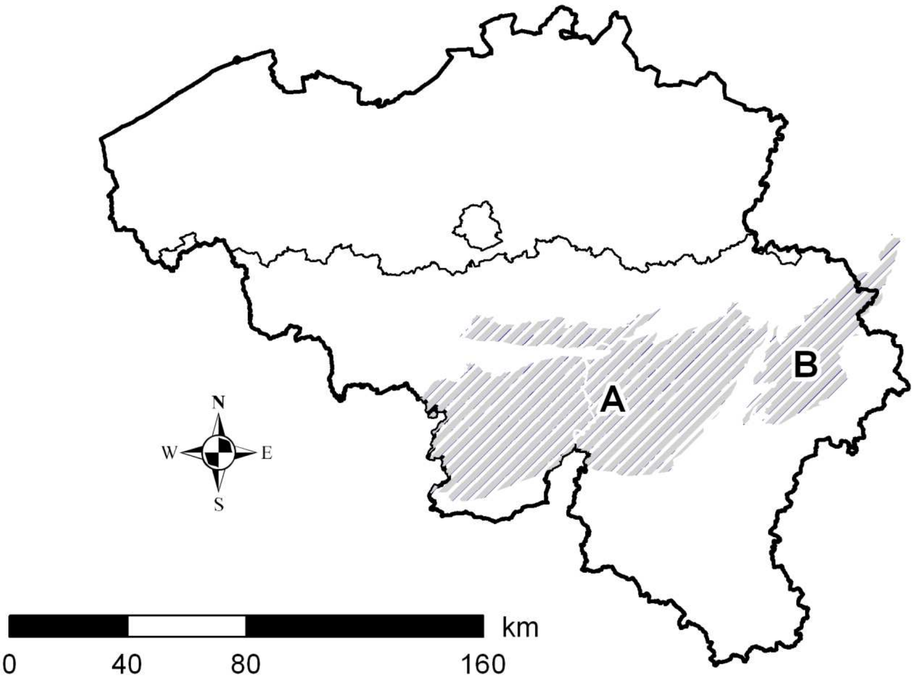

Figure 4.2: The Dinant Synclinorium (A) lies in the central part of the Walloon Region of Belgium whereas the Stavelot Massif (B) lies in eastern Belgium.

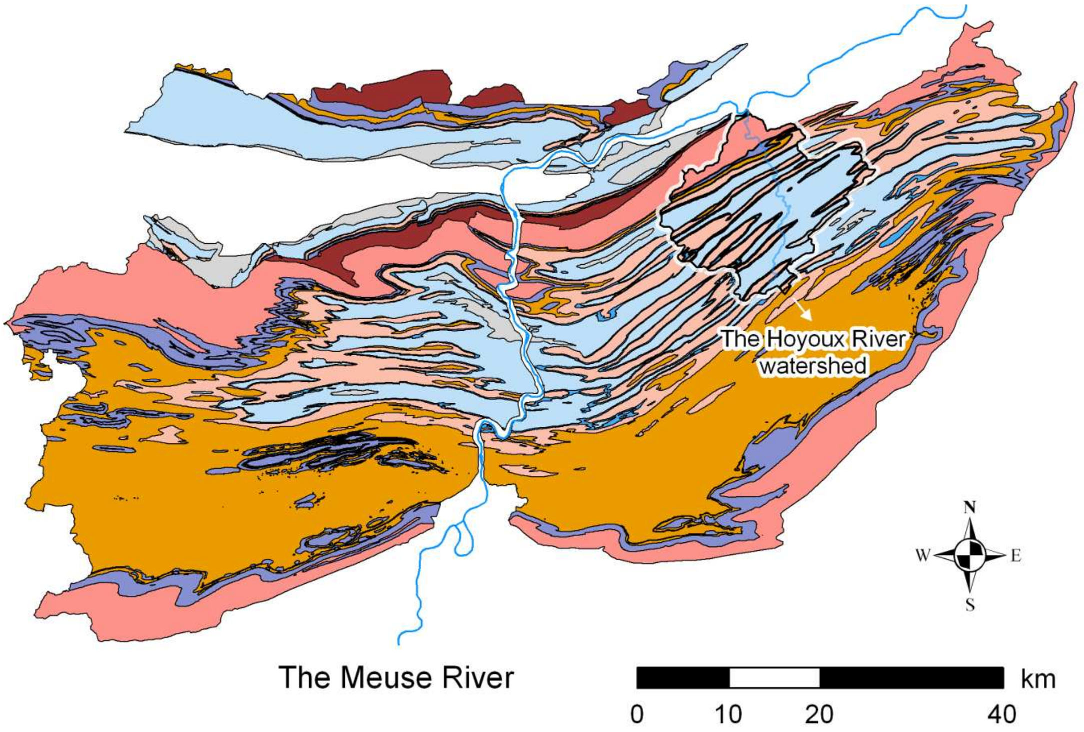

Figure 4.3: The area we investigated during the Synclin'Eau project can be assimilated to the Condroz region which is located in the Meuse River watershed (see Figure 4.4 for the color legend). The area is mainly composed of the Namur and Dinant Synclinoriums which are – in a simplified view – a succession of calcareous valleys and sandstone crests. In this Ph.D. thesis, we focused our studies on the Hoyoux River watershed situated in the north-eastern part of the Dinant Synclinorium.

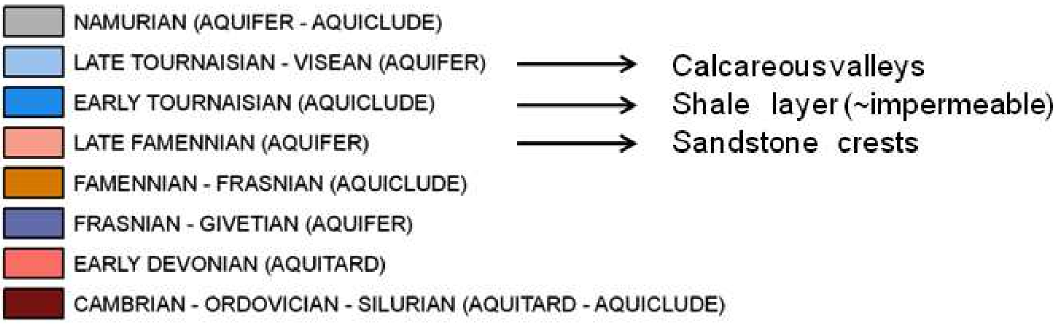

Figure 4.4: Color legend of the different hydrogeological units. A simplified version integrating the calcareous valleys, the sandstone crests and, the impermeable shale layer in between is also proposed.

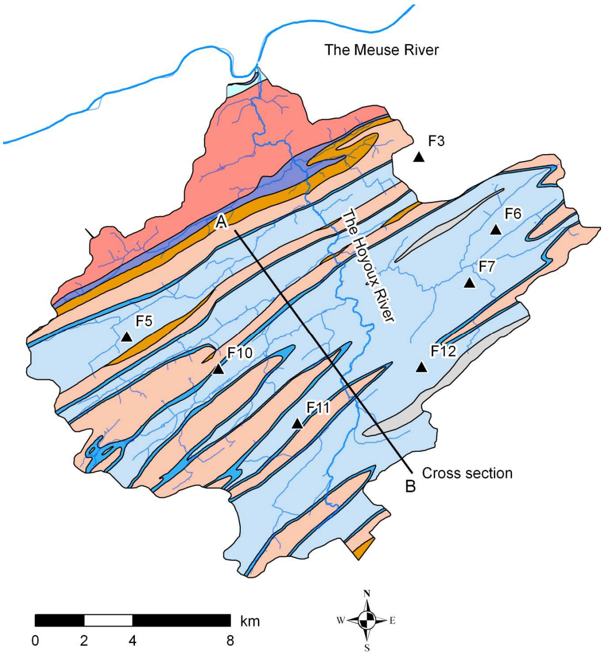

Figure 4.5: We focused our studies on the Hoyoux River watershed. We investigated seven different sites – named F3, F5, F6, F7, F10, F11 and, F12 – which are all located in a calcareous valley. These sites correspond to areas where little hydrogeological information is present. The Hoyoux River creates a transversal valley within the geological structures. All other rivers lie in some calcareous valleys and flow toward the Hoyoux River. See Figure 4.4 for the color legend.

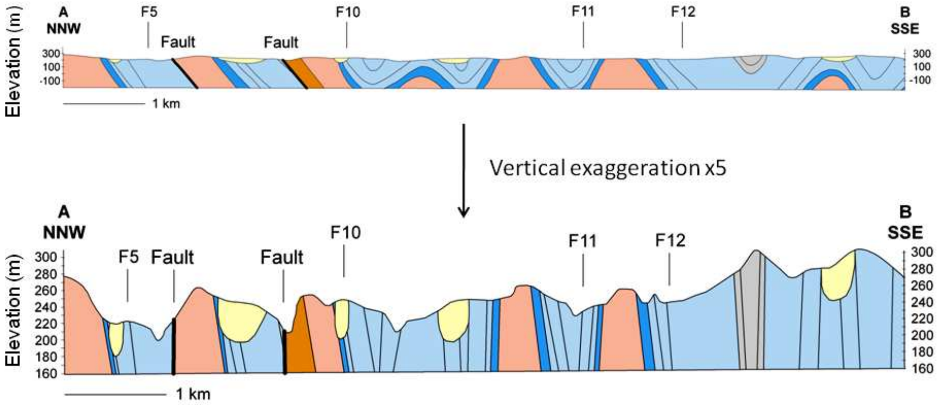

Figure 4.6: This cross section shows the succession of calcareous synclines and sandstone anticlines (top) and the relation between the geology and the rolling topography (bottom). Indeed, calcareous synclines correspond to valleys whereas sandstone anticlines correspond to crests. It is a result of the differential erosion that occurred between limestones and sandstones. Some site positions are also projected on this cross section. See Figure 4.4 for the color legend.

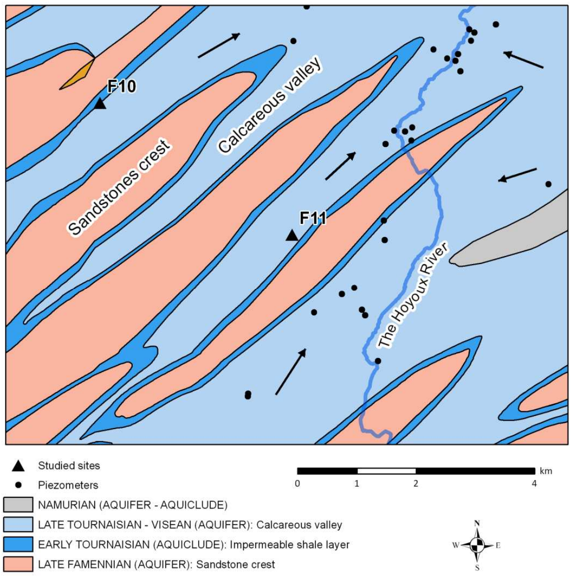

Figure 4.7: The sites we investigated are areas with little hydrogeological information as it can be seen by the absence of piezometers in these areas. The main groundwater flow direction (arrows) is generally along the geological structures, that is NW – SE. This gradient is related to the Hoyoux River that imposes a base level to the aquifers. A second gradient, perpendicular to the main groundwater flow direction and related to the flanks of valleys is also present in well-defined synclines. Another contribution to this second hydraulic gradient comes from the Meuse River that also imposes a base level to the aquifers of the Hoyoux River watershed. The closest from the Meuse River, the more dominant this contribution is.

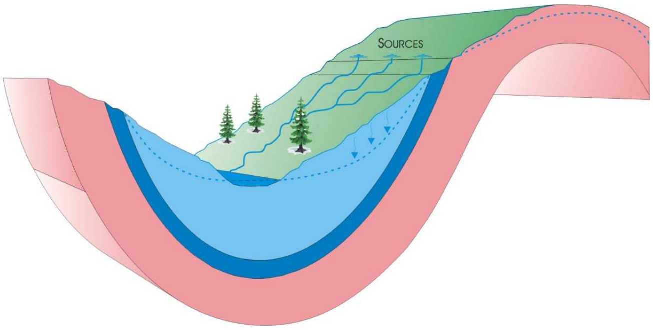

Figure 4.8: This conceptual model of a typical Condruzian system shows that groundwater discharges appear in the contact between the sandstone aquifer (pink) and the shale hydraulic barrier (dark blue). Then, water either runoffs from the springs along the topography and/or recharges the limestone aquifer (light blue). Small rivers are sometimes present in the bottom of the valleys and can be either draining or losing (e.g., the Havelange syncline where the site F11 lies).

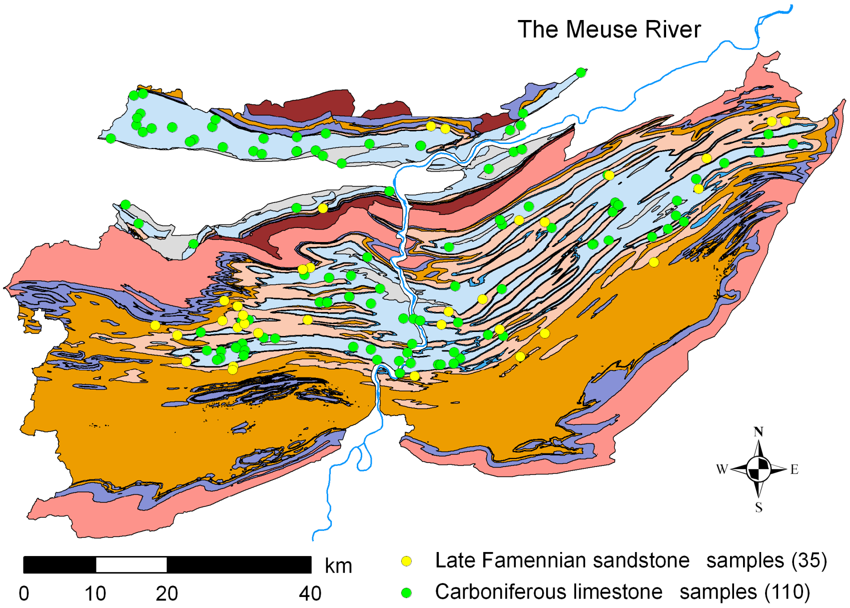

Figure 4.9: Groundwater sampling locations of the different hydrogeological units are given here. If we only focus on the two aquifers that were investigated in this Ph.D. thesis, it represents 110 samples from the Carboniferous limestones and 35 samples from the late Famennian sandstones. This map does not take into account the samplings in the new piezometers (Robert et al., 2011; section 5.3).

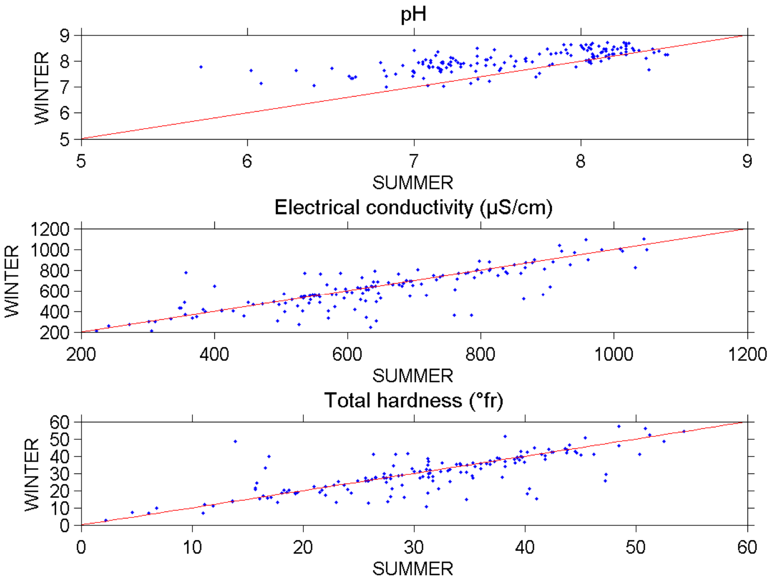

Figure 4.10: These seasonal scatterplots – summer vs. winter – show that the three main physico-chemical parameters – pH, electrical conductivity, and total hardness – do not vary much during the seasons. Only the pH seems to vary slightly in the lowest values (pH < 7).

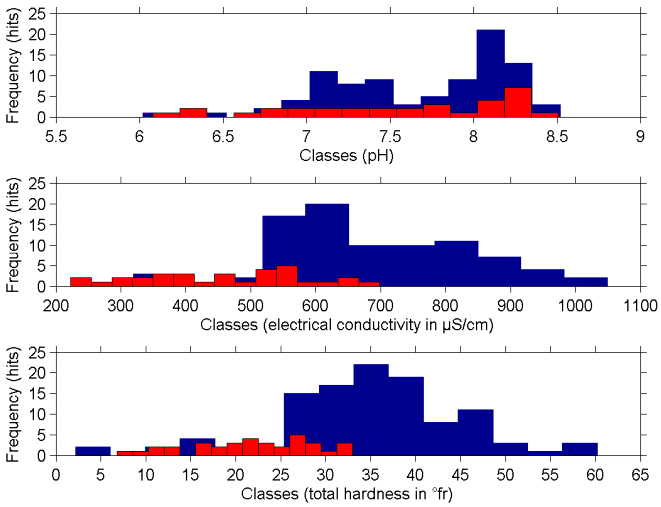

Figure 4.11: These histograms show that the late Famennian sandstones (in red) and the Carboniferous limestones (in blue) do not present the same physico-chemical parameters distribution, except for the pH. Indeed, both aquifers have basic groundwater with pH values mostly ranging between 7 and 8.5, but the pH distribution in limestones possesses two different populations. The groundwater electrical conductivity distribution is not similar between both aquifers. Limestones present higher values ranging from 500 up to 1100 µS/cm whereas sandstones – with calcareous cementation – present values ranging between 200 and 700 µS/cm. The total hardness – the sum of calcium and magnesium concentrations – presents a similar behavior with lower values for sandstones – from 5 up to 35°fr – than for limestones – from 10 up to 60°fr.

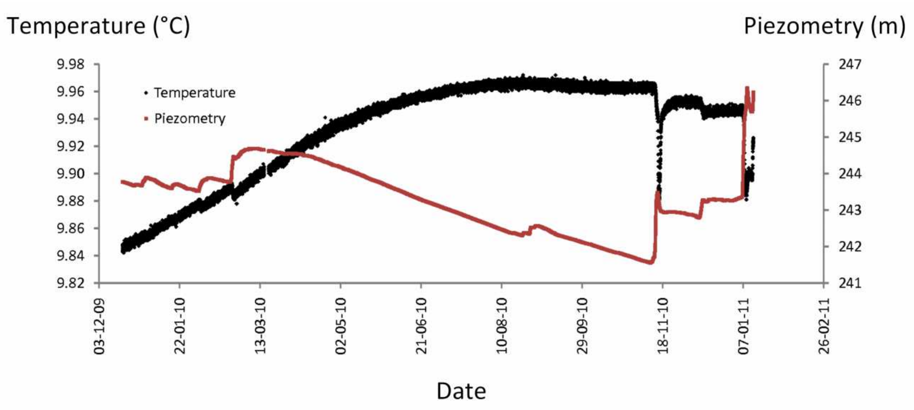

Figure 4.12: The maximum seasonal change in temperature is about 0.10°C in F11 whereas the maximum change in the water table elevation is about 5 m. Further developments on the monitoring surveys are presented in section 6.1.

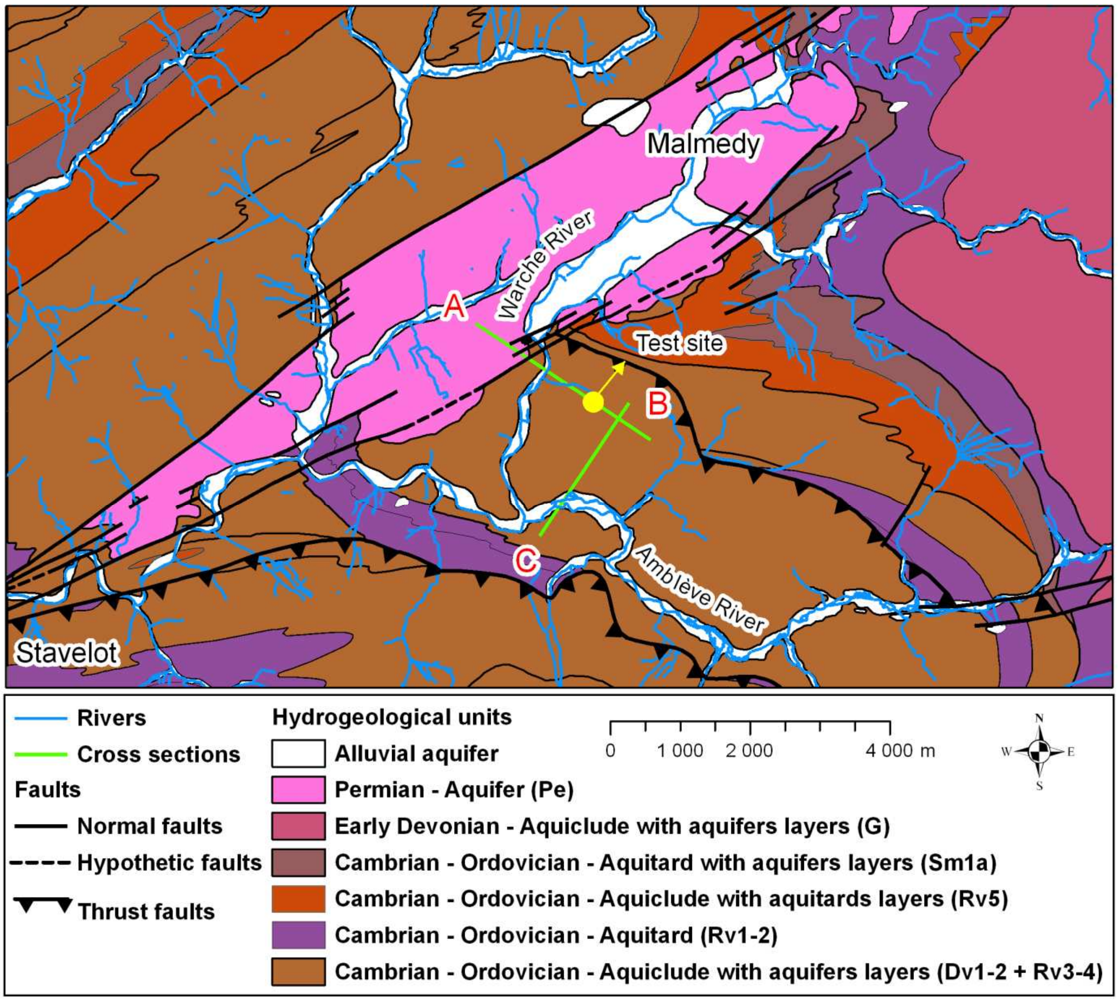

Figure 4.13: The Stavelot Massif is separated in two parts by the Malmedy Graben (Pe). The area is highly folded and fractured, especially near our test site that is lying in the Cambrian aquiclude unit (Dv2). This unit contains deep aquifer layers that are related with more fractured areas. In the investigated area, these aquifers are constrained by the Warche (AB cross section in Figure 4.14) and Amblève rivers (CB cross section in Figure 4.15). Here, we only investigated the shallow aquifer in the weathered part of the bedrock (few first meters) which is highlighted by the presence of a small spring. This figure is based on the hydrogeological map of Stavelot-Malmedy 50/5-6 that is currently in preparation (Gilson et al., In preparation).

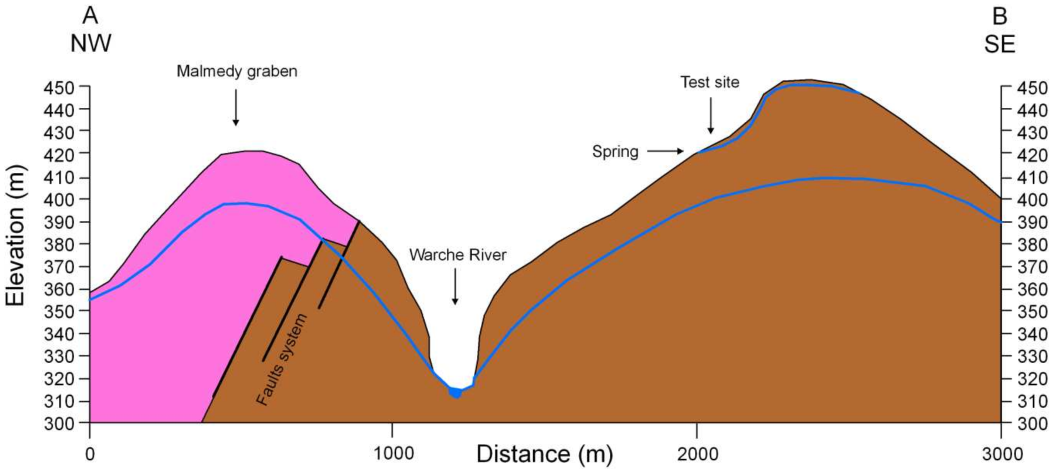

Figure 4.14: This AB cross section is a schematic representation of the geology and hydrogeology of the area. Two different aquifers – a shallow aquifer in the weathered bedrock and a much deeper aquifer related to fractured area – exist. The deep aquifer is constrained by the Warche River that flows nearby as well as by the Amblève River (Figure 4.15). We investigated the first and shallow aquifer that is related to the fractured and weathered part of the quartzite bedrock (Robert, 2007). See Figure 4.13 for the color legend.

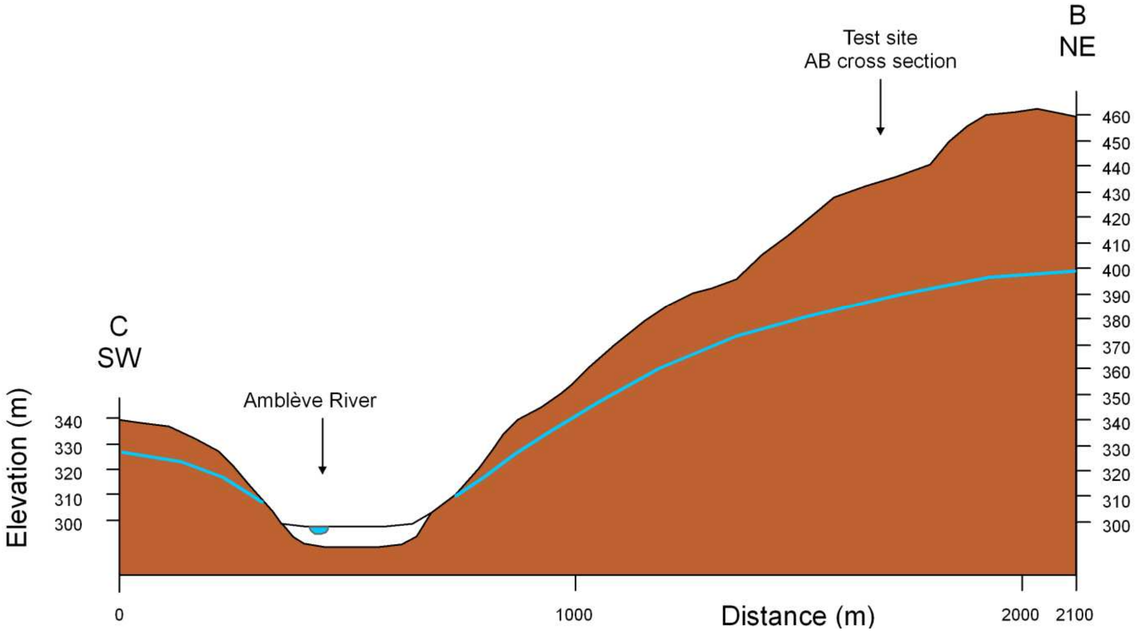

Figure 4.15: This CB cross section shows that the deeper aquifer is also constrained by the Amblève River in addition to the Warche River. See Figure 4.13 for the color legend.

Site/well	Locality	Province	X (m)	Y (m)	Z (m)	Z_{gw} (m)	ρ_{gw} (Ω.m)	K (m/s)
F3	Strée	Liège	218330	131083	245	220	14.0	$1.4E^{-4}$
F5	Evelette	Namur	206350	123725	244	233	16.4	$1.0E^{-5}$
F6	Tinlot	Liège	221473	128116	266	222	15.0	$2.5E^{-4}$
F7	Ochain	Liège	220411	125954	247	214	11.5	$4.0E^{-6}$
F10	Ossogne	Namur	210103	122403	255	226	22.1	$2.8E^{-5}$
F11	Havelange	Namur	213349	120168	255	246	18.0	$1.0E^{-4}$
F12	Bois-et-Borsu	Liège	218444	122476	263	234	14.3	$6.1E^{-6}$

Table 4.1: The geographical information for all new piezometers (one per studied site) is given here. Well coordinates are given in the Belgian Lambert 1972 coordinates system. Z_{gw} is the water table elevation measured in August 2009, ρ_{gw} is the groundwater electrical resistivity measured in the piezometers in August 2009 and, K is the hydraulic conductivity estimated with pumping tests in these wells.

	Carboniferous limestones	Late Famennian sandstones	Unit
pH	7.52	7.02	-
σ (at 25°C)	674	442	µS/cm
Total hardness	35	21	°fr
[Ca^{++}]	113	60	mg/l
[Mg^{++}]	16	14	mg/l
[Na^{+}]	14	12	mg/l
[K^{+}]	4	3	mg/l
[Cl^{-}]	32	23	mg/l
[SO4^{--}]	42	34	mg/l
[NO3^{-}]	33	27	mg/l
[CO3^{--}]	2	1	mg/l
[HCO3^{-}]	308	186	mg/l
[SiO2]	10	13	mg/l

Table 4.2: A typical groundwater composition of the two studied aquifers is given here. Values were rounded to the nearest unity for clarity. The discriminating parameters between both aquifers are the pH, the electrical conductivity and the total hardness. Obviously, the concentration in calcium and carbonates are also discriminating but they influence the total hardness value.

References

Boulvain, F., and Pingot, J.-L., 2012, *Une introduction à la géologie de la Wallonie* (in French), http://www2.ulg.ac.be/geolsed/geolwal/geolwal.htm, consulted January 20, 2012.

Brouyère, S., J. Gesels, P. Goderniaux, P. Jamin, T. Robert, L. Thomas, A. Dassargues, J. Bastien, F. Vanwittenberge, A. Rorive, F. Dossin, J.-L. Lacour, D. Le Madec, P. Nogarède, and V. Hallet, 2008, Caractérisation hydrogéologique et support à la mise en œuvre de la Directive Européenne 2000/60 sur les masses d'eau souterraine en Région Wallonne (Projet Synclin'EAU), *délivrable D.4.1 - Rapport relatif aux échantillonnages complémentaires des éléments majeurs*, Convention RW et SPGE-Aquapole (in French).

Brouyère, S., J. Gesels, P. Goderniaux, P. Jamin, T. Robert, L. Thomas, A. Dassargues, J. Bastien, F. Vanwittenberge, A. Rorive, F. Dossin, J.-L. Lacour, D. Le Madec, P. Nogarède, and V. Hallet, 2009a, Caractérisation hydrogéologique et support à la mise en œuvre de la Directive Européenne 2000/60 sur les masses d'eau souterraine en Région Wallonne (Projet Synclin'EAU), *délivrable D.3.12 - partie RWM021*, Convention RW et SPGE-Aquapole (in French).

Brouyère, S., J. Gesels, P. Goderniaux, P. Jamin, T. Robert, L. Thomas, A. Dassargues, J. Bastien, F. Vanwittenberge, A. Rorive, F. Dossin, J.-L. Lacour, D. Le Madec, P. Nogarède, and V. Hallet, 2009b, Caractérisation hydrogéologique et support à la mise en œuvre de la Directive Européenne 2000/60 sur les masses d'eau souterraine en Région Wallonne (Projet Synclin'EAU), *délivrable D.3.12 - partie RWM011*, Convention RW et SPGE-Aquapole (in French).

Brouyère, S., J. Gesels, P. Goderniaux, P. Jamin, T. Robert, L. Thomas, A. Dassargues, J. Bastien, F. Vanwittenberge, A. Rorive, F. Dossin, J.-L. Lacour, D. Le Madec, P. Nogarède, and V. Hallet, 2009c, Caractérisation hydrogéologique et support à la mise en œuvre de la Directive Européenne 2000/60 sur les masses d'eau souterraine en Région Wallonne (Projet Synclin'EAU), *délivrable D.3.12 - partie RWM012*, Convention RW et SPGE-Aquapole (in French).

Bultynck, P., F. Geukens, and A. Smolderen, 2001a, *Permian lithostratigraphic units, Malmédy Graben (Belgium)*, In Bultynck & Dejonghe, eds., Guide to a revised lithostratigraphic scale of Belgium, Geologica Belgica, 4 (1-2), 105-106.

Bultynck, P., and L. Dejonghe, 2001b, *Devonian lithostratigraphic units (Belgium)*, In Bultynck & Dejonghe, eds., Guide to a revised lithostratigraphic scale of Belgium, Geologica Belgica, 4 (1-2), 39-68.

Caterina, D., 2007, *Caractérisation hydrogéologique du bassin de la Haze*, Master thesis of the University of Liège, Liège, Belgium, 121 pp. (In French).

Delloye, F., Demarets, X., Imerzoukène, S., Masset, R., Meus, P., Popescu, C., Rentier, C., and Zaros, S., 2011, *Etat des nappes d'eau souterraine de la Wallonie*, Direction de l'Etat environnemental, Direction des eaux souterraines, http://environnement.wallonie.be/de/eso/atlas/, consulted January 20, 2012.

Geukens, F., 1986, *Commentaire à la carte géologique du Massif de Stavelot*, Aardkundige Mededelingen, 3, 15-30.

Geukens, F., 1999, *Révision de la carte géologique du Massif de Stavelot (1986)*, Aardkundige Mededelingen, 9, 183-190.

Gilson, M., P. Briers, I. Ruthy, and A. Dassargues, In preparation, *Carte hydrogéologique de Wallonie, Stavelot – Malmedy 50/5-6, 1:25000*, Namur, Service Public de Wallonie, Direction générale opérationnelle Agriculture, Ressources naturelles et Environnement.

Hallet, V., V. Peters, I. Ruthy, and R. C. Gogu, 2000, *Carte hydrogéologique de Modave - Clavier (prototype)*, LGIH, University of Liège, Belgium (In French).

Hayley, K., L. R. Bentley, M. Gharibi, and M. Nightingale, 2007, *Low temperature dependence of electrical resistivity: Implications for near surface geophysical monitoring*, Geophysical Research Letters, 34, L18402, doi:10.1029/2007GL031124.

Robert, T., 2007, *Etude et caractérisation hydrogéologique du bassin hydrogéologique du Rechterbach*, Master thesis of the University of Liège, Liège, Belgium, 101 pp. (In French).

Robert, T., A. Dassargues, S. Brouyère, O. Kaufmann, V. Hallet, and F. Nguyen, 2011, *Assessing the contribution of electrical resistivity tomography (ERT) and self-potential (SP) methods for a water well drilling program in fractured/karstified limestones*, Journal of Applied Geophysics, 75 (1), 42-53.

Robert, T., A. Dassargues, S. Brouyère, O. Kaufmann, V. Hallet, and F. Nguyen, In preparation, *Electrical properties of the Dinant Synclinorium calcareous formations*.

Ssolbergj, 2008, *Wallonia in Belgium and the European Union*, downloaded October 27, 2011, http://en.wikipedia.org/wiki/File:Wallonia_in_Belgium_and_the_European_Union.svg, Wikipedia.

Poty, E., L. Hance, A. Lees, and M. Hennebert, 2001, *Dinantian lithostratigraphic units (Belgium)*, In Bultynck & Dejonghe, eds., Guide to a revised lithostratigraphic scale of Belgium, Geologica Belgica, 4 (1-2), 69-93.

Vandenven, G., 1990, *Explications de la carte du Synclinorium de l'Eifel (Région de Gouvy – Sankt-Vith – Elsenborn)*, Annales de la société géologique de Belgique, 113, 103-113.

Verniers, J., A. Herbosch, M. Vanguestaine, F. Geukens, B. Delcambre, J.-L. Pingot, I. Belanger, M. Hennebert, T. Debacker, M. Sintuin, and W. De Vos, 2001, *Cambrian-Ordovician-Silurian lithostratigraphic units (Belgium)*, Geologica Belgica, 4 (1-2), 5-38.

5. Identification of fractures and well positioning

5.1. Geoelectrical signatures of a preferential flow path in fractures

5.1.1. Introduction

One goal of this work was to highlight a characteristic signature – in terms of electrical resistivity and SP signals – of preferential flow paths in fractured media. We saw in sections 2 (ERT) and 3 (SP) that both active and passive electrical methods can be helpful to characterize more fractured area. To further illustrate the ability of retrieving fractures positions from SP signals, we show in this section the results of a shallow geoelectrical survey conducted in a test site situated in eastern Belgium in the Stavelot Massif (Robert, 2007). Compared to the other studied sites, we here investigate a depth of a few meters versus tens of meters in the following sections (5.3, 5.4, 6, and 7). The physical, geological, hydrogeological, and geochemical backgrounds of the Stavelot Massif are presented in section 4.5.

The aquifer that we investigated lies in the weathered part of the bedrock composed of Cambrian quartzites. The water table is shallow, between 2 and 3 m deep depending the season. Piezometrical measurements in a well situated in the village confirmed that the water table elevation is directly in relation with rainfall events.

The test site comprises a small spring that supplies drinking water to a small part of the inhabitants of a nearby village (Figure 5.1). The flow rate of this spring is difficult to measure since it is exploited. However, it is quite low, probably less than a few hundreds L/h.

We assumed that a fractured zone in the weathered quartzites drains groundwater directly toward the spring. Therefore, we performed the ERT and the SP profiles perpendicular to the regional direction of flow (Figure 5.1), centered on the spring position, and positioned 20 m upstream from the spring location. The targeted fractured zone is only a few meters deep.

We measured the specific electrical conductivity of groundwater in 2007 and 2008 at about 70 µS/cm. This extremely low value is characteristic of such shallow aquifers in the Stavelot Massif. As a consequence, in terms of bulk electrical resistivity, a fractured area may not present a contrast compared to more compact bedrock. If less resistive anomalies are present, they could be a consequence of the presence of clayey materials but not a proof of water-bearing fractures.

In terms of SP signals, rocks containing less conductive groundwater present higher coupling coefficients than rocks containing more conductive groundwater (see section 3). Groundwater is also acidic in the studied site (pH = 5.9) and the coupling coefficient has a negative sign (see section 3). Therefore, we can expect a negative anomaly in the SP profile centered on the spring projected position.

5.1.2. Methods

We used two different electrode arrays to acquire ERT data, a Wenner alpha and a dipole-dipole (with a spacing factor $n \leq 6$) configuration. We used the Wenner alpha array for its high signal-to-noise ratio and the dipole-dipole array for its good lateral resolution (see section 2.2). We inverted both data sets together to obtain an electrical image of the subsurface. We stopped the inversion process at a final absolute error of 3%. To acquire the data, we used the commercial ABEM Terrameter Lund Imaging System (one recording channel) with 64 electrodes spaced by 1 m. To invert the data, we used the Res2DInv software (Loke and Barker, 1996) using an extended model and a robust data and model constraint (see section 2.4). This robust model constraint also called the blocky inversion (e.g., Loke et al., 2003) produces sharper electrical structures. Since fractured zones are assumed to present sharp limits in the subsurface, we believe that the blocky inversion is particularly well suited.

We took SP measurements every meter at the same location as the ERT electrodes. To evaluate the SP error, we measured SP signals in 5 holes situated inside a 0.3 m square (Figure 5.2). The mean value of these 5 measurements represents then the average SP signal of the SP station while the associated SP error is given by the corresponding standard deviation value. The distribution of the SP errors (Figure 5.3) shows that any SP anomaly higher than 4.2 mV is statistically significant and can be physically interpreted.

5.1.3. Results

The bulk electrical resistivity distribution in the test site can be separated horizontally in two different parts (Figure 5.4). The first 2 m correspond to the unsaturated zone of the weathered bedrock. They present more electrically resistive structures with values ranging from 520 to 1000 Ω.m. Then, below the water table, the bulk electrical resistivity decreases with values ranging between 150 to 460 Ω.m. The depth of investigation was estimated at 6 to 8 m using the relative sensitivity matrix.

No specific electrical resistivity contrast can be highlighted in this electrical image. One reason could be that groundwater is not electrically conductive but rather resistive since its specific electrical conductivity is about 70 µS/cm. Therefore, the contrast of electrical resistivity is not large enough to be imaged.

SP signals present a clear and strong negative anomaly, 15 meters wide, in the middle of the profile (Figure 5.4). 15 mV (in absolute value) is much more than the maximum value of the SP error distribution which is 4.2 mV (Figure 5.3) and we can therefore conclude that this anomaly is statistically valid. Since no other contribution to the SP signal than the electrokinetic effect is expected and since there is no electrical resistivity contrast in the electrical image, we can interpret this anomaly in terms of groundwater flow. The interesting point is that the center of this anomaly is exactly situated at the spring projected location where we assumed a preferential groundwater flow path in fractures. Therefore, we can assume that the fractured area allows groundwater to flow rapidly toward the spring and that this fluxes difference between the fractured area and the host rocks creates a negative anomaly in the SP signals.

5.1.4. Conclusions

Here, we demonstrated that ERT can sometimes fails for the identification of fractures locations, especially in areas with electrically resistive groundwater. However, even if the contrast in bulk electrical resistivity was here not sufficient, we recommend performing ERT whenever SP measurements are taken since SP signals are also linked to contrasts of electrical resistivity (section 3.1).

The data from this site demonstrated the ability of the SP method to delineate a fractured area where groundwater preferentially flows. We found a 15 mV negative anomaly in the SP signal exactly at the spring (projected) position. This anomaly can directly be correlated with the SP anomaly of type V in Richards et al. (2010, Figure 11).

This work opened great perspectives since a more general use of geoelectrical surveys, especially the joint use of ERT and SP, before a drilling campaign (e.g., for drinking water wells) could precise the more hydraulically active areas. Section 5.3 presents an assessment of the joint use of ERT and SP in a larger water well drilling campaign in limestones of the Dinant Synclinorium in southern Belgium, where the target is more challenging given that it is located at tens of meters deep.

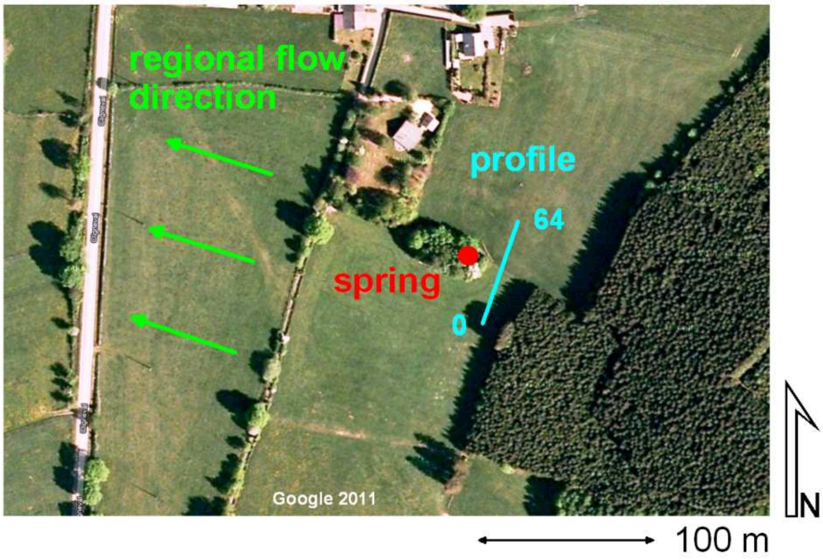

Figure 5.1: To identify a geoelectrical signature of preferential flow paths in fractures, we conducted a geoelectrical survey in a site where fractures drain groundwater toward a spring. We centered the geophysical profile (ERT and SP) on the projected spring position, 20 m upstream, and perpendicular to the regional groundwater flow direction.

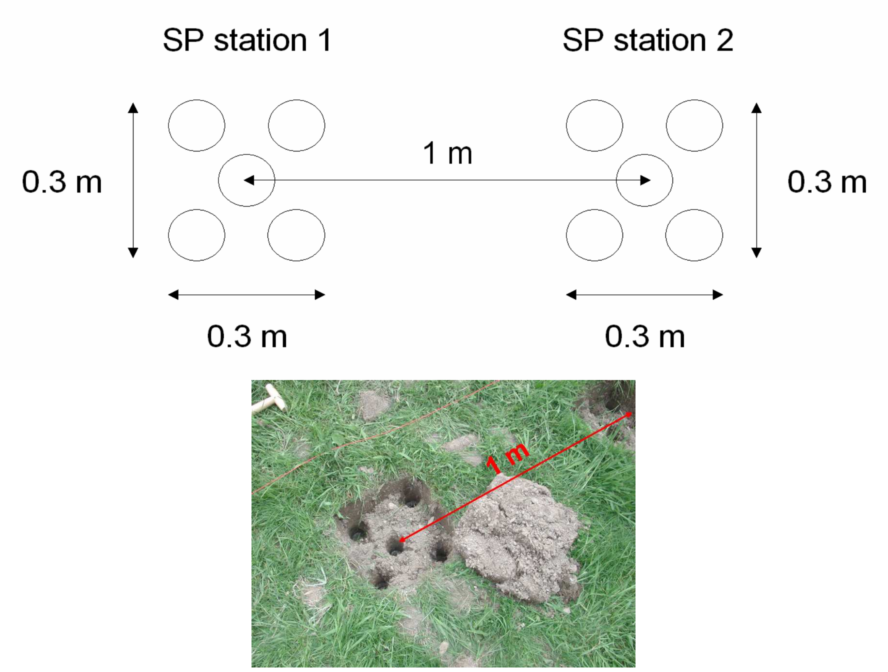

Figure 5.2: To evaluate the SP error associated with a particular SP station, we measured the SP signal in 5 holes inside a 0.3 m square. The mean value of these 5 measurements represents the average SP signal of the SP station while the associated SP error is given by the standard deviation value. Every SP station is separated by 1 m.

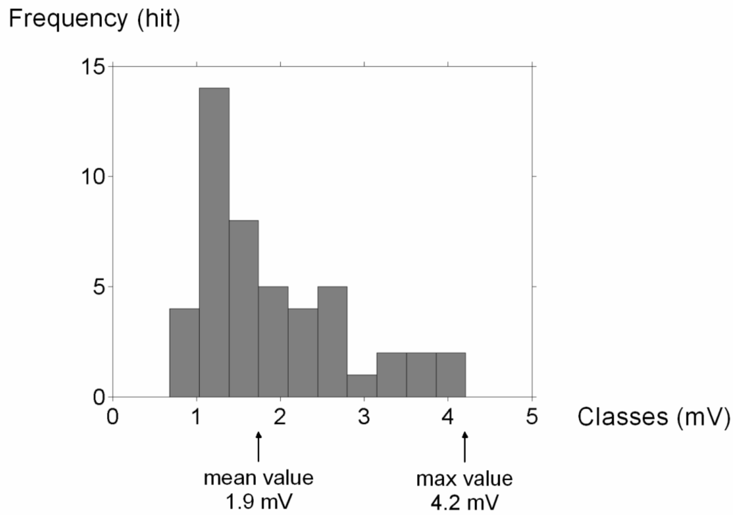

Figure 5.3: Any SP anomaly that has an absolute value higher than 4.2 mV (maximum value of the SP errors distribution) is statistically significant and can therefore be physically interpreted.

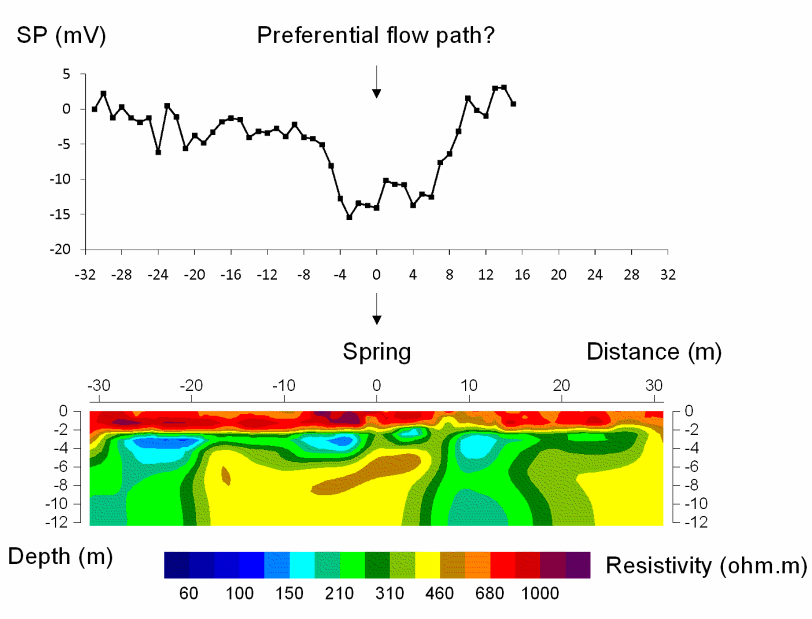

Figure 5.4: Using only one geophysical method could be risky to delineate a preferential groundwater flow path (here, a fractured area in quartzites). Indeed, with an ERT profile centered on the spring position (bottom), we were not able to highlight the fractured zone, probably because the electrical contrast between fractured and compact quartzites was not large enough. However, we highlighted an SP anomaly centered at the spring position (top) by measuring the natural electrical (self) potential every meter at the ground surface. We assumed that this anomaly is only related to preferential groundwater flow in the fractured area since we assumed that the electrokinetic effect is the dominant contribution of the self-potential signal in our test site.

References

Loke, M. H., and R. D. Barker, 1996, *Rapid least-squares inversion of apparent resistivity pseudosections by a quasi-Newton method*, Geophysical Prospecting, 44 (1), 131-152.

Loke, M. H., I. Acworth, and T. Dahlin, 2003, *A comparison of smooth and blocky inversion methods in 2D electrical imaging surveys*, Exploration Geophysics, 34 (3), 182-187.

Richards, K., A. Revil, A. Jardani, F. Henderson, M. Batzle, and A. Haas, 2010, *Pattern of shallow ground water flow at Mount Princeton Hot Springs, Colorado, using geoelectrical methods*, Journal of Volcanology and Geothermal Research, 198 (1-2), 217-232.

Robert, T., 2007, *Etude et caractérisation hydrogéologique du bassin hydrogéologique du Rechterbach*, Master thesis of the University of Liège, Liège, Belgium, 101 pp. (In French).

5.2. Outcrops analysis

Geological outcrops are direct windows of the subsurface. Therefore, their analysis is mandatory when this information is present. In this section, we will briefly describe several outcrops (Pictures 1 to 6) from the Mercier quarry situated in the village of Petit-Avin in terms of “fractures” and karstic phenomena. We will also present a picture of a quarry exploiting late Famennian sandstones and situated in the same village as the Mercier quarry (Picture 7).

The Mercier quarry (Figure 5.5 and Figure 5.6) lies in the extension of the Havelange calcareous syncline where we performed numerous field works (site F11). The Mercier quarry has a depth of about 40 m (Figure 5.5). The first meters are composed of overburden, mainly clay loam (Picture 2). Overburden overlies the limestone bedrock that can be highly weathered (Picture 2), fractured (Pictures 3 to 5), and even karstified (Picture 6). The water table can be retrieved at the bottom of the quarry that is about at the same elevation as the Hoyoux River that flows nearby in the north.

Different types of fractures can be found in these calcareous synclines. First, the stratification is a well-known fractures family. Since the Mercier quarry is situated in the southern flank of the calcareous valley (Figure 5.5), the dip is toward north. The stratification plane (S_0) has a direction and a dip of about N70°E/70°N and is presented in Pictures 1 to 3.

Second, the classical fractures or joint sets (J_1 and J_2) can be viewed in Picture 4 (taken perpendicular to S_0). J1 has a direction and a dip of about N5°E/35°E whereas it is N130°E/60°S for J2. Both joint types have a millimetrical to centimetrical thickness except in places where erosion and dissolution occurred preferentially (Picture 5). In some areas, these fractures can have up to a decimetrical thickness.

When erosion or dissolution becomes too important, we cannot employ the term fracture anymore since it is more related to karstic phenomena. Therefore, the third type of fracture presented here is related to karstic conduits (Picture 6) that can have decimetrical to metrical opening. Hereafter in this work, we will not distinguish the different types of fractures since they all lead to the same result in terms of groundwater flow, that is a preferential path.

The sandstone quarry is situated on the ridge of the anticline adjacent to the Havelange calcareous syncline. The bottom of the quarry is at the same elevation as the Hoyoux River that flows nearby. The water table can be seen in equilibrium with the water level in the

Hoyoux River (Picture 7). The stratification plane (S_0) has a direction of N70°E and the dip is subhorizontal. These sandstones are also highly fractured as evidenced by Picture 7.

We would like to thank Daoudi et al. (2008) and more specifically Cédric De Marneffe and Simon Delvoie for making the pictures available to this work.

Reference

Daoudi, M., C. De Marneffe, I. Dia, G. Dumont, E. S. Sauret, and Q. Thiebaut, 2008, *Havelange Project – Non invasive investigations on the future water exploitation field of Havelange*, Project in the framework of the Applied Geophysics course of Prof. F. Nguyen, University of Liege, 51 pp.

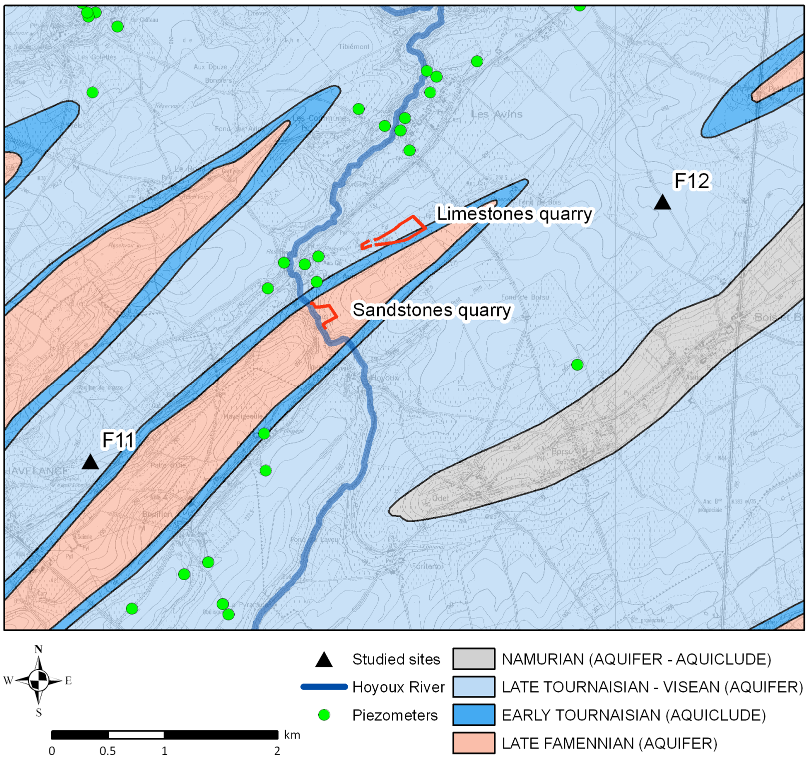

Figure 5.5: This map presents the locations of two quarries – one of sandstones and one of limestones – nearby the Havelange calcareous syncline that was intensively studied during this work.

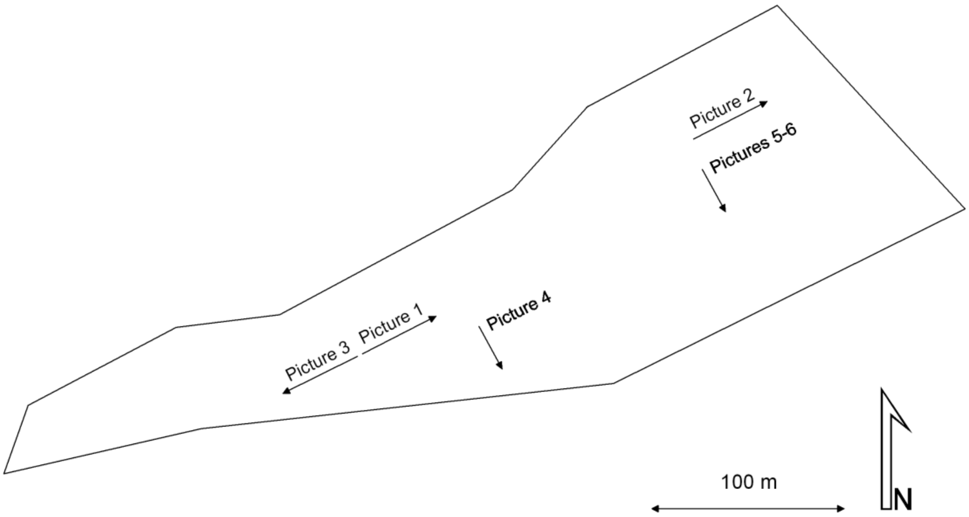

Figure 5.6: This sketch of the Mercier limestone quarry presents the orientation of several pictures that are presented below. Note that the general direction of the calcareous synclines (about N70°E) corresponds to the orientation that was taken for pictures 1 to 3.

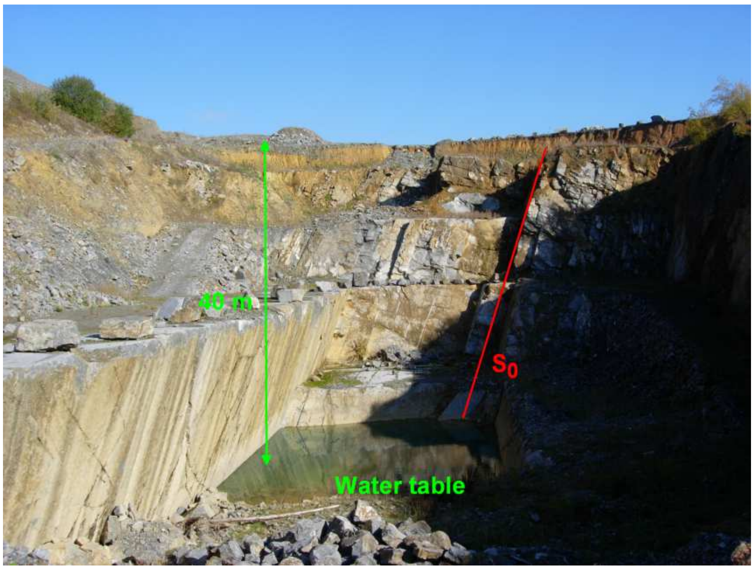

Picture 1: NE view of the Mercier quarry situated in the village of Petit-Avin. The water table is situated at a depth of about 40 m from the top of the quarry, where we can see the overburden and the weathered part of the calcareous bedrock (for a zoom, see Picture 2). The stratification plane (S_0) has a direction and a dip of N70°E/70°N.

Picture 2: Top of the Mercier quarry (NE view). The overburden has generally a thickness between 2 and 3 m but, in some areas, it penetrates deeper in more weathered limestones (up to 6 m deep in this picture). Therefore, in our electrical images, we have to expect a first layer of more conductive materials (clay loam) that is not homogeneous in terms of thickness. Karstification is also present with anomalies A and B.

Picture 3: SW view of the Mercier quarry. The limit between a more fractured area (right) and compact limestones (left) is sharp and subvertical (70°N). This information is crucial when choosing an appropriate regularization technique for ERT (see section 2.4.3).

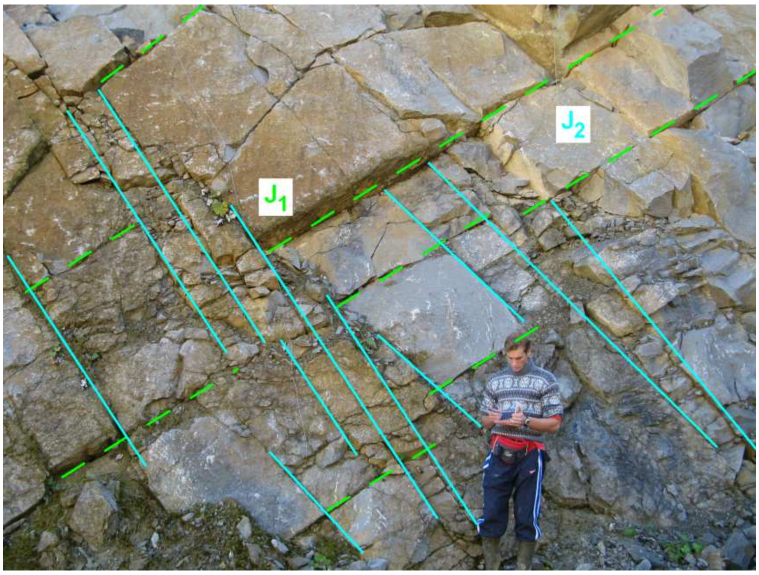

Picture 4: SE view (perpendicular to S_0) of the Mercier quarry. Two major joints families are present on this picture. J_1 has a direction and a dip of about N5°E/35°E whereas it is N130°E/60°S for J_2. Both joint types have a millimetrical to decimetrical thickness (see Picture 5).

Picture 5: Another SE view (perpendicular to S_0) of the Mercier quarry. Fractures can have centimetrical to decimetrical thicknesses, such as for the J_2 type that is presented on this picture. These factures were eroded and dissolved and they lead now to preferential groundwater flow paths.

Picture 6: SE view (perpendicular to S_0) of the bottom of the Mercier quarry. Two major karstic conduits are presented here. Their thicknesses can be decimetrical to metrical and therefore, such karstic conduits are major preferential paths for groundwater flow.

Picture 7: NE view of the sandstone quarry that is situated along the Hoyoux River in the village of Petit-Avin. This late Famennian sandstone anticline is adjacent to the Havelange calcareous syncline in the south. The water table is in equilibrium with the water level in the Hoyoux River that flows nearby. We can see on this picture that the stratification plane is nearly horizontal since the quarry lies at the top of the sandstone crest.

5.3. Joint interpretation of ERT and SP data for well positioning

We saw in section 5.1 that SP signals present negative anomalies near preferential flow paths in fractures, and that SP surveys can therefore help to position new water wells. However, the ERT survey presented in section 5.1 did not present contrasts of electrical resistivity highlighting this more fractured area, but the local groundwater electrical conductivity was quite low.

In section 5.2, we presented our targets for this section, large fractured zones in the limestone bedrock where we wanted to drill new monitoring wells. Given the prior information about the geochemistry of the calcareous synclines we investigated (see section 4.4), we were confident that water-bearing fractured zones would present a strong contrast of electrical resistivity. We were also confident that hydraulically-active fractured zones would moreover present a negative SP anomaly. We therefore used both methods to delineate suitable positions to drill new monitoring wells in zones with little hydrogeological data. Once the wells drilled, we were able to use ground truth information to assess the contribution of the joint use of ERT and SP in a drilling program.

The results of this study are presented in Robert et al. (2011), a scientific paper published in Journal of Applied Geophysics, 75 (1), 42-53. An earlier version of this section was also presented at Near Surface 2009, in Dublin, Ireland.

5.4. Comparison of different model constraints in DC electrical data inversion for the characterization of fractured aquifers

Incorporating a priori information in an inverted model is not an easy task since it depends on the type of a priori information in our possession but also on the model constraint that we can use to bias the inverted model in a way that the inverted model satisfies the a priori information too (see section 2.4.3). When dealing with fractured areas in limestones, one can expect sharp transitions between electrical structures representing fractured zones or host rocks (see section 5.2).

The type of a priori information we possess here comes from outcrops which present sharp and nearly vertical limits between fractured areas and more compact limestone zones (see section 5.2). On this basis, we chose to incorporate this information by selecting appropriate model constraints described below.

In this section, we present a comparison of different inverted models obtained with three model constraints, namely the smoothness-constraint (L_2 norm) as the standard reference, the blocky or robust constraint (L_1 norm), and the minimum-gradient-support (MGS) approach in order to find which approach best images sharp electrical structures. See section 2.4.3 for a description of the different model constraints. We used a numerical benchmark model based on a real ERT image and we processed real data taken in the Havelange valley (see chapter 7).

We used two different inversion codes, an academic one, CRTomo (Kemna, 2000), and a commercial one, Res2DInv (Loke and Barker, 1996), to perform this comparison. If both codes allow the smoothness-constraint inversion, the MGS approach (Blaschek et al., 2008; Portniaguine and Zhdanov, 1999) is only implemented in CRTomo whereas the blocky inversion (Loke et al., 2003) is only present in Res2DInv up to now.

Since we developed a synthetic case study, we used it to compare three different quantitative resolution indicators, namely the DOI index, the diagonal of the resolution matrix, and the cumulative sensitivity matrix in order to best appraise the quality of the inverted model but also to deal with the depth of investigation of an electrical image.

5.4.1. The synthetic case study

We build a synthetic model with sharp lateral contrasts of electrical resistivity between different rock formations that are more or less fractured. We based the construction of this synthetic model on a real case study (see section 5.3 and Robert et al., 2011 – site F5 – Figure 6). In calcareous formations such as the ones studied in this work, we often have a more conductive superficial layer representing the overburden (clay loam) and the weathered bedrock. At depth, lateral contrasts due to fracturing or karstification often occur.

The first layer of the model (Figure 5.7) is composed of a 10 m thick superficial conductive body (80 Ω.m) representing the overburden. The second layer represents weathered rocks (200 Ω.m) more or less thick (from 5 to 15 meters). Then, we inserted a conductive body (200 Ω.m) related to a more fractured area between two resistive bodies (1000 and 3000 Ω.m) representing the host rocks. The width of this fractured zone is equal to 100 m. At last, we inserted a square body (80 Ω.m) inside the fractured area to represent a karstified area. It is assumed that the water table is 10 m deep so that the different zones of the model are fully saturated. This synthetic model is a simplified view of the inverted model we can see at the bottom of Figure 6 in Robert et al. (2011), shown in this thesis at section 5.3.

To construct this model, we used a finite element mesh composed of 5 x 5 m cells where 5 m is the unit electrode spacing, a no-flow boundary condition at the surface and mixed boundary conditions at the sides and bottom of the model. The model has 20 layers which correspond to a total depth of 100 m. We simulated an acquisition sequence based on a dipole-dipole configuration with 64 electrodes spaced by 5 m and a spacing factor $n < 6$ to calculate our data through forward modeling. This resulted in a data set containing 1015 measurements. This sequence was used successfully in our field acquisitions and we believe it represents a good compromise between the signal-to-noise ratio (for field studies) and resolution (see section 2.2).

We added 3% of Gaussian noise in the data set before inversion (Figure 5.8) since real data are always contaminated with noise. However, it is difficult to estimate the true data noise level that affects real data and one generally uses the reciprocal error distribution to estimate the true data errors. To be as close as possible to real data conditions, we used the Slater et al. (2000) approach (Figure 5.9) to calculate an error model (see section 2.3) based on the 3% of Gaussian noise we added. With this approach, we obtained an error model with $a = 0.1$ mΩ (absolute error parameter) and b = 3% (relative error parameter) that we used in every inversion presented in this section. The standard deviation value of the error distribution is about 1%. Therefore, we chose to present resulting images with a final ε^{RMS} error of 1; see section 2.4.2 and Eq. (2.14).

In order to stand as much as possible close to field data, we always used a robust (L_1 norm) constraint to calculate the data misfit (see section 2.4.2 and Eq. 2.14). We chose to present every CRTomo inversion with a final ε^{RMS} error of 1 and we tried to obtain the same percentage with Res2DInv. However, in order to approach this level with Res2DInv, we had to trim the data set with a cutoff value of 10%. As a consequence, the final data set had to be reduced (mostly measurements close to the surface) to 896 data points instead of 1015. With the remaining 896 measurements, we obtained a RMS value of 1.44%.

As a prior and reference model for all inversions, we used a homogeneous half-space with a value of 200 Ω.m, that is approximately the mean value of the measured apparent resistivity distribution. We tried to estimate the depth of investigation of the inverted model (see section 2.4.4) using the approach from Oldenburg and Li (1999). To do this, we ran two smoothness-constraint inversions with two different values – 20 and 2000 Ω.m – for the prior and homogeneous reference models and we compared both resulting models (Figure 5.10). Then, we calculated the DOI index. We extended the regular mesh to a depth of 300 m in order to visualize the differences in the electrical structures linked to the choice of the reference model.

With the approach from Oldenburg and Li (1999), it is easy to discriminate parts of the inverted model that are not related to surface measurements at all (Figure 5.10). Here, we can easily affirm that the mesh should have a maximal depth of 100 m since both inverted models return to the value of the reference model below this depth. We can also see that the central conductive area which represents a fractured zone – between 100 and 200 m – is either closed or opened at a depth of about 50 m, depending on the choice of the reference model. This simple comparison gives a direct indication about the depth of investigation.

To precise this depth of investigation or simply appraise the quality of our inverted models, we decided to use the cumulative sensitivity matrix (see section 2.4.4) which has the same behavior as the resolution matrix (Figure 5.11 and Figure 5.12) but requires less computation time. Basically, the cumulative sensitivity matrix gives directly an idea about the sensitivity of measurements subject to changes in the electrical structures. Therefore, areas with poor sensitivity are generally considered as less reliable. Indeed, if a change occurs in those areas, this will barely modify the surface data.

We compared the three resolution indicators, namely the DOI index, the cumulative sensitivity matrix, and the diagonal values of the resolution matrix versus the true error – the error between the true and the inverted models – in order to select the best cutoff to appraise an electrical image (Figure 5.12). Full details of this study will be available in a forthcoming paper from Caterina et al. (in preparation for the Near Surface Geophysics Special Issue on Geotechnical Assessment and Geoenvironmental Engineering of June 2013). However, we present hereafter some insights of the methodology which can be summarized as follows:

1. Forward modeling of the true resistivity model given an acquisition sequence,
2. Noise is added to the synthetic data set,
3. Inverse modeling of the synthetic data set contaminated with noise,
4. The subtraction of the inverted model to the true model gives the true error model,
5. The true error model is compared to the resolution indicator to select the appropriate cutoff.

Oldenburg and Li (1999) suggested an arbitrary cutoff value of 0.1 – 0.2 for their DOI index that is empirically supported by several authors (e.g., Hilbich et al., 2009; Marescot et al., 2003). However, selecting a cutoff value of 0.1 in our synthetic case leads to strong errors since cells related to high absolute errors are kept with this resolution indicator (Figure 5.12). This is not the case with both the sensitivity and the resolution matrix that behave the same. With these resolution indicators, we can find a cutoff value that rejects every cell related to a high absolute error. In the present case, $10^{-1.5}$ for the resolution matrix and $10^{-2.8}$ for the cumulative sensitivity matrix should be reasonable values. Note that these values are strongly dependent on the resistivity distribution, for example Nguyen et al. (2009) used a value for the cumulative sensitivity distribution of 10^{-5} in the context of seawater intrusions which generally exhibit smooth variations between low resistivity zones. These cutoff values, when reported in Figure 5.11, indicate the depth of investigation of the inverted model which is about 35 m in the central part of the electrical image.

Compared to the true resistivity model (Figure 5.13), the two smoothness-constraint inversions do not recreate the true electrical structures whereas the blocky inversion and the inversion using the MGS approach using a value of 0.05 for β (see Eq. 2.18) do. Sharper electrical structures are indeed retrieved with focused inversion schemes as demonstrated by other authors (e.g., Portniaguine and Zhdanov, 1999; Blaschek et al., 2008). Interestingly here, with the blocky model, it is also possible to discriminate the karstified area from the fractured zone which is not possible with others model constraints. Clearly, the regularization of the MGS approach, which forces minimum gradients in the inverted model, overtakes data resolution at the benefits of an oversimplified structure but at the expenses of the sought structure in this case.

Generally, studies focus on the recovered resistivity distribution. In several contexts, including the one of this thesis, it might be relevant to look at the structures recovered by ERT (see also Nguyen et al., 2005). We will therefore examine the impact of the different regularizations in terms of resistivity gradients (Figure 5.14). The best inversion procedures seem to be the blocky inversion and then, the MGS approach (still with β = 0.05) since the maximum resistivity gradients correspond well in value and position with the true resistivity gradients. The two smoothness-constraint inversions (with Res2Dinv and CRTomo) do not recreate so well the different electrical structures, as expected, and should therefore not be used when prior information indicates the existence of sharp limits.

Note that the difference observed between the two smoothness-constraint inversions result from the different optimizations of the regularization parameters (lambda). CRTomo takes the solution with the maximum lambda for a given $\varepsilon^{\mathrm{RMS}}$ (section 2.4.1), which is important to actually fulfill the optimization criterion (smoothest model, subject to fitting the data). In this sense, Res2DInv does not take the Occam solution since the iteration process stops once the desired RMS error is achieved (lambda is therefore not optimized). As a consequence, CRTomo will generally produce smoother images than Res2DInv.

5.4.2. The real case study

The real case study corresponds to a long ERT profile (595 m) that we acquired to identify and characterize large hydraulically-active fractured zones in the Havelange calcareous syncline (see section 7.1). We positioned the profile perpendicular to the direction of the geological structures and we tried to cover the whole calcareous syncline.

We used 120 electrodes spaced by 5 m with a dipole-dipole configuration ($n \leq 6$) to acquire this data set. We also had to acquire it in a roll-along mode since we only had access to 72 electrodes (3 cables with 24 electrodes each). The acquisition was then as follows. First, we collected the data of a 72 electrodes profile. Then, we moved the first 24 electrodes (one cable) at the end of the profile and we acquired the extra data set. We repeated the last operation once more to complete the data collection.

We used an IRIS SYSCAL PRO device to collect these data. We optimized the dipole-dipole sequence for multi-channel acquisition by sorting the sequence in a way that no pair of potential electrodes was used after a current injection. We used up to 6 channels because we limited the spacing factor n to 6 in order to avoid too high geometrical factors to improve the signal-to-noise ratio. We chose a transmitter-current-injection time window (T_{on}) of 1 s and we performed 3 to 6 stacks with a quality factor (the standard deviation value of the stacked signal) of 1%.

Due to some logistical constraints, we were not able to collect all the reciprocal measurements since we had to remove the profile to allow the farmer to plow its field. As a consequence, we were only able to collect normal measurements for the last roll-along sequence.

The distribution of the reciprocal error (Figure 5.15) is normal and centered on zero. The standard deviation value (σ) is equal to 0.25 mΩ. Therefore, ±96% of the reciprocal errors are comprised between -0.5 and 0.5 mΩ, that is $\pm 2\sigma$. Since we did not possess all reciprocal errors, we constructed an error model based on the approach of Slater et al. (2000). The resulting error model parameters are equal to 0.75 mΩ (absolute error parameter – a) and 0.5% (relative error parameter – b) and the error model is presented in Figure 5.16.

We took the topography into account for the mesh construction since the maximum difference in elevation in the profile is about 35 m (Figure 5.17). The main mesh is composed of 119 x 30 finite elements of 5 x 5 m whereas it is extended – in CRTomo – in both sides of the model by 5 x 30 elements with increasing width to account for the boundary conditions (see the synthetic case study).

Here, we also used a robust (L_1 norm) constraint to calculate the data misfit (see section 2.4.2). We present every CRTomo inversion with a final $\varepsilon^{\mathrm{RMS}}$ error of 1 for a maximum value of λ and again, we tried to obtain the same corresponding RMS with Res2DInv. Generally, we obtained a RMS value between 1.84 and 2.44% with Res2DInv. As a prior and reference model for all inversions, we used a homogeneous half-space with a value of 200 Ω.m, that is approximately the mean value of the measured apparent resistivity distribution.

Given our findings related to the calculation of the depth of investigation on the synthetic case study, we decided to only use the cumulative sensitivity matrix. The choice of the resolution-indicator cutoff is more difficult in a real case study since we cannot use the true resistivity model to calculate the true error. To solve this problem, we used the following methodology:

1. The model obtained by inverse modeling of the real data set is considered as “true”,
2. Forward modeling of the “true” model with the same acquisition sequence as used in reality,
3. Inverse modeling of the resulting data set with the same inversion parameters,
4. The subtraction of the inverted model to the “true” model gives the “true” error model,
5. The “true” error model is compared to the cumulative sensitivity matrix to select the appropriate cutoff.

This methodology will be part of a forthcoming paper from Caterina et al. (in preparation for the Near Surface Geophysics Special Issue on Geotechnical Assessment and Geoenvironmental Engineering of June 2013).

Now that we have access to an estimated ”true” error, we can use it to pick a cutoff value of the sensitivity distribution for depth of investigation purpose. We plotted this error versus the cumulative sensitivity matrix in Figure 5.18. We can see that above a sensitivity value of 10^{-2}, the absolute errors (in Ω.m) remain at a low level (below 100 Ω.m). However, with sensitivity values below 10^{-2}, the absolute errors start to increase exponentially. Therefore, it seems wise to only physically interpret the electrical structures that present a sensitivity value above 10^{-2}. Note that we used the absolute error and not the relative one. Since we focus on high resistivity contrasts, we believed that taking the absolute error was a better choice.

Reporting the selected cutoff value (10^{-2}) in Figure 5.19 allows the estimation of the depth of investigation. For example, in areas that are more electrically conductive, the depth of investigation is about 30 m below surface which approximately corresponds to an elevation of 230 m. As a consequence, these more conductive electrical structures can be interpreted geologically. In this case, they are most likely related to fractured zones in the limestone valley.

The four inverted models presented in Figure 5.20 present all three more conductive areas in depth, most likely fractured areas in the limestone valley. The overburden which is composed of clay loam is also electrically conductive. This upper layer is well imaged with the smoothness-constraint and the blocky inversions whereas it is almost completely absent (less thick) in the inversion using the MGS approach. This fact is clearly visualized in Figure 5.21 presenting the gradient images. Indeed, we can see that the MGS approach (in contrary of the other approaches) places the first horizontal gradient directly at the surface, which is not coherent because drillings logs show at least a 5 m thick conductive overburden (section 5.3). However, we did not scan the whole range of β values here, and it is therefore possible to find a solution with the MGS approach that has the same characteristics as the other inverted models.

All inverted models seem to position the different lateral gradients in the same locations, but the MGS approach (at least, with the chosen β value) seem to be less efficient for horizontal gradients. Scanning the whole ranges of β values will probably solve this issue. In terms of well positioning, we recommend to use one of the two focused inversion schemes presented here, the blocky inversion or the MGS approach. With the MGS approach, one needs to be aware that a full scan of β values may be the best approach, even if it costs time.

Choosing an appropriate model constraint is not an easy task since it will generally biases the inverted model. In the case of sharp and nearly vertical fractured areas in limestones, we saw that – both in a synthetic and in a real case study – the blocky inversion and then, an inversion using the MGS approach led to sharper and simpler electrical structures. In terms of electrical resistivity gradients, we also saw that these two focused approaches position correctly the different structures. The gradients values seem to be slightly underestimated with the MGS approach and this scheme also produces raw images that are maybe not so physically realistic as the blocky structures. Here, we generally used the blocky inversion to present our ERT images.

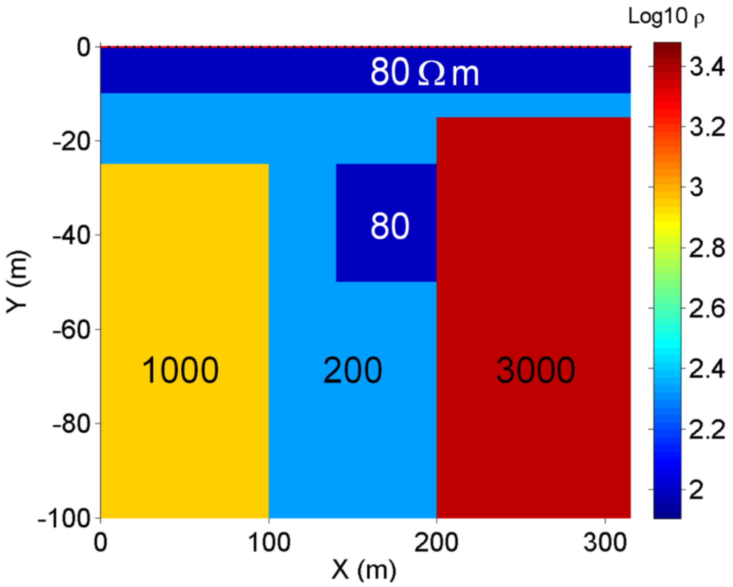

Figure 5.7: We build a synthetic model representing sharp lateral contrasts of electrical resistivity between different rock formations that are more or less fractured. The first layer represents the conductive overburden (clay loam – 10 m thick – 80 Ω.m) and its bottom corresponds to the water table depth whereas the second layer (200 Ω.m) is related to weathered limestones (5 to 15 m thick). A fractured area (200 Ω.m) of 100 m width lies between two resistive bodies (1000 and 3000 Ω.m) representing compact limestones. Finally, we inserted a karstified area (80 Ω.m) inside the fractured zone. This synthetic model is based on a real case study (Robert et al., 2011 – site F5 – Figure 6; section 5.3).

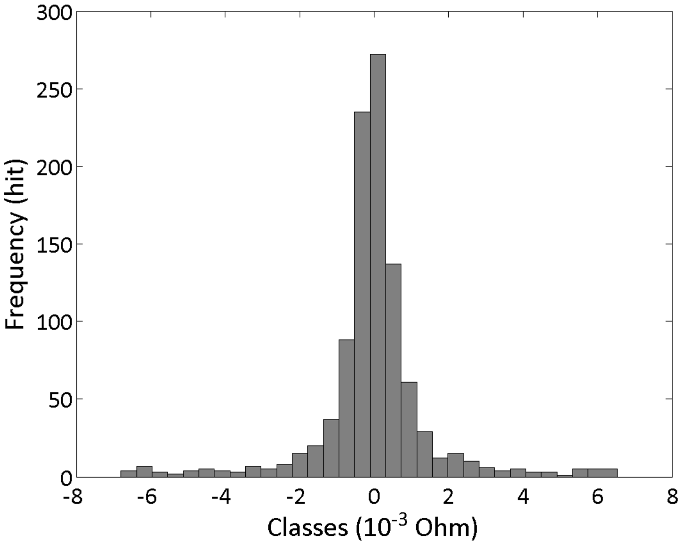

Figure 5.8: After the forward modeling, we added 3% of Gaussian noise in the data to simulate real data. This histogram (in mΩ) presents the corresponding data noise distribution which is centered on zero.

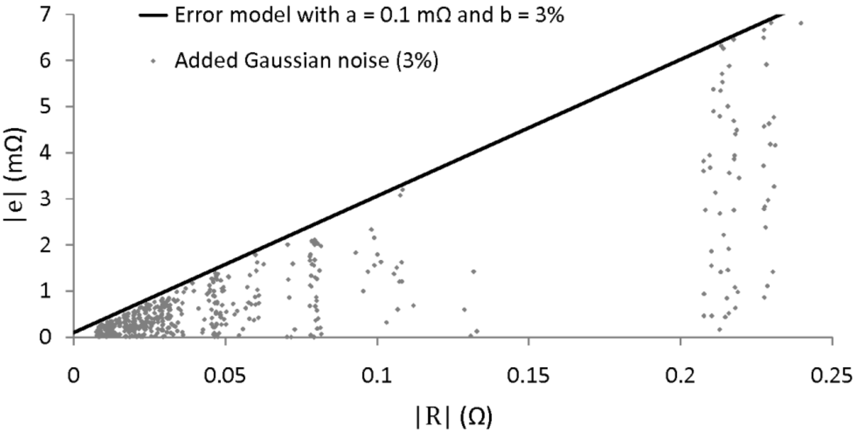

Figure 5.9: The real data error level is difficult to estimate. To take into account this difficulty into our synthetic case study, we estimated an error model based on the true data errors we added in the synthetic data (3% of Gaussian noise). We used the Slater et al. (2000) approach (see section 2.3) that uses the line which encompass all data errors in the (|R|, |e|) plane. The error model parameters are equal to 0.1 mΩ (absolute error parameter – a) and 3% (relative error parameter – b).

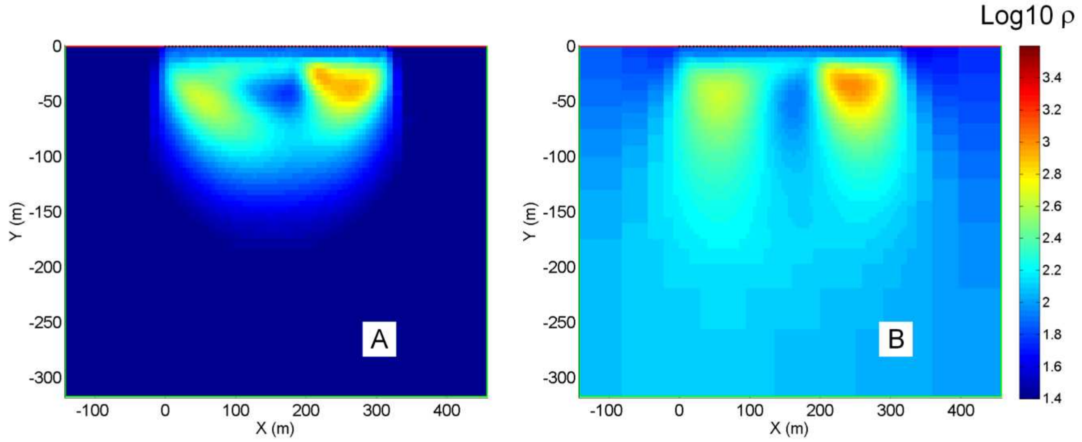

Figure 5.10: The only parameter that changed between these two CRTomo inversions is the value of the homogeneous reference model – 20 Ω.m (A) and 2000 Ω.m (B). We used the approach of Oldenburg and Li (1999) to estimate the depth of investigation of our inverted model (see section 2.4.4). Below a depth of 100 m, both models return to the value of the reference model. Hereafter, we will limit the model depth to 100 m.

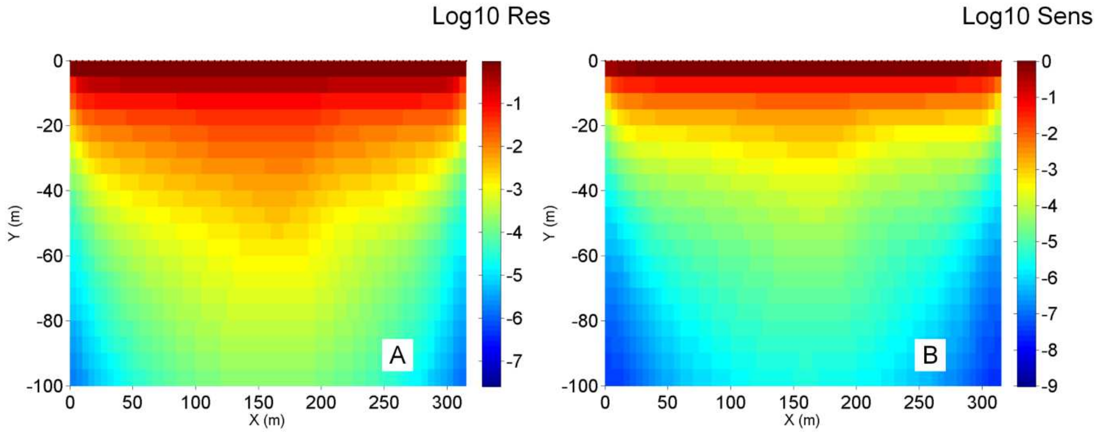

Figure 5.11: In terms of image appraisal, one can also use the diagonal values of the resolution matrix (A) or the cumulative sensitivity matrix (B). In this thesis, we choose to only present the cumulative sensitivity matrix because both resolution indicators give approximately the same results (see Figure 5.10). Moreover, the computation time needed for the resolution matrix is higher than the one needed for the cumulative sensitivity matrix. With the cutoff values estimated in Figure 5.12, we can calculate the depth of investigation to about 35 m in the central part of the inverted model.

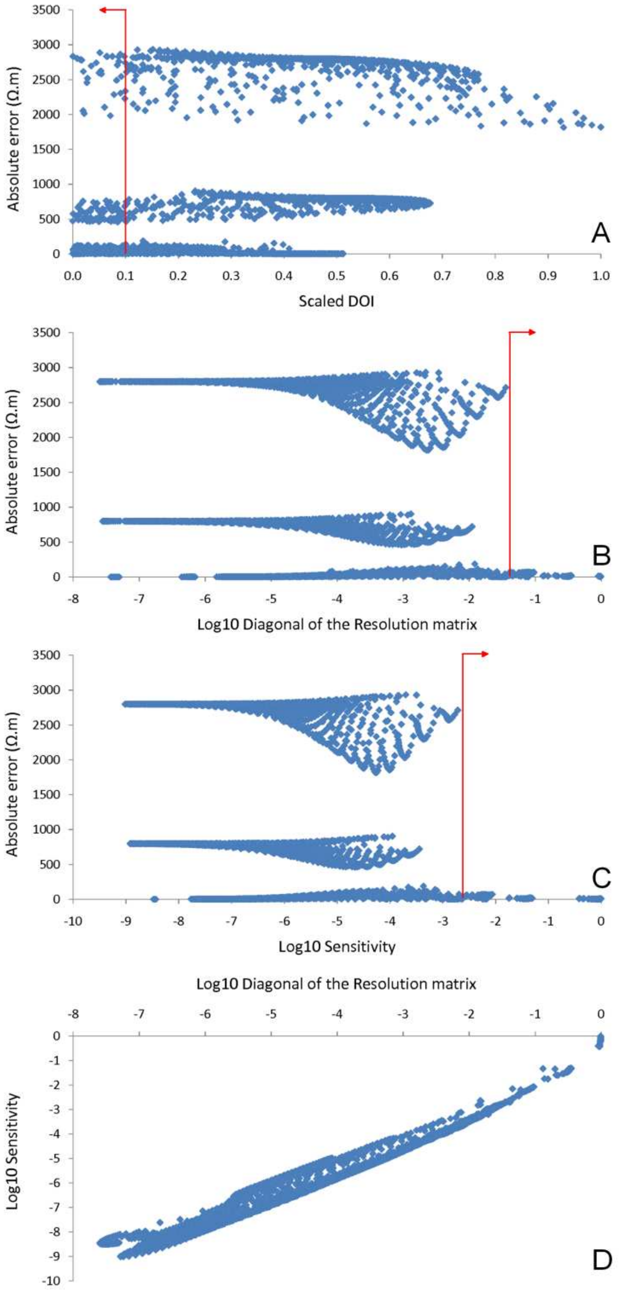

Figure 5.12: Three different resolution indicators are presented versus the absolute error – the error between the true model and the inverted model using a smoothness constraint – in order to estimate a value below/above which the associated electrical structures should be interpreted with caution since they do not rely only on data. For the DOI index (A), Oldenburg and Li (1999) used a value of 0.1 but in our case, completely false structures are kept. This is not the case with the resolution matrix (B) or the cumulative sensitivity matrix (C) that present a similar behavior (D). Indeed, cutoff values rejecting false structures can be found for these two resolution indicators.

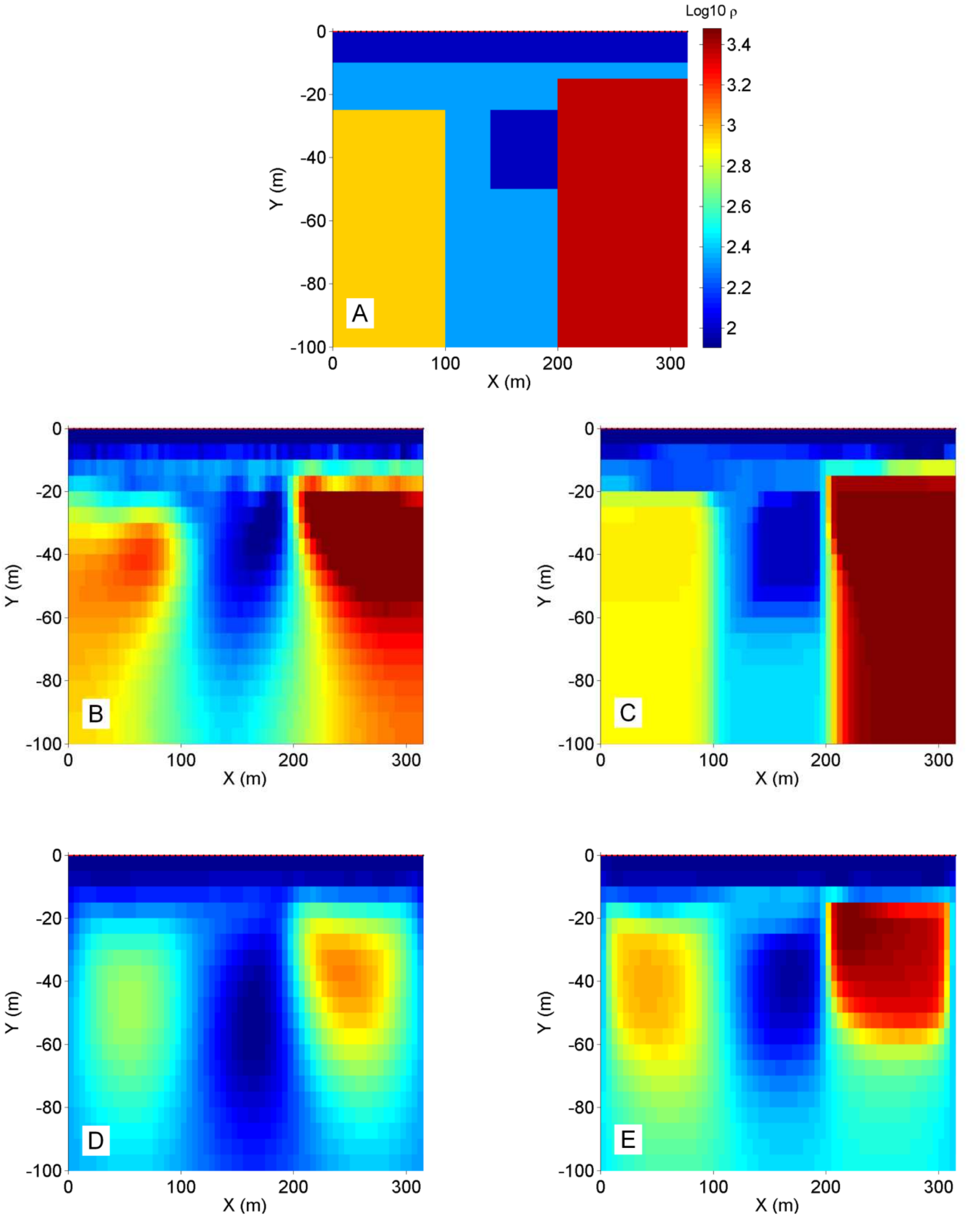

Figure 5.13: Compared to the true resistivity model (A), the two smoothness-constraint inversions, with Res2Dinv (B) and CRTomo (D), do not recreate the different sharp limits as well as the blocky inversion performed with Res2Dinv (C) and the inversion using the MGS approach – β = 0.05 – with CRTomo (E).

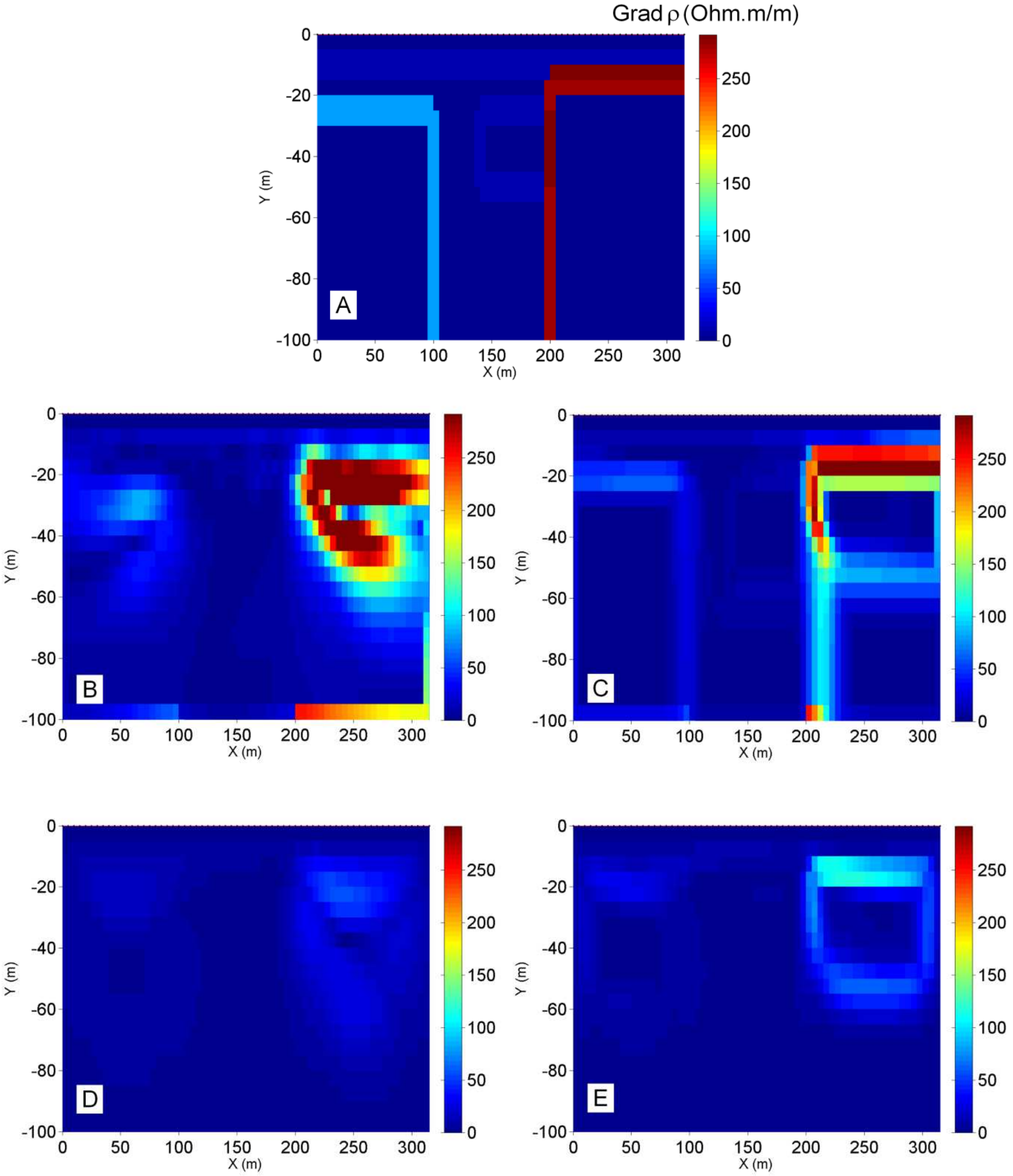

Figure 5.14: In terms of resistivity gradients (in Ω.m/m), the best inversion procedures seem to be the blocky inversion (C) available in Res2DInv and the MGS approach – β = 0.05 – (E) available in CRTomo since the maximal gradients correspond well in value and position with the true resistivity gradients (A). With the blocky model, it is also possible to image the karstified area (see Figure 5.13). The two smoothness-constraint inversions – with Res2Dinv (B) and CRTomo (D) – do not recreate so well the different sharp limits and should not be used when prior information indicates sharp limits.

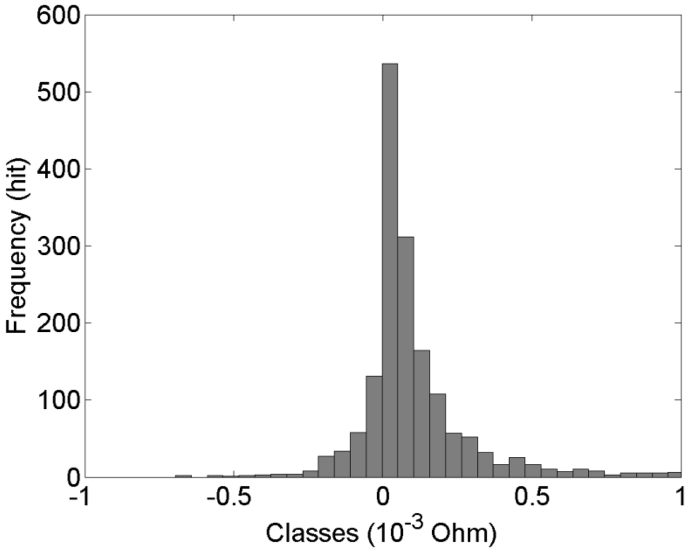

Figure 5.15: This histogram (in mΩ) presents the reciprocal error distribution of profile P2 in the Havelange calcareous valley. The distribution is normal and centered on zero. The standard deviation (σ) value is equal to 0.25 mΩ. Therefore, ±96% of the reciprocal errors are comprised between -0.5 and 0.5 mΩ, that is ±2σ.

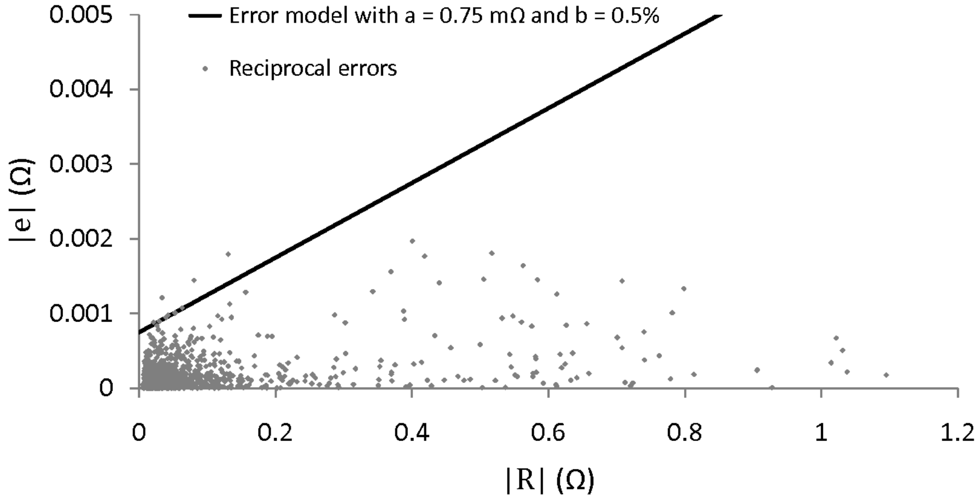

Figure 5.16: Reciprocal measurements were collected for the entire profile P2, except for the third (last) roll-along sequence. As a consequence, we developed an error model based on the Slater et al. (2000) approach for the inversion. The error model parameters are equal to 0.75 mΩ (absolute error parameter – a) and 0.5% (relative error parameter – b).

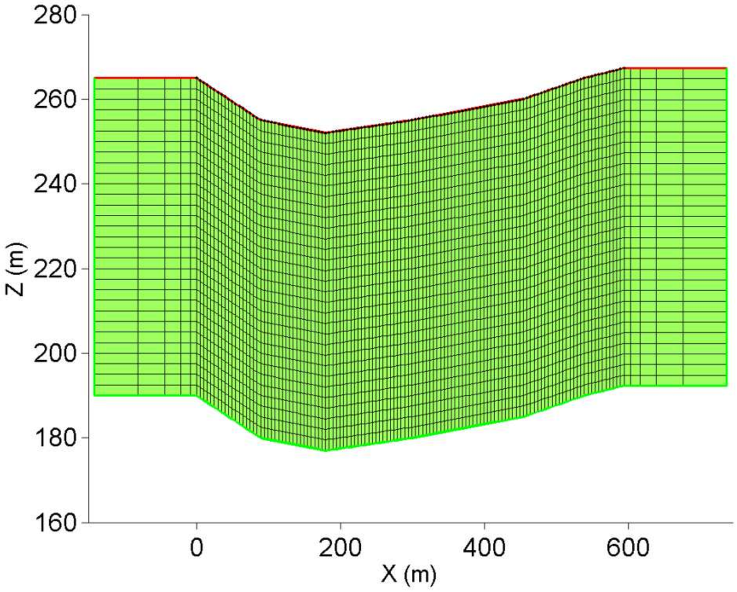

Figure 5.17: The mesh of the profile P2 takes into account the topography of the Havelange calcareous valley. The main mesh is composed of 119 x 30 finite elements of 5 x 5 m whereas it is extended by 5 x 30 finite elements with increasing width in both sides to account the boundary conditions.

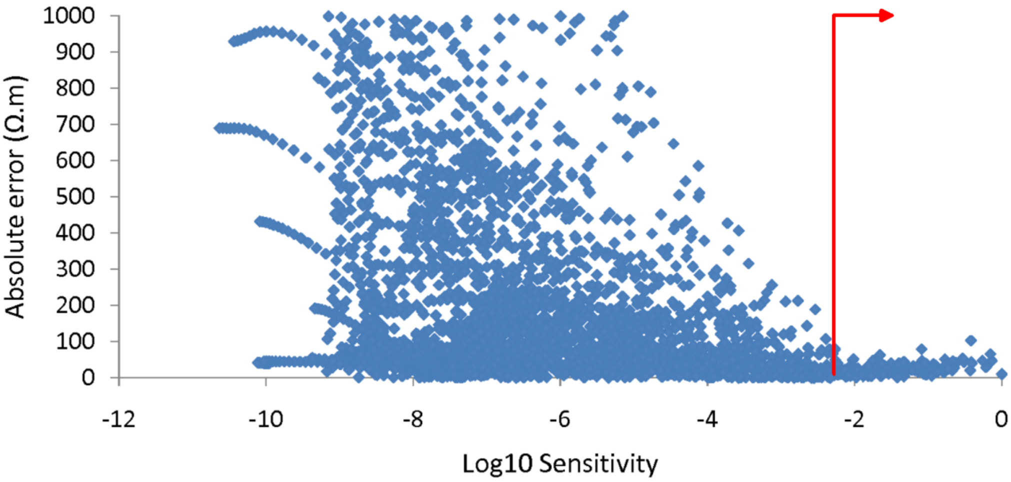

Figure 5.18: In a real case study, it is not possible to have access to the true resistivity model since it is what we are searching for. In order to select a cutoff for the cumulative sensitivity matrix, we used the inverted model as a true model and we ran a forward modeling to obtain a new data set that was again inverted. Obviously, we kept the same acquisition or inversion parameters. The error between both inverted models is then plotted versus the sensitivity to obtain the cutoff value (about 10^{-2}).

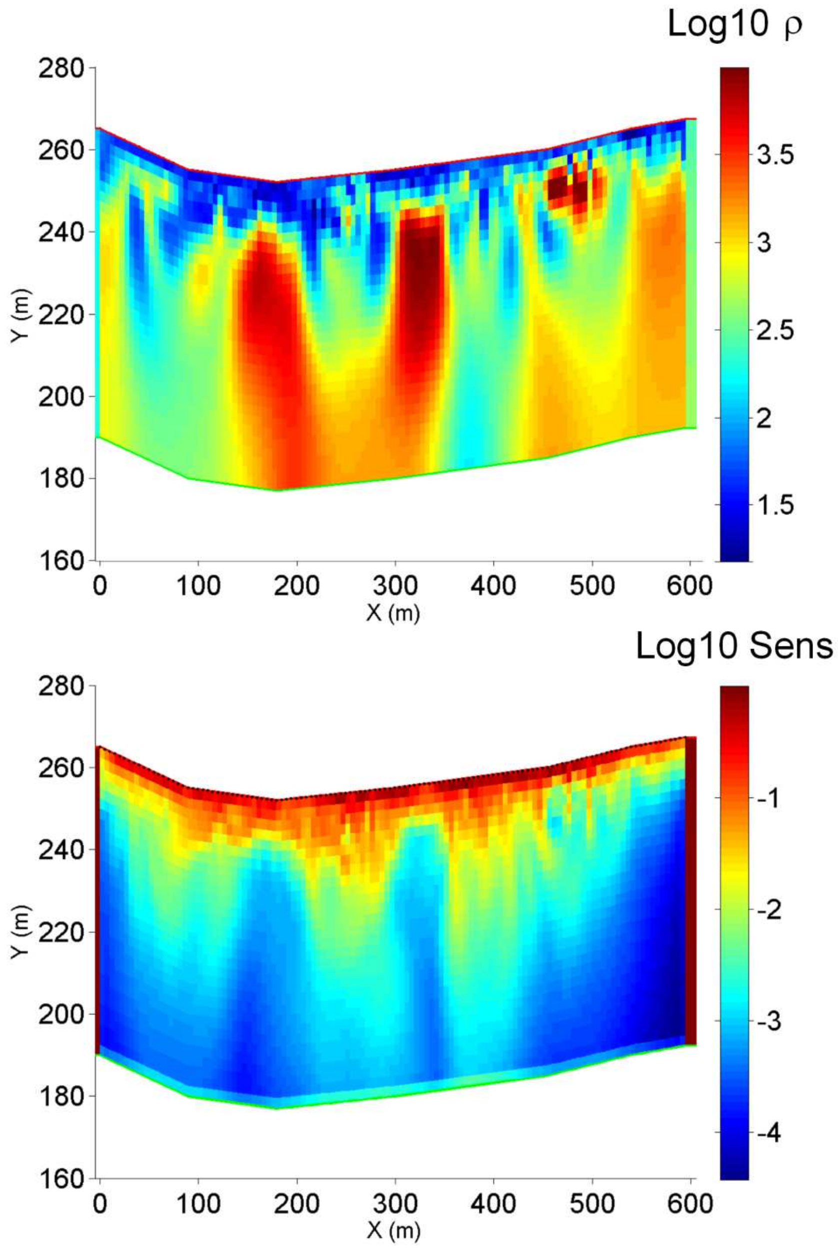

Figure 5.19: If we select 0.01 as a cutoff for the cumulative sensitivity matrix (bottom panel), we can see that the depth of investigation is around an elevation of 230 m (a depth of 30 m below surface). The three conductive layers in this profile P2 are well marked (top panel) and their sensitivity is higher than the selected cutoff. Therefore, we can interpret these conductive layers in terms of geology; e.g., these are fractured area in the Havelange calcareous valley.

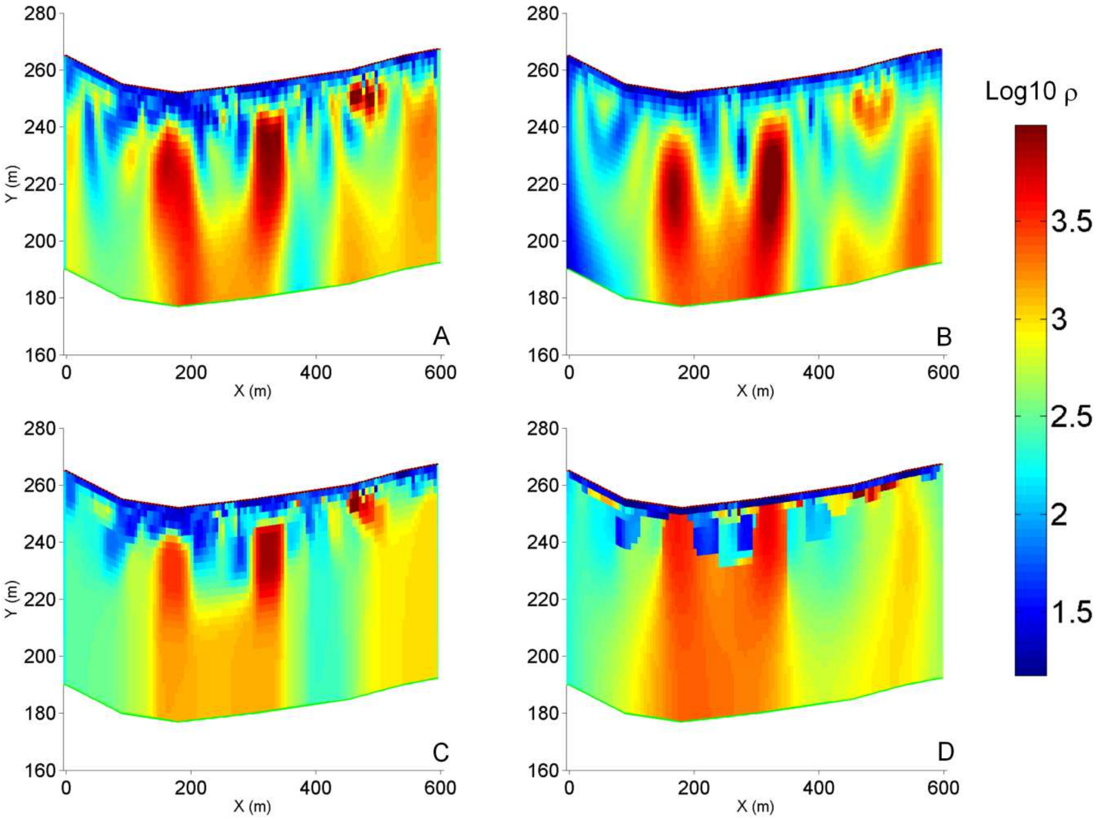

Figure 5.20: The four inverted models present three clear conductive zones which are discussed in details in section 7.1. However, the inverted models obtained with a blocky inversion (C) or using a MGS approach (D) present simpler electrical structures and sharper contrasts than the smooth inverted models – (A) with Res2DInv and (B) with CRTomo. Nevertheless, the MGS approach places the gradients limits closer to the surface than the blocky or smoothness-constraint inversions.

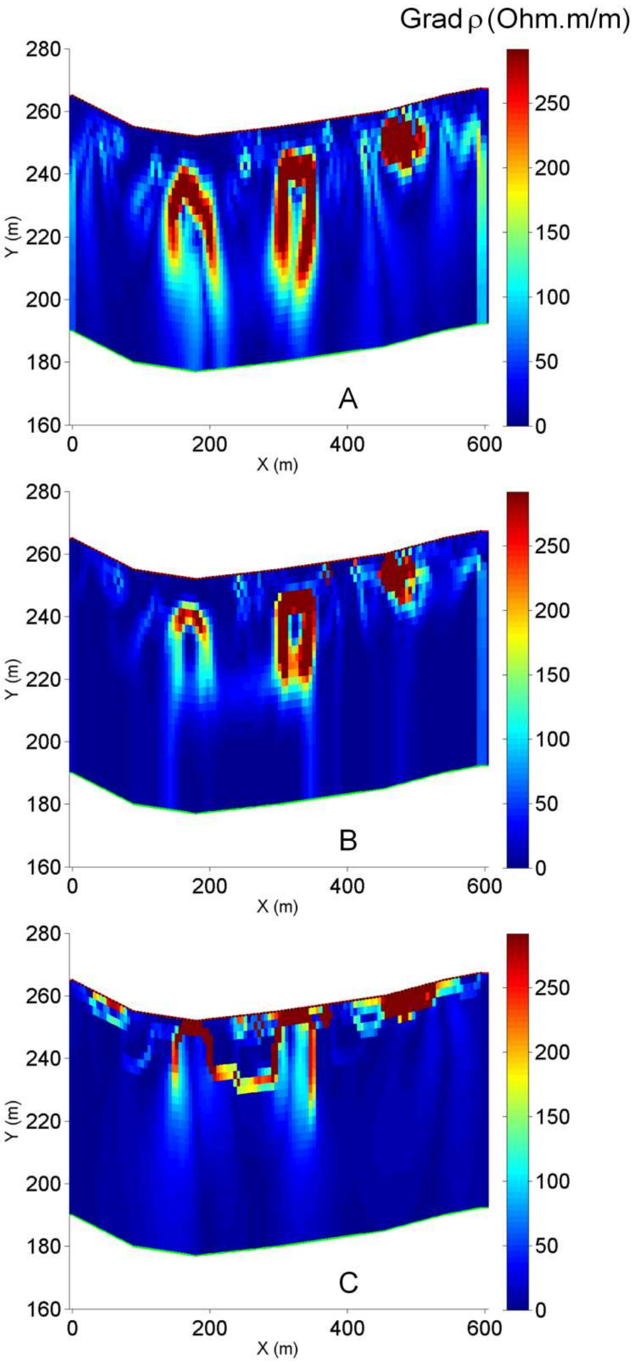

Figure 5.21: These gradients images of the P2 ERT profile present three major gradients. Starting from the right, the first gradient is close to the surface and is related to a limestone outcrop that rises in the overburden. The second and third gradients are more in depth and are related to the limits of more fractured areas. The smoothness-constraint (A) and the blocky (B) inversions place these gradients more in depth than the inversion using the MGS approach (C).

References

Blaschek, R., A. Hordt, and A. Kemna, 2008, *A new sensitivity-controlled focusing regularization scheme for the inversion of induced polarization data based on the minimum gradient support*, Geophysics, 73 (2), F45-F54.

Hilbich, C., L. Marescot, C. Hauck, M. H. Loke, and R. Mäusbacher, 2009, *Applicability of Electrical Resistivity Tomography Monitoring to coarse blocky and ice-rich permafrost landforms*, Permafrost and Periglacial Processes, 20, 269-284.

Kemna, A., 2000, *Tomographic inversion of complex resistivity : theory and application*, PhD Thesis, University of Bochum.

Loke, M. H., and R. D. Barker, 1996, *Rapid least-squares inversion of apparent resistivity pseudosections by a quasi-Newton method*, Geophysical Prospecting, 44 (1), 131-152.

Loke, M. H., I. Acworth, and T. Dahlin, 2003, *A comparison of smooth and blocky inversion methods in 2D electrical imaging surveys*, Exploration Geophysics, 34 (3), 182-187.

Marescot, L., M. H. Loke, D. Chapellier, R. Delaloye, C. Lambiel, and E. Reynard, 2003, *Assessing reliability of 2D resistivity imaging in mountain permafrost studies using the Depth Of Investigation index method*, Near Surface Geophysics, 1, 57-67.

Nguyen, F., S. Garambois, D. Jongmans, E. Pirard, and M.H. Loke, 2005, *Image processing of 2D resistivity data for imaging faults*, Journal of Applied Geophysics, 57 (4), 260-277.

Nguyen, F., A. Kemna, A. Antonsson, P. Engesgaard, O. Kuras, R. Ogilvy, J. Gisbert, S. Jorreto, and A. Pulido-Bosch, 2009, *Characterization of seawater intrusion using 2D electrical imaging*, Near Surface Geophysics, 7 (5-6), 377-390.

Oldenburg, D. W., and Y. Li, 1999, *Estimating depth of investigation in dc resistivity and IP surveys*, Geophysics, 64 (2), 403-416.

Portniaguine, O., and M. S. Zhdanov, 1999, *Focusing geophysical inversion images*, Geophysics, 64 (3), 874-887.

Robert, T., D. Caterina, J. Deceuster, O. Kaufmann, and F. Nguyen, 2012, *A salt tracer test monitored with surface ERT to detect preferential flow and transport paths in fractured/karstified limestones*, Geophysics, 77 (2), 1-13.

Slater, L., A. M. Binley, W. Daily, and R. Johnson, 2000, *Cross-hole electrical imaging of a controlled saline tracer injection*, Journal of Applied Geophysics, 44 (2-3), 85-102.

6. Characterization and monitoring

Geophysical monitoring allows studying the dynamics of bulk physical properties which can then be interpreted in terms of physical processes such as hydrodynamics. As an example, a variation in the subsurface electrical resistivity distribution can occur from different causes including – among many others – a change in the water table elevation, a change in the moisture content, a change in the groundwater chemistry, or a change in groundwater temperature.

Geophysical monitoring has now become an essential tool to study the dynamics of reservoirs whether the process is related to flow or to solute transport, and whether it is physically forced (e.g., salt tracer, pumping, and injection tests) or natural (e.g., seasonal variations of the water table or the moisture content).

In this chapter, we will first present the results of an ERT and SP monitoring study showing the ability of the SP method to follow the natural dynamics of the hydraulic gradient related to the southern flank of a calcareous valley of southern Belgium where ERT failed to do so using natural variations only. Then, we will focus on a physically forced process to infer some groundwater flow and solute transport parameters by monitoring, using surface ERT, a salt tracer test in a fractured and karstified limestone aquifer. Finally, we will compare and discuss several time-lapse model constraints in DC electrical data inversion for the characterization of fractured aquifers, focusing on noise characterization.

6.1. ERT and SP monitoring of seasonal variations of hydraulic gradients

In section 4.3, we presented a conceptual model of a typical Condruzian system where groundwater discharges appear in the contact between the sandstone aquifer and the shale hydraulic barrier. This water then either runoffs from the springs along the topography and/or recharges the limestone aquifer.

The dynamics of this water exchange depends on the season. Indeed, in low groundwater level periods when the water table in the sandstone aquifer is too deep, springs – that recharge the limestone aquifer – are not supplied by groundwater anymore. One can therefore expect a decrease in the hydraulic gradient related to the flank of the calcareous valley. In contrary, in high groundwater level periods, the water recharge in the limestones aquifer increases again, as does the corresponding hydraulic gradient. This dynamics is difficult to visualize since it requires a dense monitoring network that is not always available due to obvious financial and logistical constraints.

In Robert et al. (2011), we presented an SP profile that images the hydraulic gradient of the southern flank of the Havelange calcareous valley (see section 5.3). We used the water table model (e.g., Fournier, 1989; Revil et al., 2003) that relates the SP signal directly to the difference in hydraulic heads, given the knowledge of the electrokinetic coupling coefficient C' (see section 3.2), to image the water table distribution.

The idea of this study was to monitor these hydraulic gradients with ERT and SP in order to image the drawdown of the water table and the possible seasonal decrease/increase of the hydraulic gradients, but also to highlight eventual changes in groundwater flow through preferential paths. To do so, we investigated two different calcareous valleys – the Havelange (Figure 6.1) and the Evelette (Figure 6.2) synclines – where we previously identified contrasted SP results. We also chose these sites because of their shallow water table which is between 8 and 12 m below surface.

In the Havelange syncline (Figure 6.1), the hydraulic gradient that we wanted to monitor is related to the southern flank of the calcareous valley. As previously mentioned, an SP profile measured in September 2008 presented a strong SP gradient indicating a strong hydraulic gradient along the profile, according to the water table model.

In the Evelette syncline (Figure 6.2), the relief is much flatter than the Havelange valley because the syncline structure is stopped with a fault system in the south. The water table distribution is in relation with the flat area and is therefore quite horizontal. Here, we expected no change in the hydraulic gradient value in the Evelette syncline as it was previously highlighted with an SP profile measured in January 2008 (Robert et al., 2011).

We positioned our monitoring lines in a NW – SE direction, perpendicular to the geological structures (Figure 6.1 and Figure 6.2). We used 64 stainless steel electrodes spaced by 5 m with a dipole-dipole configuration ($n \leq 6$) for the ERT profiles. This resulted in a profile length of 315 m. We used an ABEM Lund Imaging System SAS1000 (one recording channel) for the data collection. With this dipole-dipole sequence, we collected up to 1015 measurements per ERT profile.

In order to evaluate the data quality, we performed 3 to 6 stacks with a standard deviation of 1%. The repetition error which corresponds to the standard deviation value of the stacked signal has a maximum value of 4% for the Havelange profile and 5% for the Evelette profile. The repetition error distributions which are lognormal are presented in Figure 6.3 and Figure 6.5 for the Havelange and Evelette ERT profiles, respectively.

We also collected reciprocal measurements (swapping current and potential electrodes) to evaluate the noise level through the reciprocal errors. The reciprocal error distributions which are normal and centered on zero are presented in Figure 6.3 and Figure 6.5 for the Havelange and Evelette ERT profiles, respectively.

The reciprocal error is one order of magnitude higher than the repetition error since it is comprised – after the removal of a few outliers – between -40 and 40% for the Havelange profile and between -50 and 50% for the Evelette profile. We calculated an error model based on the approach of Slater et al. (2000) to estimate the true data noise level. These error models are presented in Figure 6.4 and Figure 6.6 for the Havelange and Evelette ERT profiles, respectively. We used the same error model for both sites which is 5 mΩ for the absolute error model parameter (a) and 1% for the relative error model parameter (b); see Eq. (2.5).

We centered the profiles on the piezometer positions (see Robert et al., 2011) in order to correlate the electrical resistivity and the SP changes with hydraulic head values. We performed a one year monitoring of the hydraulic heads in the Havelange F11 (Figure 6.7) and

Evelette F5 (Figure 6.8) piezometers thanks to two pressure head probes (In-Situ Inc. miniTROLL) that measured the hydraulic head and the temperature every 30 minutes.

We placed this pressure head probes in the piezometers because our first time-lapse ERT results presented highly erratic distribution (Figure 6.9). One reason of the strong artifacts presence in our time-lapse images is related to the fact that we had to remove and place the steel electrodes again each time to allow the farmer to plow its field or plant its crop between the different time series. Even if we collected every electrodes position with a differential GPS (Leica GPS 1200, Leica Geosystems), it was not possible to hammer them back in the right place. This led to spacing errors (±5 cm given the differential GPS precision) that affected the time-lapse data set. Moreover, the electrical contact resistances between two time series changed resulting in a different noise level between two time-lapse acquisitions.

Different physical parameters can also induce a natural change in the bulk electrical resistivity distribution. We already saw in section 4.4 that the groundwater geochemistry – pH, hardness, and electrical conductivity – does not vary significantly over time. The time series collected by the pressure head probes in F11 and F5 (Figure 6.7 and Figure 6.8) show that the temperature did not vary more than 0.12°C between different seasons. This slight difference in temperature cannot be imaged with time-lapse ERT at our working scale. The pressure head probes also recorded the water table elevation. The maximum difference in the water table elevation between different seasons is approximately equal to 5 m (F11) and 2.5 m (F5). Given our working scale (we used a unit electrode spacing of 5 m), it is unlikely that time-lapse ERT could image this natural fluctuation of the water table. For all these reasons, we will only present one monitoring ERT result, which demonstrates its inability to map these natural fluctuations (Figure 6.9), and the results of the SP monitoring.

The electrical image of the southern flank of the Havelange calcareous valley is presented at the bottom of Figure 6.10. The overburden – 5 to 10 m thick – composed of clay loam presents conductive structures with resistivity values ranging between 20 to 80 Ω.m. This conductive layer can also be related to the upper weathered mantle of the limestones. At a depth of 10 m below surface, we assume that the limestone bedrock is fully saturated because the water table is at a depth of about 10 m below surface in the F11 piezometer. The limestone bedrock presents quite conductive electrical structures for saturated limestones with values ranging between 100 and 620 Ω.m. This is an indication of fractured or at least, not compact, limestones.

The electrical image of the Evelette calcareous valley is presented at the bottom of Figure 6.11. Two different areas can be distinguished with very conductive electrical structures (20 to 80 Ω.m) before a distance of 170 m along the profile and slightly higher values (120 to 440 Ω.m) but still quite conductive after 170 m. As a consequence, it is difficult in the first half of the profile to isolate the overburden from the limestone bedrock because the resistivity model presents no electrical contrast. In the second half of the profile, the overburden – 10 m thick and here composed of sand – can be discriminated from the limestone bedrock. Again, such low resistivity values for saturated limestones – the water table is at a depth of about 12 m – indicate a highly fractured/karstified area.

Concerning the SP measurements acquisition, we spaced every SP station by 5 m and the locations of these stations correspond to the ERT electrode positions. We placed the fixed base electrode at the beginning of the monitoring line (0 m). We dug three holes at each SP station and we filled them with a mud composed of water saturated in salt and bentonite to improve the electrical contact between the soil and the non polarizable electrodes (see section 3.3). We also changed the fixed base electrode position every 40 m since we saw that after 50 m, the SP signal started to be unstable. The final SP signal was corrected for the base drift and brought back at the first base position (0 m).

In January 2008, we used a METRIX MX 20 voltmeter (internal impedance > 10^7 Ω) to measure the self electrical potential. As it is explained in Robert et al. (2011), we started to have problems with this voltmeter because it was not designed to endure such difficult conditions (wet and cold weather). For all the SP measurements taken after this campaign, we used a METRIX MX 59 HD (for heavy duty) voltmeter of similar impedance.

We collected three measurements per SP station in order to evaluate the standard deviation value of the SP signal – taken as an estimation of the SP error – associated to a particular SP station. The problem we got with our first voltmeter was reflected in the corresponding SP signal (Figure 6.11) since the SP errors of the survey performed in January 2008 in the Evelette line present higher values (±4 mV) than the following surveys in December 2009 and January 2010 (±1 mV). For the Havelange surveys (Figure 6.10), we only used the new voltmeter and we obtained a very low noise level (±1 mV except for a few stations). Therefore, a good confidence can be placed in the SP signals measured in Havelange (Figure 6.10) or in Evelette (Figure 6.11).

The SP signals measured in the Evelette line (Figure 6.11) are reproducible since the main anomaly that is centered on the F5 piezometer position is retrieved in all three profiles. Except this strong negative anomaly that is related to a preferential flow path in a fractured/karstified area (Robert et al., 2011), the signals present no specific gradient. This is in agreement with the assumption that in this area, the water table distribution should be horizontal, meaning that the hydraulic gradient perpendicular to main drainage direction is almost zero.

The SP signals measured in the Havelange line (Figure 6.10) are reproducible and present both a strong gradient after a distance of 40 m along the profile. This gradient is higher in September 2008 (0.173 mV/m) than in December 2009 (0.140 mV/m). These two dates correspond to a high and low groundwater level period, respectively. Every other characteristic of these SP signals is discussed in details in Robert et al. (2011).

In these calcareous valleys, we can assume that the dominant contribution to the SP signal is related to the electrokinetic effect. We saw previously that the parameters that could possibly influence the electrokinetic coupling coefficient value (see section 3.2) do not vary significantly during the seasons (e.g., pH, temperature, and fluid electrical conductivity, among many others). Therefore, if significant changes are highlighted between two time series, they should be interpreted in terms of groundwater flow.

We used the water table model to image the changes in the hydraulic head distribution along the monitoring line positioned on the southern flank of the Havelange calcareous valley. To do so, we assumed that the apparent coupling coefficient of the electrokinetic effect was constant over time. Then, we used the same value for this apparent coupling coefficient as the one estimated in Robert et al. (2011) which was 2.7 mV/m. Even if this value only represents an order of magnitude, we believe it is sufficient to demonstrate the ability of the SP method to image changes in hydraulic gradients.

The water table model relates the electrical (self) potential measured between two points to the difference in hydraulic heads between these two points. To convert these hydraulic heads differences into water table elevation, one needs at least a measurement of the water table elevation. Therefore, we measured the hydraulic head in the F11 piezometer every time we collected SP measurements. The water table elevation in F11 was measured at 247.74 m and 243.87 m in September 2008 and December 2009, respectively. These dates corresponded respectively in a high and low groundwater level periods.

We reconstructed the water table distribution using only the main trend of the signal. This way, we avoid interpreting little oscillations that were possibly related to small contrasts in the bulk electrical resistivity or to the presence of perpendicular preferential flow paths. However, the static electrical image of the southern flank of the Havelange syncline presents quite homogeneous electrical structures (Figure 6.10). The reconstructed water table distributions corresponding to both time series are presented in Figure 6.12.

The results of this water table reconstruction validate the assumption that the hydraulic gradient decreases during a low groundwater level period (e.g., in December 2009) and increases during a high groundwater level period (e.g., in September 2008). This study leads to great perspectives in terms of hydrogeological watershed studies at the scale of a watershed relevant for real world applications, especially when looking at the dynamics of complicated systems such as the Condruzian system we investigated here. Obviously, a denser monitoring network is still needed for a more quantitative study, for example to better estimate the electrokinetic apparent coupling coefficient. However, for a qualitative comprehension of the dynamics of a hydrogeological basin, the utility of the SP method – when measurements are possible – is now well known.

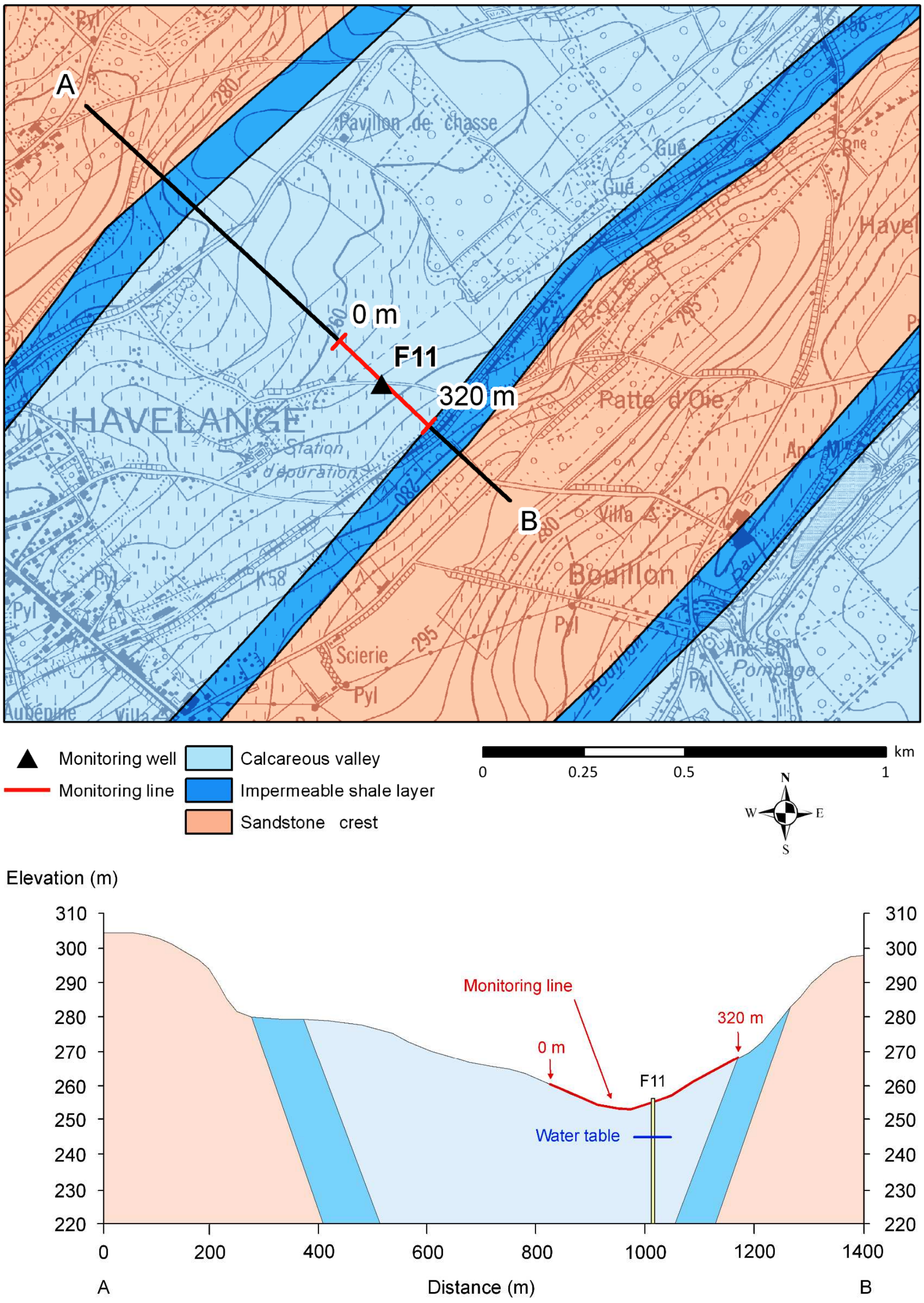

Figure 6.1: The Havelange syncline is a typical calcareous valley of the Condroz Region with a well marked topography. We positioned our monitoring line on the southern flank of this valley and we centered it on the F11 piezometer. The water table elevation is at about 245 m and this corresponds to a depth of about 10 m below surface. A previous SP profile performed on this line showed a strong hydraulic gradient along this direction.

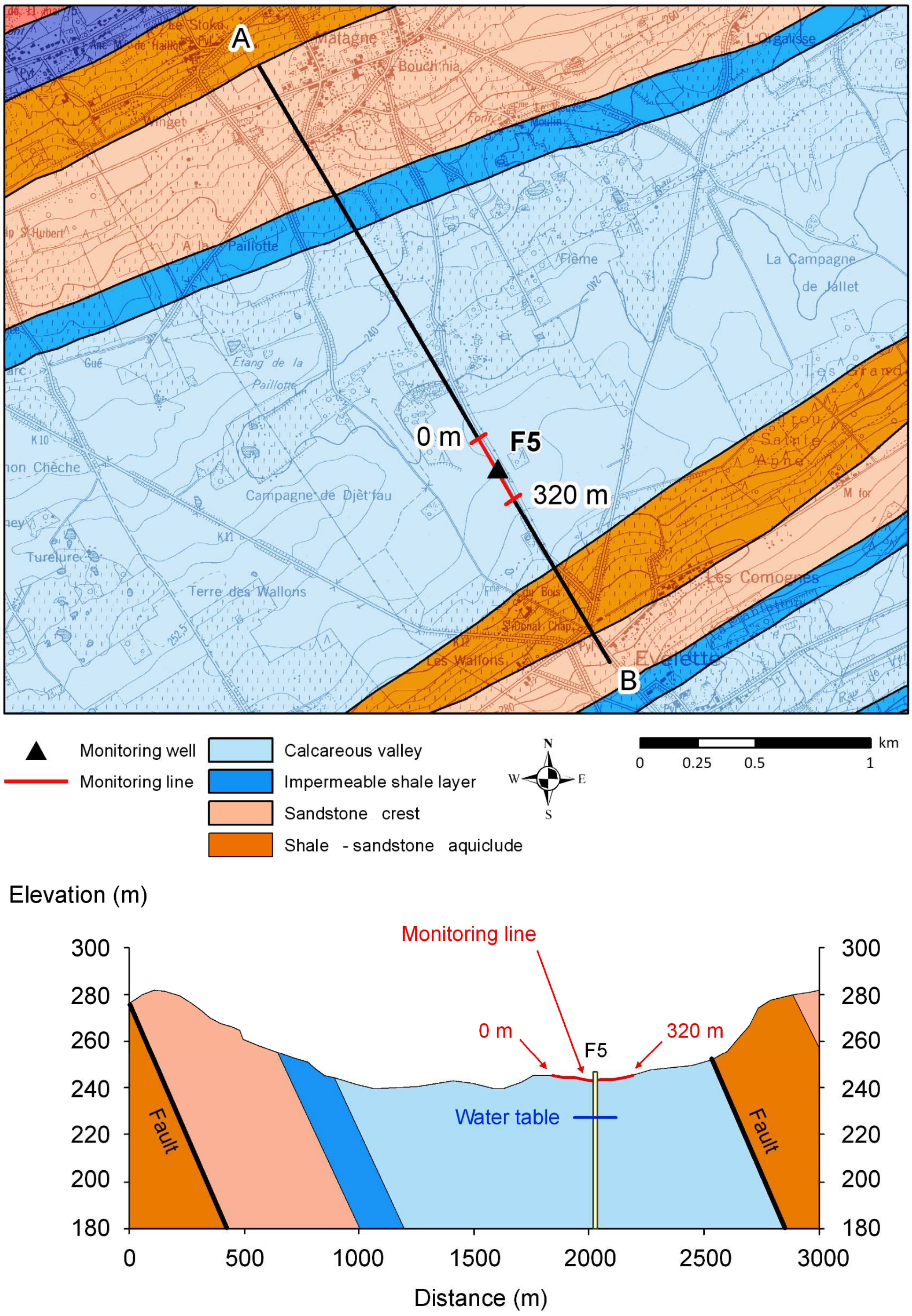

Figure 6.2: In the Evelette syncline, we positioned our monitoring line in the central part of the valley and we centered it on the F5 piezometer. The water table elevation is at about 230 m and this corresponds to a depth of about 13 m below surface. A previous SP profile performed on this line showed a flat signal along this direction – meaning a horizontal water table distribution.

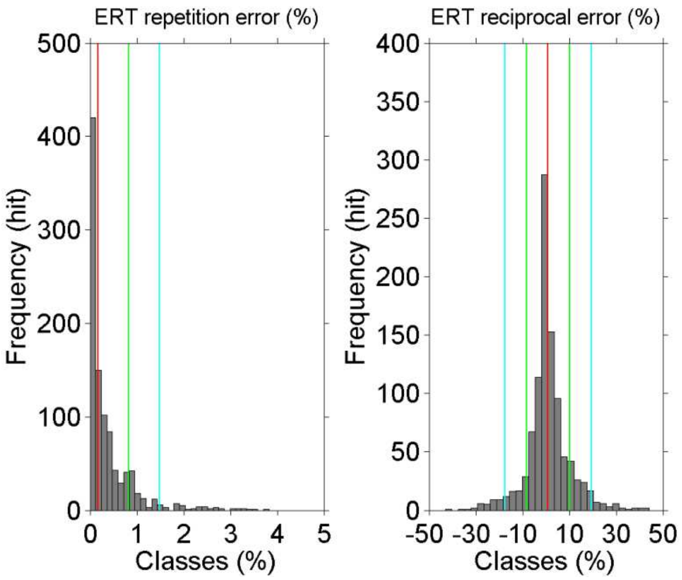

Figure 6.3: The repetition error distribution of the Havelange ERT profile which is lognormal presents values below 4% and the corresponding standard deviation value σ is equal to 0.8%. The reciprocal error distribution which is normal and centered on zero presents values that are one order of magnitude higher than the repetition error and comprised between -40 and 40%. The standard deviation value σ of the reciprocal error distribution is about 9%. The interval m±σ where m is the mean value of the reciprocal error (red line) is represented by green lines whereas the interval m±2σ – which contains ±96% of the reciprocal errors – is represented by blue lines. Such high noise level was common with an ABEM Lund Imaging System SAS1000.

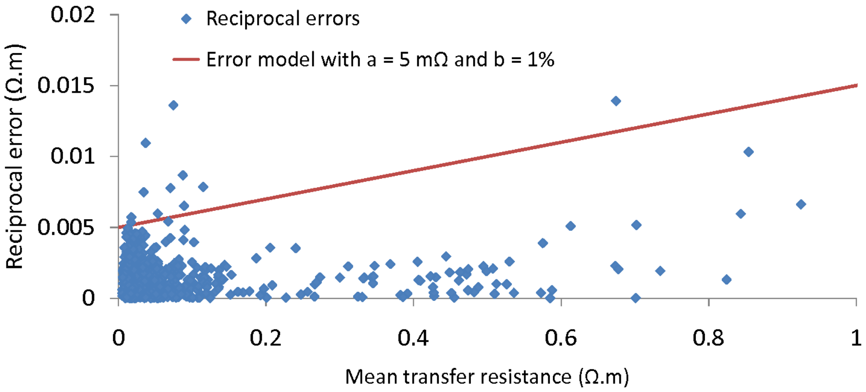

Figure 6.4: The error model for the ERT profiles of site F11 is equal to 5 mΩ for the absolute error model parameter (a) and 1% for the relative error model parameter (b). We used the same error model for site F5 (Figure 6.6).

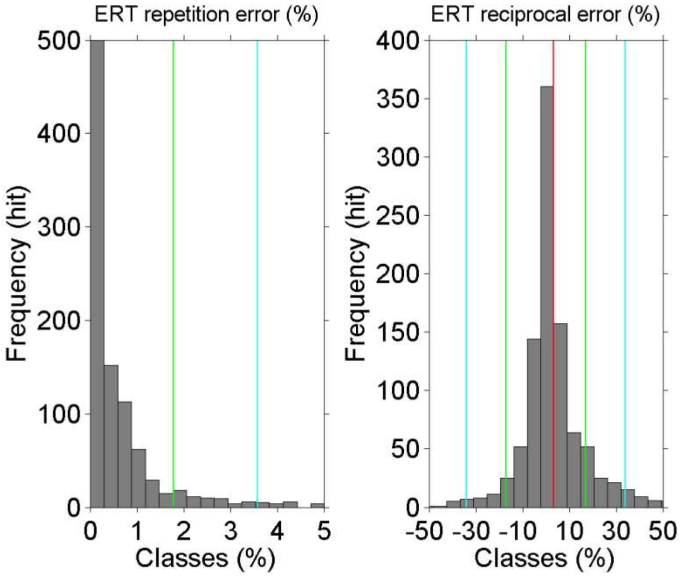

Figure 6.5: The repetition error distribution of the Evelette ERT profile which is lognormal presents values below 5% and the corresponding standard deviation value σ is equal to 1.8%. The reciprocal error distribution which is normal and centered on zero presents values that are one order of magnitude higher than the repetition error and comprised between -50 and 50%. The standard deviation value σ of the reciprocal error distribution is about 12%. The interval m±σ where m is the mean value of the reciprocal error (red line) is represented by green lines whereas the interval m±2σ – which contains ±96% of the reciprocal errors – is represented by blue lines. Such high noise level was common with an ABEM Lund Imaging System SAS1000 as it is proved here with the reciprocal error level for the Havelange but also the Evelette ERT profiles.

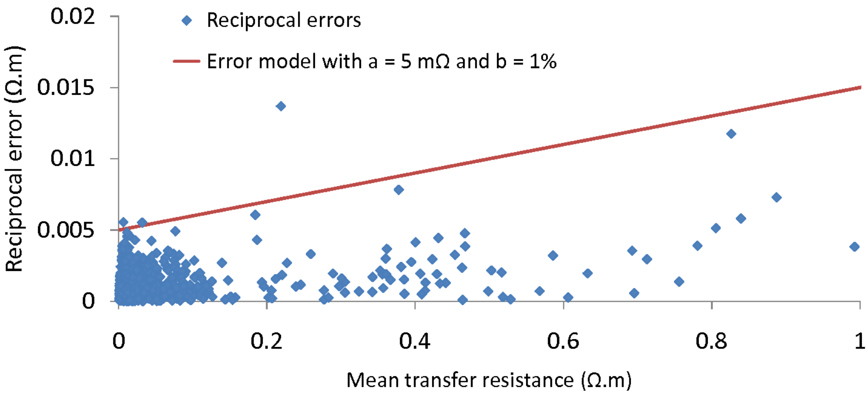

Figure 6.6: We used the same error model as the one of site F11 (Figure 6.4) for site F5. It is equal to 5 mΩ for the absolute error model parameter (a) and 1% for the relative error model parameter (b).

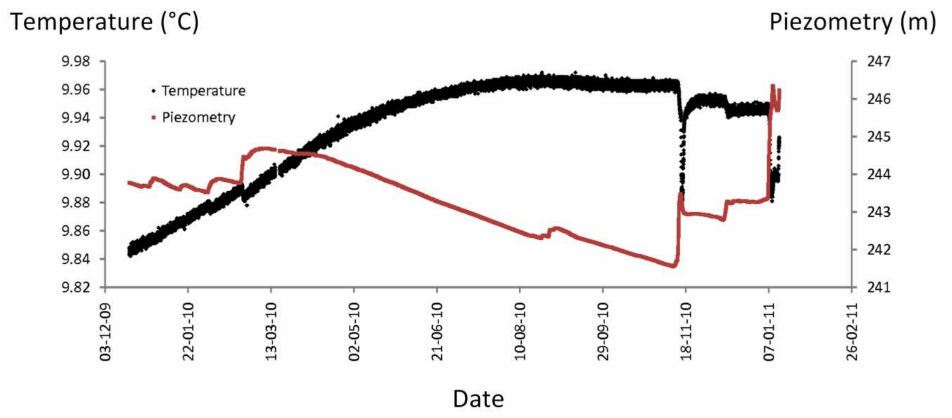

Figure 6.7: The pressure head probe placed in piezometer F11 (Havelange) recorded more than one year of hydraulic heads and temperature measurements (one every 30 minutes). The temperature did not change much during one year (a maximum of 0.12°C) and should not lead to changes in the bulk electrical resistivity. The water table elevation varied between 242 and 247 m (a maximum of 5 m) during this specific year. Given our working scale, it is unlikely that the water table fluctuation could be imaged with time-lapse ERT. The temperature and piezometry time series also present a good correlation. Indeed, after strong rainfall or snowmelt events – such as in mid-November 2010 and mid-January 2011 – the temperature decreases abruptly whereas the piezometry increases all so abruptly.

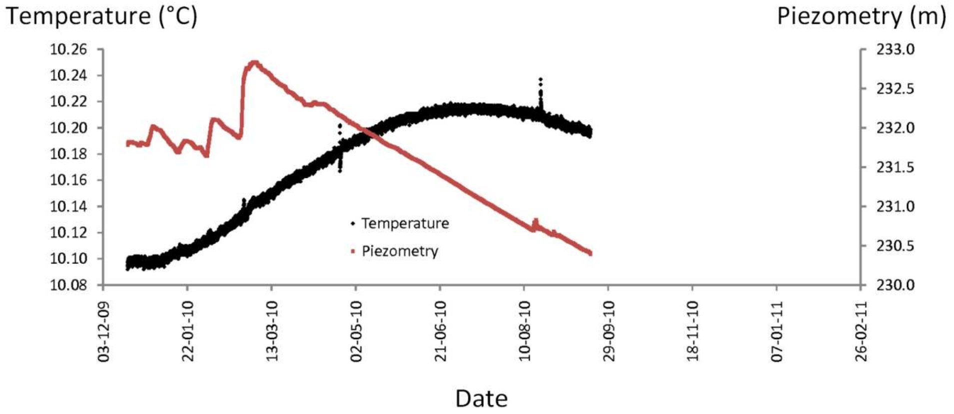

Figure 6.8: The pressure head probe placed in piezometer F5 (Evelette) did not record one entire year of hydraulic heads and temperature measurements because this piezometer was inserted in an automatic monitoring network of the Walloon Region of Belgium which led to the removal of our probe. Here, changes in temperature were also very low (a maximum of 0.12°C). The water table elevation was at its minimum in December 2010 (230 m) and at its maximum in July 2010 (232.5 m). As for site F11, it is unlikely that the temperature and the water fluctuation could be imaged with time-lapse ERT.

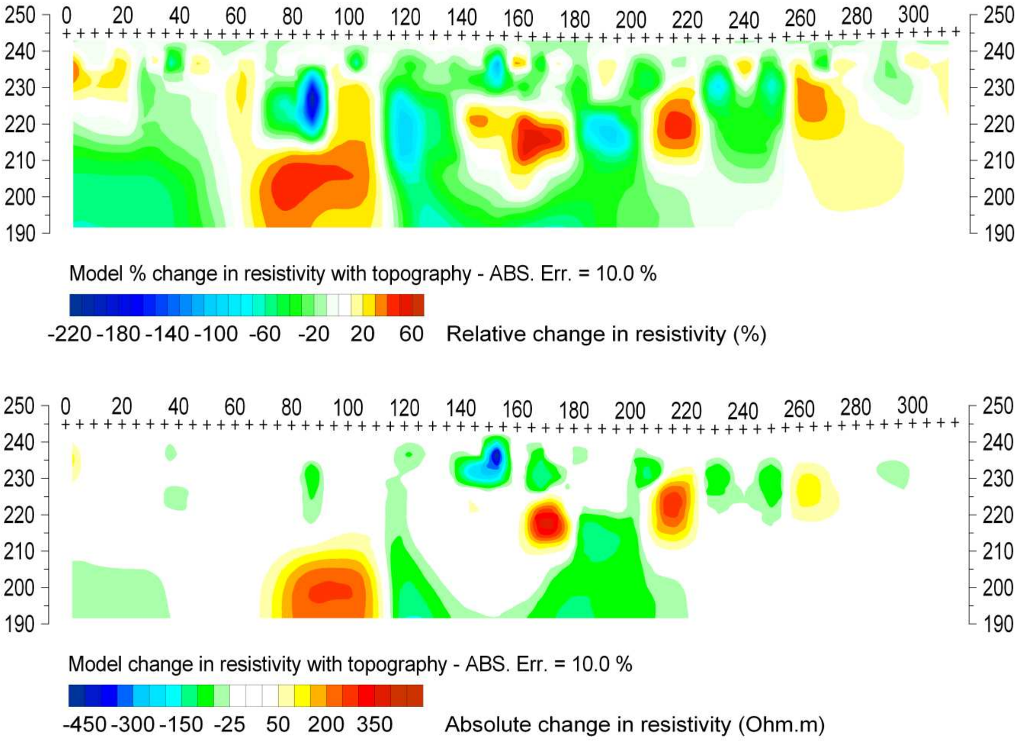

Figure 6.9: The time-lapse changes in resistivity for the Evelette F5 monitoring line present an erratic distribution with values ranging between -450 and 450 Ω.m (bottom) corresponding to percentage changes ranging between -220 and 70% (top). These images cannot be interpreted physically because of the presence of strong artifacts. Moreover, we expected more diffuse changes given all the a priori information we had about seasonal fluctuations of the water table. In our working scale, it seems that ERT is unable to image changes of hydraulic gradients, or a preferential flow through fractures. For this reason, we decided to force changes in resistivity to image the latter (section 6.2).

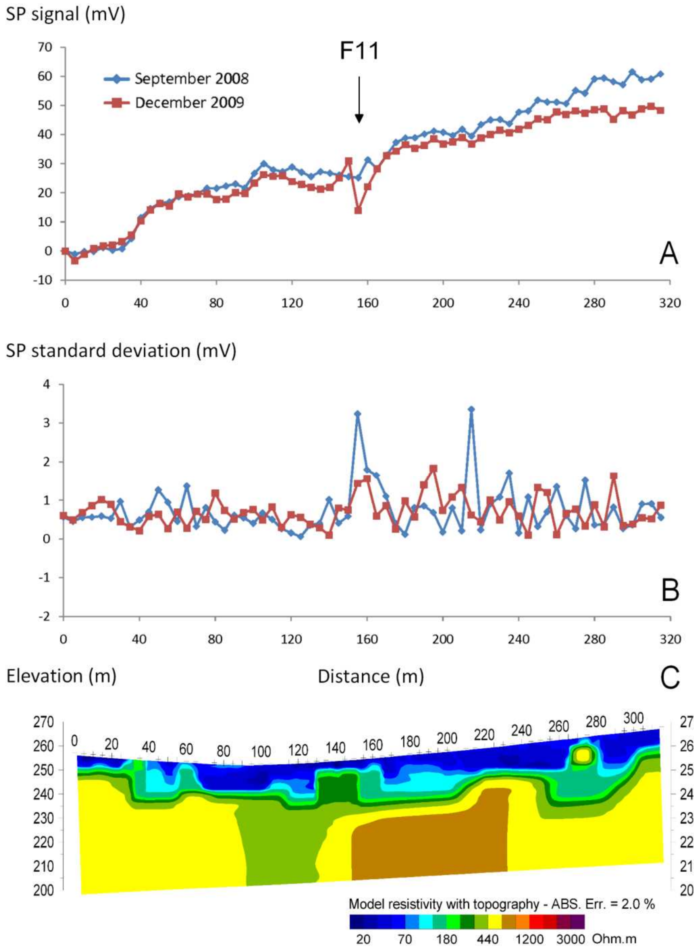

Figure 6.10: The electrical resistivity distribution of the Havelange (F11) monitoring line (C) presents two different homogeneous layers. The first one – 5 to 20 m thick – is related to the conductive (20 to 80 Ω.m) overburden (clay loam) or the weathered limestone bedrock. The saturated limestone bedrock presents values between 100 and 620 Ω.m indicating fractured (or at least not compact) limestones. We measured the SP signal twice – in September 2008 and in December 2009 – with the same fixed base position (0 m). The SP signal (A) presents a higher gradient in September 2008 (0.173 mV/m) than in December 2009 (0.140 mV/m). This conclusion is comforted by the fact that the SP standard deviation value remained constant between both acquisitions (B). Moreover, we measured the water table depth at 7.39 m and 11.27 m below surface – in September 2008 and December 2009, respectively – in the F11 piezometer situated at a distance of 155 m. The hypothesis related to a stronger hydraulic gradient in high groundwater level periods seems valid.

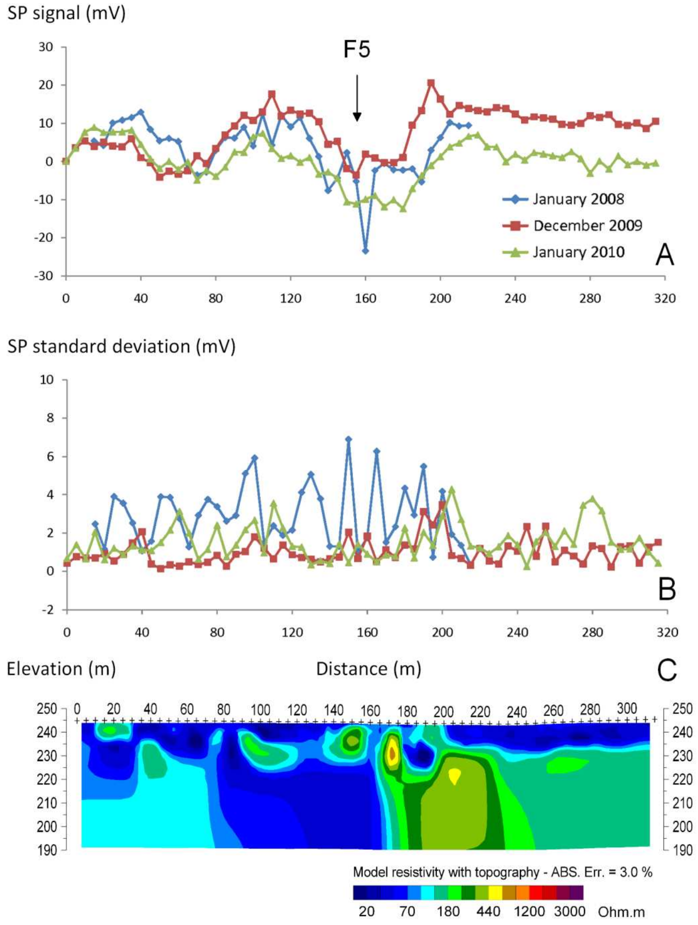

Figure 6.11: The electrical resistivity distribution of the Evelette (F5) monitoring line (C) presents two different behaviors. From the start of the profile to the distance of 170 m, the overburden (clay loam and sand) and the weathered/fractured/karstified limestone bedrock present resistivity values between 20 and 80 Ω.m. After 170 m, the overburden – 10 m thick – can be discriminated from the limestone bedrock that seems to be highly fractured/karstified given the range of inverted resistivity values (120 to 440 Ω.m). We measured the SP signal three times – in January 2008, December 2009, and January 2010 – with the same fixed base position (0 m). The SP profiles (A) present the same flat signal with a strong negative anomaly centered near the piezometer position in all three periods. The SP standard deviation value remained constant between the two last profiles (B). However, the SP signal of January 2008 presents a higher noise level. We measured the water table depth at 12.46 m and 12.50 m below surface – in December 2009 and January 2010, respectively – in the F5 piezometer situated at a distance of 155 m. We were not able to measure it in January 2008 since the piezometer did not exist yet. Here, the hypothesis of a horizontal water table distribution seems valid.

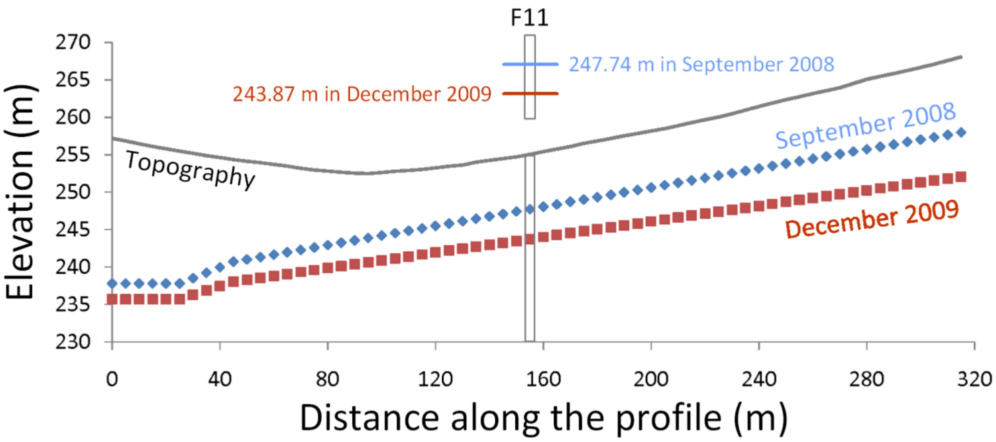

Figure 6.12: If we assume a constant value of the electrokinetic apparent coupling coefficient over time, we can image a raw distribution of the water table elevation from the different SP signals – September 2008 and December 2009 – using the water table model. To do this, a hydraulic head measurement from both periods is mandatory since the SP signal is only related to the difference of hydraulic heads, according to the water table model. The hypothesis related to a stronger hydraulic gradient – related here to the southern flank of the Havelange calcareous valley – in high groundwater level periods and in contrary, a lower hydraulic gradient in low groundwater level periods seems valid. We used here a value of 2.7 mV/m for the apparent coupling coefficient (see Robert et al., 2011). Even if this value is only a gross estimation of the true apparent coupling coefficient, the ability of the SP method to image changes in the hydraulic gradients is demonstrated.

References

Fournier, C., 1989, *Spontaneous potentials and resistivity surveys applied to hydrogeology in a volcanic area: case history of the Chaîne des Puys (Puy-de-Dôme, France)*, Geophysical Prospecting, 37 (6), 647-668.

Revil, A., V. Naudet, J. Nouzaret, and M. Pessel, 2003, *Principles of electrography applied to self-potential electrokinetic sources and hydrogeological applications*, Water Resources Research, 39 (5), 1114, doi:10.1029/2001WR000916.

Robert, T., A. Dassargues, S. Brouyère, O. Kaufmann, V. Hallet, and F. Nguyen, 2011, *Assessing the contribution of electrical resistivity tomography (ERT) and self-potential (SP) methods for a water well drilling program in fractured/karstified limestones*, Journal of Applied Geophysics, 75 (1), 42-53.

6.2. A salt tracer test monitored with surface ERT

We saw in the previous section that a surface ERT monitoring was not efficient to study seasonal variations of the dynamics of groundwater flow, especially at our working scale and for our investigated sites (calcareous valleys of the Dinant Synclinorium) as well as to highlight preferential flow paths through fractures. To solve the latter problem, we decided to force a change in the bulk electrical resistivity that can be measured with ERT and imaged by time-lapse ERT inversion.

We injected a salt tracer solution in the F11 piezometer of the Havelange calcareous valley to decrease the groundwater electrical resistivity (and consequently, the bulk electrical resistivity) and we monitored its propagation with surface ERT. This methodology is particularly difficult to use in complex fractured systems such as the ones investigated in this work. This is even more challenging because we only used surface ERT that possess a lower resolution than crosshole ERT. However, with strong precautions in the experiment set up, in the data acquisition, and in the time-lapse inversion, we were able to image the salt tracer transport in the Havelange calcareous syncline.

The results of this section are presented in Robert et al. (2012), a scientific paper published in Geophysics, 77 (2), B55-B67. Earlier versions of this section were also presented at EGU 2010, in Vienna, Austria, at Near Surface 2010, in Zurich, Switzerland, and at GELMON 2011, Vienna, Austria.

6.3. Groundwater flow direction from an SP map

In the previous section, we were able to estimate the local groundwater flow direction in the vicinity of the F11 piezometer in the Havelange calcareous valley. To do this, we monitored a salt tracer test with surface ERT and the local flow direction was estimated to approximately N10°E. In this brief section, we present the results of an SP mapping survey designed to identify the local hydraulic gradients of the southern flank of the calcareous valley, in the vicinity of the F11 piezometer. This study was realized in the framework of an applied geophysics course in 2008 and we would like to acknowledge students of the YEG group for providing us this data set.

We conducted this SP survey in the Havelange calcareous valley in November 2008. We centered the SP mapping on the F11 piezometer and the fixed base position corresponds to the first SP station of the first profile (Figure 6.13). We took two measurements for each of the 125 SP stations distributed on 6 parallel profiles. The SP error – the standard deviation of the SP measurements at a given station – distribution (Figure 6.13) shows a low noise level with all values below 2.7 mV. Therefore, we can have a good confidence in the resulting SP map since SP values range between -12 and 12 mV.

To obtain the SP map, we used ordinary kriging. To do so, we modeled the experimental variogram (Figure 6.13) with a nugget effect of 7.2 mV and a linear slope of 0.42. The resulting map is presented in Figure 6.13. It shows a strong gradient from south to north which, interpreted in terms of groundwater flow, corresponds to the combination of the two perpendicular hydraulic gradients of this calcareous syncline (see section 4.3). The groundwater flow direction estimated from the salt tracer test – N10°E – is then confirmed by the results of this SP mapping. A strong SP anomaly is also present in the immediate vicinity of the well. It was already present in the SP profile taken in September 2008 (Robert et al., 2011; section 5.3) and this is another proof of the reproducibility of SP measurements.

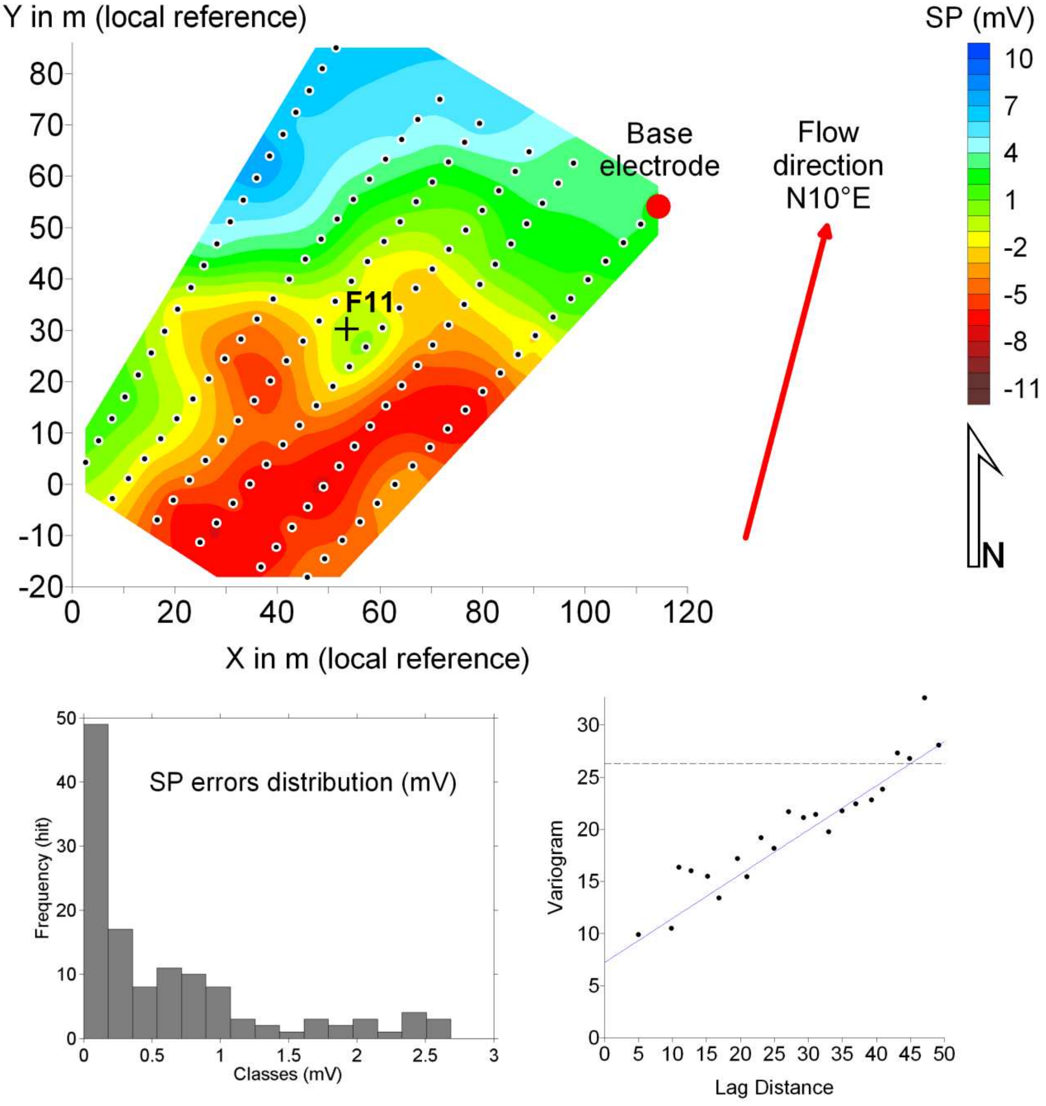

Figure 6.13: This SP map (top) centered on the F11 piezometer presents a strong gradient in a direction of about N10°E. This direction corresponds to the local groundwater flow direction that we estimated with the salt tracer test experiment. This map was obtained by kriging the values of the different SP stations (black dots) using a linear variogram with a slope of 0.42 and a nugget effect of 7.2 mV (bottom right). The distribution of the SP errors (bottom left) shows that all errors are below 2.7 mV. Therefore, we can have a good confidence in the SP map.

6.4. Time-lapse noise characterization and comparison of different time-lapse strategies

In the previous section, we demonstrated the ability of surface ERT to monitor a salt tracer test in a fractured limestone aquifer at a scale relevant for real-world applications. We also showed that noise reduction was essential when conducting time-lapse measurements because the percentage of changes measured in the data (electrical resistances) may be small compared to the noise level. Assuming that strong precautions were made during the data acquisition, the question of noise characterization is also crucial. This was already true for static electrical images (see section 2.3) but it is even more appropriate in time-lapse inversion. Indeed, selecting a too safe noise assumption will not let the data set speaks entirely and the desired changes in resistivity might not be modeled and the dynamics of the system missed. In contrary, an underestimation of the noise level could lead to the presence of strong artifacts that might mask the subsurface process that is monitored or even worse, induce wrong interpretation on the hydrodynamics.

Here, we will address the issue of time-lapse noise characterization using the first transversal profile (P1) of the second tracer test of Robert et al. (2012) presented in section 6.2. Then, we will compare several time-lapse inversion schemes, namely independent, cascaded, or data difference inversions (see section 2.4.5) and the influence of several noise assumptions on the final results. An earlier version of this work was partly presented during the 1st International Workshop on Geoelectrical Monitoring – GELMON 2011 – held at the Geological Survey of Austria in Vienna (Nguyen et al., 2011). Finally, we will present results related to the use of specific model constraints including the minimum-gradient-support or an extra time-domain model constraint.

All inversions shown here were performed with the code CRTOMO (Kemna, 2000) which was detailed in section 2.

6.4.1. Background resistivity model

The background resistivity of profile P1 (see section 6.3) presented in Figure 6.14, presents two different layers as discussed in the previous section. The first one is composed of electrically conductive clay loam, up to 80 Ω.m, that compose the 5 to 10 m thick overburden and the weathered part of the limestone bedrock. The second layer presents higher resistivity values, from 100 up to 320 Ω.m that are related to the saturated and fractured limestone bedrock. We measured the water table at the depth of 11.38 m during all the experiment.

This background model will be used as a reference for further time-lapse inversions. It is therefore important to investigate the static – in opposition to ‘‘time-lapse’’ – reciprocal errors. We collected reciprocal measurements for this background data set and the estimated errors using reciprocals are plotted versus the mean transfer resistances in Figure 6.15. We used an error model equal to 1 mΩ (a) and 2% (b) to obtain the background model and further inverted models using, or related to, this background model in order to make quantitative comparisons. With this error model, we encompass almost all errors although it might be considered as too secure.

We collected reciprocal measurements for three background data sets, one for each of the three days of the salt tracer experiment (Robert et al., 2012), a scatter plot of normal and reciprocal resistances for these days are shown in Figure 6.16. The correlation between the normal and reciprocal data is nearly perfect and does not vary over time, which indicates that the static error is constant over time. The choice of using the same error model which is equal to 1 mΩ (a) and 2% (b) for all time-lapse images related to the background model is then validated.

We estimated the propagation of “static” noise in time-lapse results by inverting two different background data sets using independent inversions, as we did in Robert et al. (2012); section 6.2. Independent inversions of time-lapse data sets generally give the highest error percentage, the obtained changes will then allow us to select a cutoff for non-significant percentage changes. Figure 6.17 shows that the percentage change in resistivity between both backgrounds ranges between -2.5 and 2.5%. We can therefore consider this interval as non-significant in terms of changes in resistivity. This is reflected in the color scale of the time-lapse images presented in this section.

6.4.2. Time-lapse data error characterization

Data difference inversion uses the difference of resistances ($d - d_0$) measured at different times and not the resistances (d) themselves (see section 2.4.5). As a result, the error estimation for data error should also be adapted to this difference. To our knowledge, there are few to no references on how to proceed. In analogy to the procedure used for static error characterization, we analyzed the time-lapse reciprocal error, $\Delta \log R_N - \Delta \log R_R$. The scatterplot between $\Delta \log R_N$ and $\Delta \log R_R$, presented in Figure 6.18, shows a similar 1:1 trend as the static scatterplot of Figure 6.16, except that the resistance cloud is much more diffuse around this trend. The distribution of the time-lapse reciprocal errors is Gaussian and all errors are below 0.01 (Figure 6.18).

The approach of LaBrecque et al. (1996) and Slater et al. (2000) concerning static noise characterization states that the data error is a function of the measured resistance. This was validated by field or laboratory data (see Figure 6.15 for an example) but never checked for time-lapse data. The time-lapse reciprocal error versus the mean difference of the measured resistances plot (Figure 6.19), which is the *inverted* data, shows no clear correlation. However, the plot of the time-lapse reciprocal error versus the mean transfer resistance (Figure 6.19), which is the *measured* data, shows that the time-lapse error, as estimated by reciprocal measurements, is dependent of the measured resistance. In our case, the dependence is minimal since only a few percent of errors present higher values, and using a constant error model have little influence on the final results. However, in Nguyen et al. (2011), we showed that some cases require quantifying and taking into account this relationship in order to obtain exploitable results.

6.4.3. Time-lapse inversion results using resistances as data

We first compared several independent inversions in Figure 6.20 computed using a constant error model of $|e| = 2\% \mathrm{R} + 10^{-3}$; see Eq. (2.5). Time-lapse images from the six time-series are presented in the same chronological order than in Robert et al. (2012); section 6.2, that is 1 ½, 3, 4 ½, 6 ½, 8, and 10 hours after the beginning of the injection of a 4 hours long pulse of salt tracer. We compared the independent inversion (A) with the cascaded approach (B) but none of these methodologies gave us a focused time-lapse change as it is expected (Robert et al., 2012). Moreover, both schemes led to images that are difficult to interpret physically. Applying smoothing on the spatial changes did not help either (C). However, adding a time-domain model constraint (see section 2.4.5) with a high velocity assumption ($\mathrm{v} = 0.5$) led to a focused anomaly in agreement with a preferential flow path, but it is not located as it was obtained in Robert et al. (2012), where the location was 70 m along the profile (in agreement with the local flow direction estimated from an SP map, see section 6.3) instead of 100 m here. Changing the high velocity assumption and using a value for v = 0.1 in Eq. (2.31) (section 2.4.5) leads to the results presented in Figure 6.21. A wrong assumption about the "velocity" can remove all time-lapse changes and strong precautions should then be taken when no prior information on the hydrodynamics is present. A parametric study on the velocity coefficient could be performed to assess its robustness.

Figure 6.22 shows that slightly decreasing the relative error model parameter from 2 to 1.5% allowed us to retrieve a focused anomaly with independent inversions. In this case, the preferential path is located at a distance of 70 m instead of 100 m, which is more in agreement with the local flow direction (sections 6.2 and 6.3). This proves that noise characterization is primordial in time-lapse inversion and may supplant the choice of the model constraint or of the inversion scheme, especially with independent or cascaded inversions.

We also see in Figure 6.22 (left panel, last time-lapse image at the bottom) that this error model is not suited for every time-lapse data set since the last time-lapse image presents lots of artifacts. Therefore, it might be useful to use different error models when the noise level fluctuates over time (Nguyen et al., 2011) although that would hinder a quantitative interpretation.

6.4.4. Time-lapse inversion results using resistances differences as data

Fitting the data difference to about two times the standard deviation (~0.01) observed in Figure 6.18 brings obvious and numerous artifacts in the resulting image (Figure 6.23). However, the preferential path is present but masked by strong artifacts.

Using data difference inversions with a standard deviation value of 0.25 to weight the data (Eq. 2.13), we retrieved directly a focused anomaly at the correct position which is around 70 m along the profile (Figure 6.24). The application of smoothing on the spatial changes (Figure 6.24, left panel) highlights the same preferential path but removes efficiently artifacts. However, this comes at the expense of a smoother area which is not present in all time frames.

We then tried to find by trial and error a good compromise in terms of error levels between a lower amount of artifacts and the best delineation of the preferential path, supposing that the latter was focused in space. Taking a standard deviation value 5 times lower (0.05) than the one used for Figure 6.24 resulted in a sharper delineation of the preferential path but also introduced some artifacts, although mainly located in deeper areas and therefore easily identifiable (Figure 6.25). Applying smoothing on the spatial changes or using a time-domain model constraint with a high velocity assumption remove the main artifacts and preserve the sharpness of the tracer path. However, there is a strong difference in terms of imaging between the two regularization approaches in terms of magnitude and spatial imprint of the tracer. The data difference with the smoothing of spatial changes leads to the larger imprint, whereas the spatio-temporal regularization produces changes with smaller magnitudes (~5% instead of ~10%) and a more focused area.

As a perspective, we used the minimum-gradient-support approach (Eq. 2.18) to invert the data differences (Figure 6.26) in order to produce focused changes. We used two different β values, 0.001 in A and 0.005 in B and C. With the smaller β value, the resulting image presents artifacts that could be explained by the fact that for very low β, the MGS approach is less stable (Blaschek et al., 2008). However, with an “appropriate” value of β which was obtained by trials and errors, we have a time-lapse image presenting almost no artifact. Using a vertical anisotropy (a ratio of 1/5) in addition to the MGS approach (C) allowed us to find a preferential flow that is more in agreement with the geological information (subvertical fractures).

The conclusion of this section is that the best improvement, or the most impacting factor, in the resulting time-lapse images is obtained by correctly estimating the noise level. This should be based on an analysis of the static or time-lapse reciprocal errors. This is especially important for independent and cascaded inversions since wrong noise assumptions led to images that were not physically realistic with the monitored process. It is therefore essential, given the results shown here, as well as the ones from Miller et al. (2008), to systematically collect reciprocal measurements (or a subset of them) in order to have a solid basis for noise characterization and estimation. Further improvements brought by regularization should always be taken with care and come in a second step, since the a priori information rendered in the objective function should reflect the physical process under study. To find information on the latter is a challenging task. Further studies should focus on a more detailed and systematic analysis of the data error level (using data difference) versus constraints imposition (using regularization) in time-lapse inversion, using field data with ground-truth validation and/or numerical benchmarks.

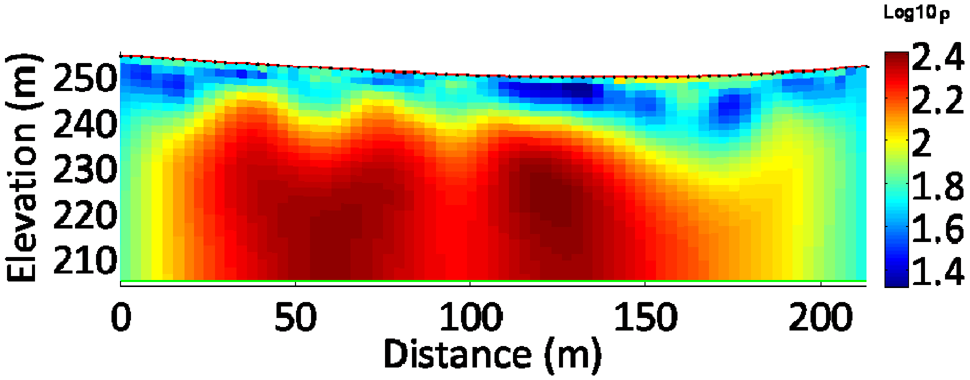

Figure 6.14: The background resistivity of profile P1 (see section 6.3) presents two layers. The first layer is composed of electrically conductive clay loam, up to 80 Ω.m, that compose the 5 to 10 m thick overburden and the weathered part of the limestone bedrock. The second layer presents higher resistivity values, from 100 up to 320 Ω.m, that are related with the saturated and fractured limestone bedrock. Note that the water table is assumed to be at a depth of 10 to 12 m. We used an error model equal to 1 mΩ (a) and 2% (b) to obtain this reference model that will be used hereafter. This error model is presented in Figure 6.15.

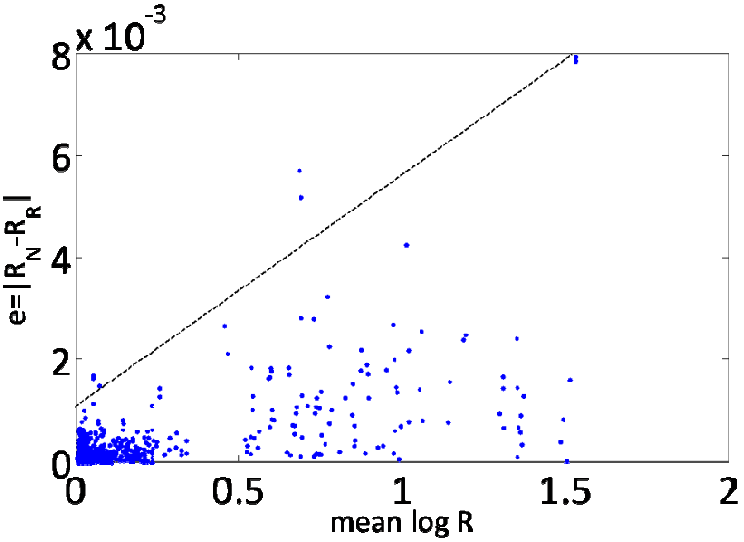

Figure 6.15: We used an error model equal to 1 mΩ (a) and 2% (b) to obtain the static electrical image that will be used as a reference model for all time-lapse inversions. With this error model, we wanted to stand in the side of safety, at this stage.

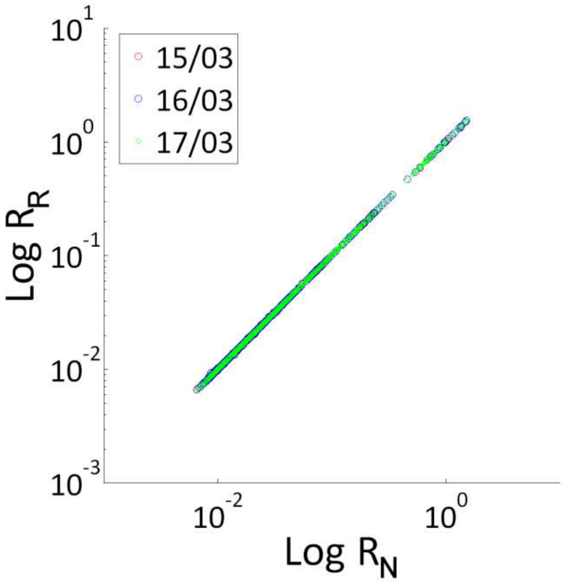

Figure 6.16: The static error seems to be constant over time since the scatterplot of normal and reciprocal resistances (in their logarithmic form) follows the same trend. For this reason, we used the same error model which is equal to 1 mΩ (a) and 2% (b) for almost all time-lapse images that are presented hereafter.

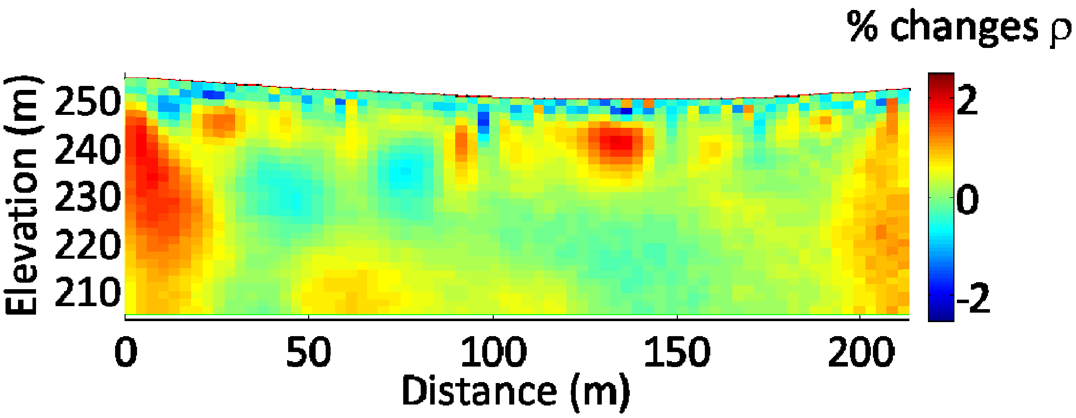

Figure 6.17: We estimated the noise propagation in time-lapse results by inverting two different background data sets using independent inversions. Indeed, the latter scheme generally gives the highest error percentage and we wanted to stand again in the side of safety. This image presents the percentage change in resistivity between both backgrounds ranging between -2.5 and 2.5%. We therefore considered this interval as non-significant in terms of changes in resistivity. We used the same error model which is equal to 1 mΩ (a) and 2% (b) for both inversions.

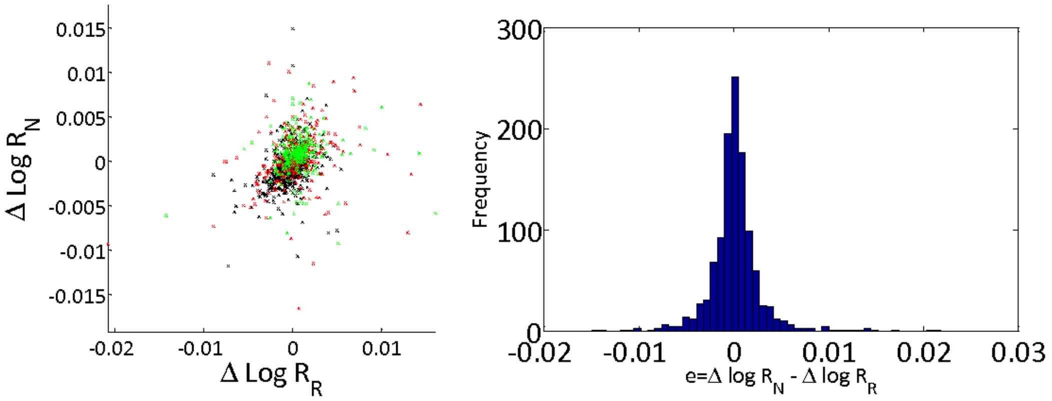

Figure 6.18: Static error models may not be appropriate in data difference inversions since the data set is the difference of resistances measured at different times and not the resistances themselves (possibly in the logarithmic form). Therefore, we investigated the time-lapse reciprocal error which is equal to $\Delta logR_N - \Delta logR_R$. The scatterplot between $\Delta logR_N$ and $\Delta logR_R$ shows a similar trend than the static scatterplot of Figure 6.16, except that the resistance cloud is more diffuse around this trend. The distribution of the time-lapse reciprocal errors is Gaussian and all errors are below 0.01.

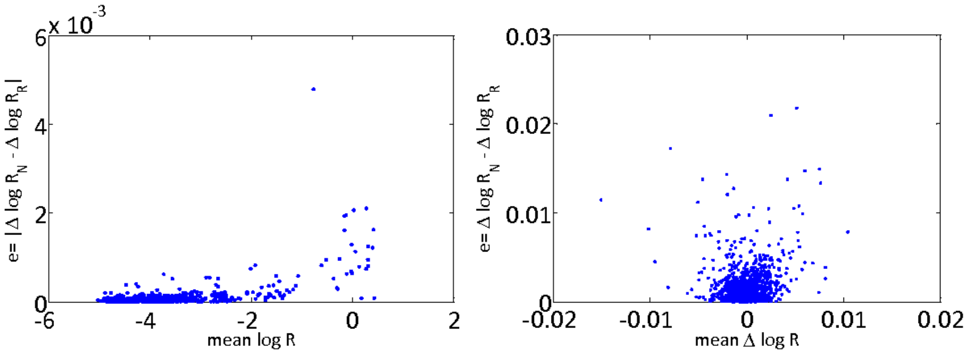

Figure 6.19: The approach of LaBrecque et al. (1996) and Slater et al. (2000) states that the data error is a function of the measured resistance, and this was validated by field observations. If we transpose this in a time-lapse framework, do we have the same kind of relationship between the time-lapse data error and the mean difference of the measured resistance? From the right panel, it seems that we do not, and one explanation could be that the actual measurement is the electrical resistance and not the data difference. In the left panel, we demonstrate by field data that the time-lapse error should be taken as a function of the measured resistance and not of the mean difference of the measured resistance. Here, the dependence is minimal since only a few percent of errors presents higher values but in Nguyen et al. (2011), we showed that in some cases, not taking this relationship into account leads to a strong misinterpretation of the process we monitored.

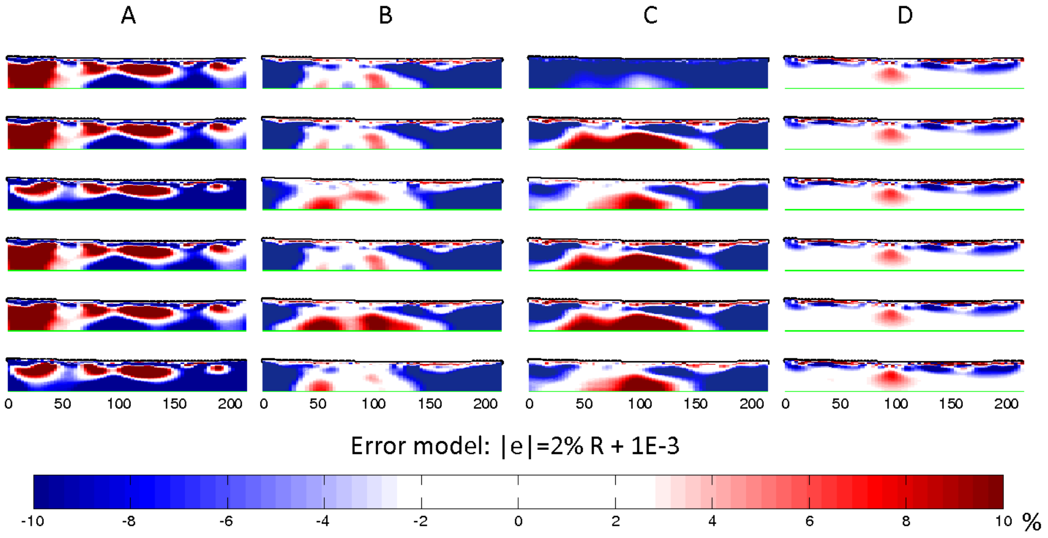

Figure 6.20: We compare here several independent inversions that are presented in the same chronological order as in Robert et al. (2012); section 6.2. We used no starting model in A whereas we used the background image as a starting model in B (the cascaded approach). Both schemes led here to images that are difficult to interpret physically since we expected a focused anomaly. Applying smoothing on the spatial changes did not help neither (C), but adding a time-domain model constraint (see section 2.4.5) with a high velocity assumption (v = 0.5) led to a focused anomaly in agreement with a preferential flow path. Note that we blanked the non-significant interval, from -2.5 to 2.5% change in resistivity.

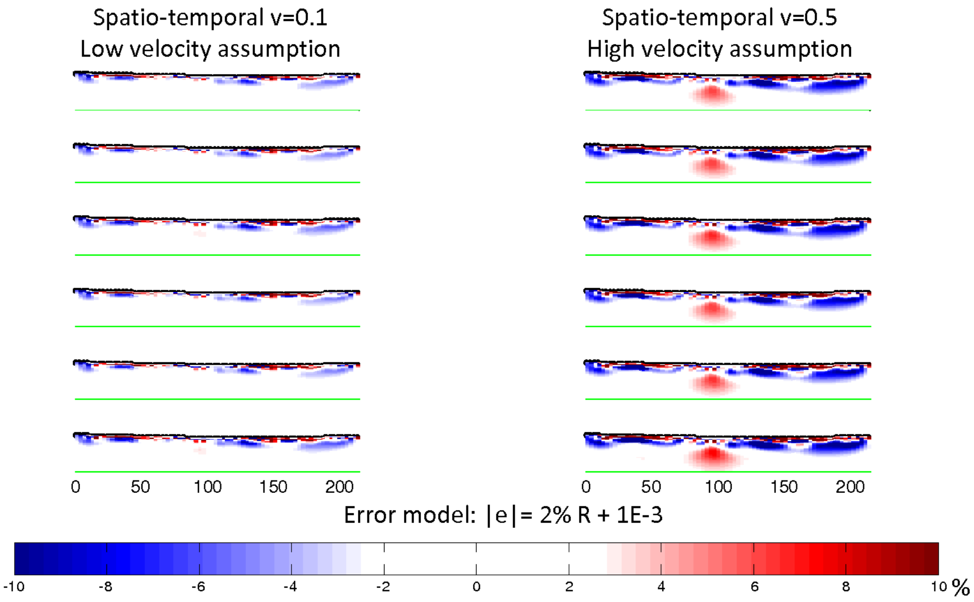

Spatio-temporal v=0.1
Low velocity assumption

Spatio-temporal v=0.5
High velocity assumption

Error model: |e|= 2% R + 1E-3

Figure 6.21: In the previous figure, we showed that a spatio-temporal model constraint helped to retrieve a focused anomaly. However, the time constraint should be used carefully because the choice of the “velocity” parameter strongly affects the results. As an example, a low velocity assumption led to almost no changes in the time-lapse images whereas a higher velocity assumption which is more in agreement with the monitored process, led to changes that are spatially focused around 100 m along the profile. We could be tempted to stop our investigations here since we found a preferential flow path. However, we did not address the issue concerning noise characterization yet, nor did we present results of data difference inversions.

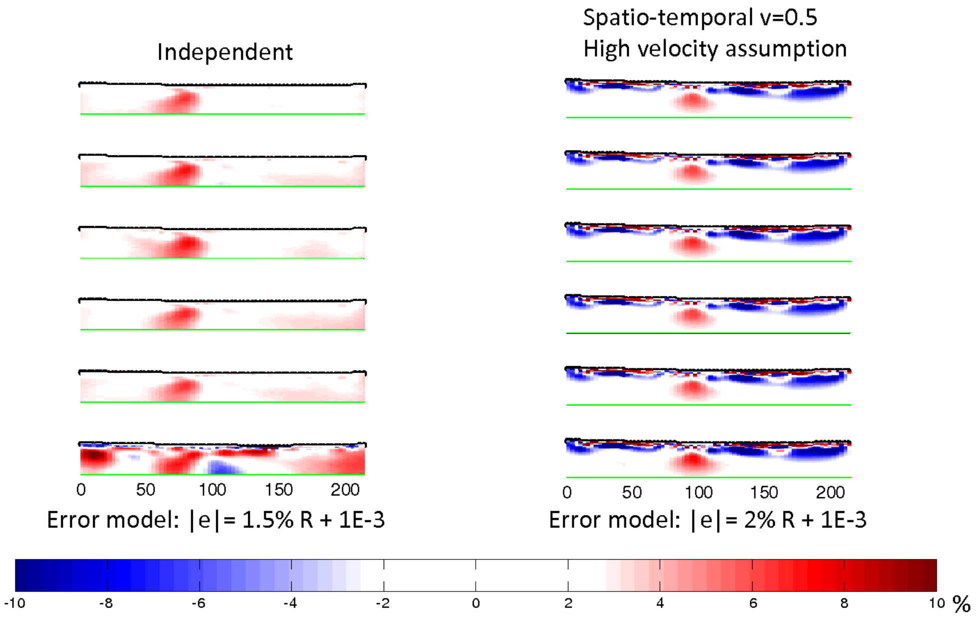

Figure 6.22: We used until now the same error model |e| = 2% R + 1E-3 and we obtained a focused anomaly only by using a spatio-temporal constraint with a high velocity assumption (right panel). Slightly decreasing the relative error model parameter from 2 to 1.5% allows the inversion process to exploit the data set thoroughly. The left panel shows that slightly decreasing the error model allows to retrieve a focused anomaly with simply independent inversions. In this case, the preferential path is located at a distance of 70 m instead of 100 m, which is more in agreement with the local flow direction (sections 6.2 and 6.3). This proves that noise characterization is primordial in time-lapse inversion and supplants the choice of the model constraint or of the inversion scheme. Note that this error model is not suited for the last time-lapse data set because of the presence of artifacts in the last time-lapse image.

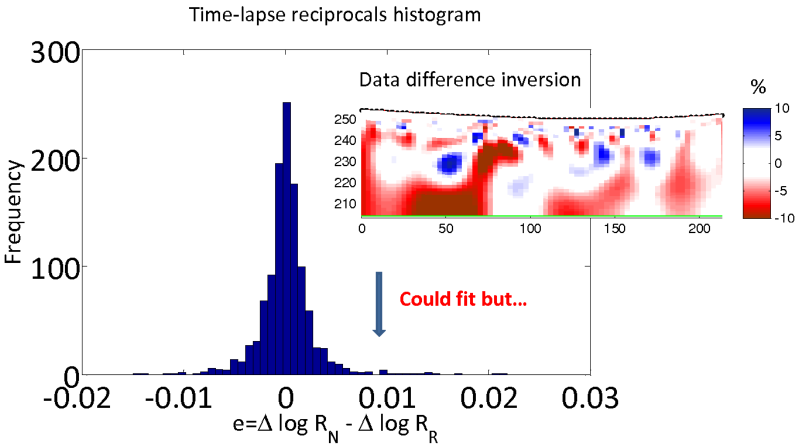

Figure 6.23: An example of overfitting is presented here, still for a data difference inversion. We saw that time-lapse reciprocal errors are constrained between -0.01 and 0.01. We were able to fit this noise level but the preferential path which is nevertheless present in the resulting image is masked by strong artifacts. Noise characterization does not necessarily imply the calculation of time-lapse reciprocals. One needs to use these time-lapse reciprocals to try different error models, to find the appropriate one.

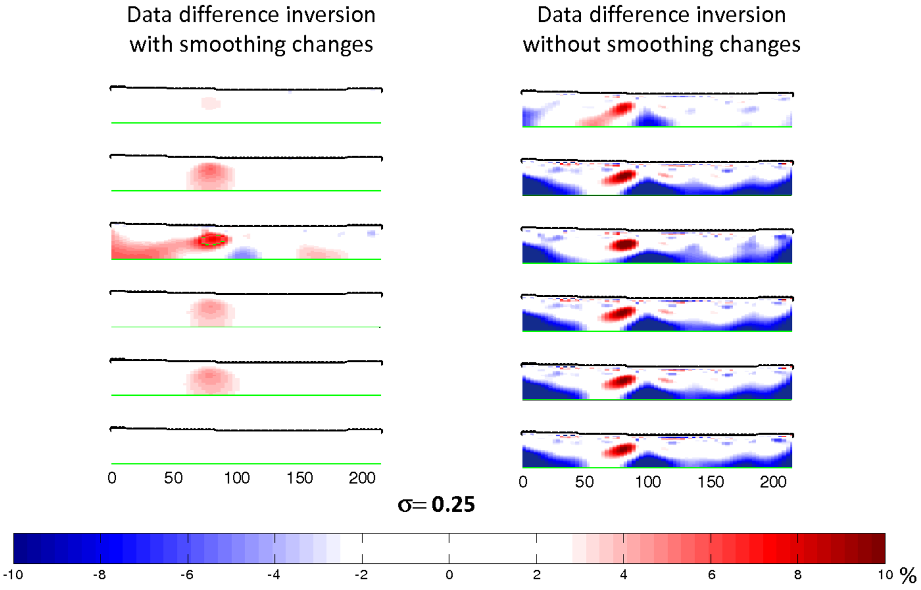

Figure 6.24: With data difference inversions, we retrieved directly a focused anomaly at the correct position which is around 70 m along the profile. The application of smoothing on the spatial changes also helps to highlight the preferential path. Here, we used a standard deviation value of 0.25 to weight the data.

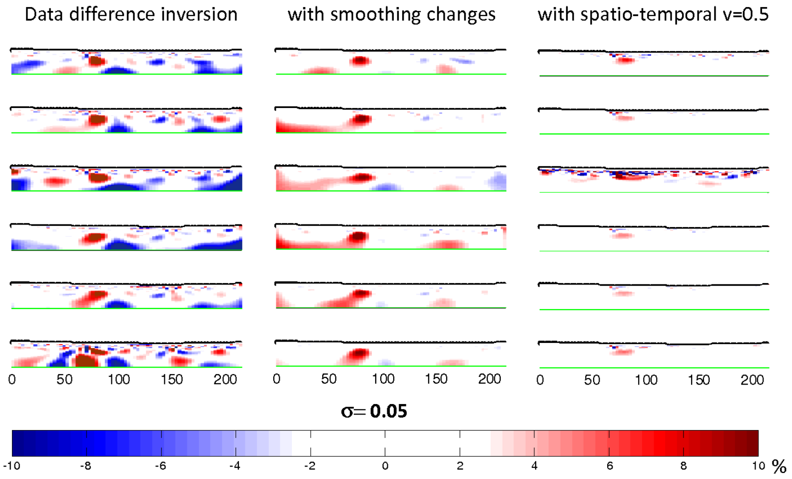

Figure 6.25: Taking a standard deviation value 5 times lower than the one used for Figure 6.24 does not, in this case, improve the resulting images with simple data difference inversion. Moreover, it seems that more artifacts are present. Here, applying smoothing on the spatial changes or using a time-domain model constraint with a high velocity assumption helps to remove these artifacts.

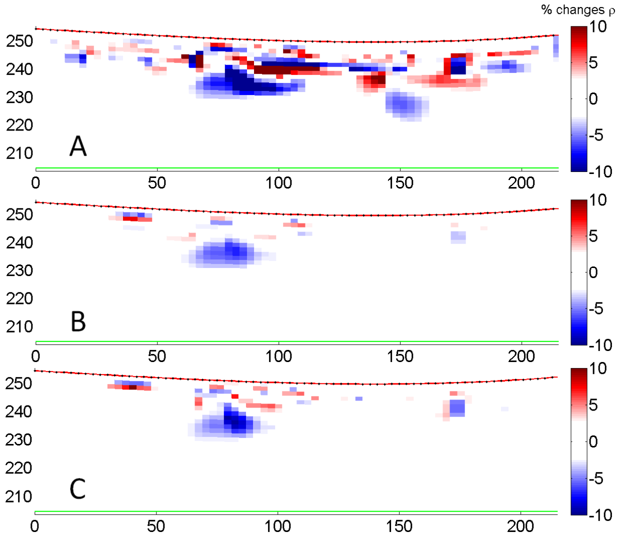

Figure 6.26: As a perspective, we used the minimum-gradient-support approach to invert the data differences. We used two different β, 0.001 in A and 0.005 in B and C. With a too small β, the resulting image presents artifacts that could be explained by the fact that for very low β, the MGS approach is less stable (Blaschek et al., 2008). However, with the appropriate value of β, we obtained a time-lapse image presenting almost no artifact. Using a vertical anisotropy (a ratio of 1/5) in addition to the MGS approach (C) allows to find a preferential flow that is more in agreement with the geological information (subvertical fractures).

References

Blaschek, R., A. Hordt, and A. Kemna, 2008, *A new sensitivity-control led focusing regularization scheme for the inversion of induced polarization data based on the minimum gradient support*, Geophysics, 73 (2), F45-F54.

Kemna, A., 2000, *Tomographic inversion of complex resistivity : theory and application*. PhD Thesis, University of Bochum.

LaBrecque, D. J., M. Miletto, W. Daily, A. Ramirez, and E. Owen, 1996, *The effects of noise on Occam's inversion of resistivity tomography data*, Geophysics, 61 (2), 538-548.

Miller, C. R., P. S. Routh, T. R. Brosten, and J. P. McNamara, 2008, *Application of time-lapse ERT imaging to watershed characterization*, Geophysics, 73 (3), G7-G17.

Nguyen, F., A. Kemna, T. Robert, T. Hermans, D. Caterina, and A. Flores-Orozco, 2011, *Inversion of multi-temporal geoelectrical data sets: insights from several case studies*, GELMON 2011, 1st International Workshop on Geoelectrical Monitoring, Vienna, Austria, December 1, 2011.

Robert, T., D. Caterina, J. Deceuster, O. Kaufmann, and F. Nguyen, 2012, *A salt tracer test monitored with surface ERT to detect preferential flow and transport paths in fractured/karstified limestones*, Geophysics, 77 (2), B55-B67.

Slater, L., A. M. Binley, W. Daily, and R. Johnson, 2000, *Cross-hole electrical imaging of a controlled saline tracer injection*, Journal of Applied Geophysics, 44 (2-3), 85-102.

7. Modeling flow

Developing a conceptual model for groundwater flow requires knowledge on the distribution of geological materials and their hydraulic properties. The identification of spatial structures in the subsurface, such as fractured zones or dissolution zones leading to preferential flow paths, is even more critical in developing a reliable conceptual model (e.g., Berkowitz, 2002; Eaton, 2006; Eaton et al., 2007; Graf and Therrien, 2007; 2008). It is also much more challenging.

Fracture information generally comes from geological observations on outcrops and from boreholes (e.g., Hancock, 1985; Lemieux et al., 2006; 2009), from the interpretation of hydraulic tests (e.g., Le Borgne et al., 2004; 2006a; 2006b; Illman and Tartakovsky, 2006; Hao et al., 2008; Blessent et al., 2011), or from geophysical surveys (e.g., Day-Lewis et al., 2003; Krishnamurthy et al., 2003; Porsani et al., 2005; Rozycki et al., 2006; Vasconcelos and Grechka, 2007; Yadav and Singh, 2007; Suski et al., 2008; Wishart et al., 2006; 2008; 2009; Dorn et al., 2011; Robert et al., 2011; 2012).

Geophysical methods have been widely used to map the subsurface distribution of geological materials but recent developments in geophysics, such as the increased use of joint inversion of geophysical and hydrogeological data, may further allow quantifying the hydraulic conductivity of geological materials (e.g., Titov et al., 2005; Jardani et al., 2007; Straface et al., 2007; Bolève et al., 2009; Jardani and Revil, 2009).

The objective of this section is to demonstrate that electrical resistivity tomography (ERT) and self-potential (SP) methods can improve both the conceptual model developed for groundwater flow systems and the calibration of the corresponding groundwater flow model. The use of the two geophysical methods, combined with a groundwater flow model, is presented for the Havelange fractured limestone aquifer. Earlier versions of this section were presented at the 2nd International HydroGeoSphere User Conference, in Hanover, Germany in 2011, at Near Surface 2011, in Leicester, United Kingdom, and at ModelCare 2011, in Leipzig, Germany.

7.1. Model conceptualization

The Havelange calcareous valley is situated in the Namur and Liège Provinces of Belgium, between the town of Havelange and the villages of Petit-Avin and Les Avins where the Hoyoux River cuts the valley (Figure 7.1). The rolling topography of the area results from a succession of calcareous valleys (synclines) and sandstones crests (anticlines). These calcareous synclines form aquifers that are very complex since they are highly fractured and even karstified (see sections 4 and 5.2) and the Havelange valley is no exception to this rule.

Given our working scale and the scale of the fractured zones retrieved in the Mercier quarry (see section 5.2), we decided to use equivalent porous media to model groundwater flow in this calcareous valley.

One critical issue with this region is the scarcity of available geological and hydrogeological data. This lack of useable information for the model conceptualization and calibration guided our choice for the site selection, namely the Havelange syncline. A few wells are present but they are close to the Hoyoux River in the eastern part of the valley (Figure 7.1). Since the Hoyoux River imposes a base level to groundwater, these wells are not useful in terms of calibration (Figure 7.2). The new F11 piezometer is maybe the only source of typical hydrogeological data for calibration purpose.

The Havelange calcareous syncline has a width of about 800 m but once the model is extended to physical limits to account for boundary conditions, this width almost doubles. The maximum length of the Havelange calcareous valley is a little bit less than 8 km, in the direction of the geological structures (Figure 7.1).

We extended the physical limits of the model to the nearest crests that are situated north and south in the sandstones anticlines. The water table is generally shallow in these sandstones aquifers and assuming that the water divides correspond to the sandstones crests is a reliable hypothesis. We limited the model east by the Hoyoux River since it creates a transverse valley crossing all synclines and anticlines of the region.

We chose these physical limits to impose the best possible boundary conditions. North and south, we imposed a no flow boundary condition because these limits of the model correspond to water divides. Brouyère et al. (2009; 2010) used the same condition to model groundwater flow at a higher scale for the whole Dinant Synclinorium. East, along the Hoyoux

River, we imposed specified hydraulic head values – the distributed Hoyoux River water level – because the river imposes a base level to groundwater (Figure 7.3).

The lack or scarcity of geological and/or hydrogeological data is frequent when conceptualizing groundwater flow models and modelers often have to use assumptions which are guided by their experiences to build models (e.g., Berkowitz, 2002; Eaton, 2006). Here, to counterbalance the lack of geological and hydrogeological data in the valley, we performed geophysical surveys. Thus, the conceptualization of the groundwater flow model is based on the interpretation of physical properties of the subsurface.

We acquired two long roll-along ERT profile (595 m each) to identify more fractured limestones in the Havelange calcareous valley, expected to be less resistive than compact limestones given the conductive groundwater that flows in these limestones. To do so, we used 120 electrodes (24 per cable) spaced by 5 m to obtain that length. We acquired profile P1 in March 2010 and profile P2 in August 2011. Both profiles, situated near the F11 well position, are parallel and separated by 250 m.

We used an IRIS SYSCAL PRO device to obtain both data sets. We created a dipole-dipole sequence with a spacing factor limited to 6 and we optimized it for multi-channel acquisition. We used a transmitter-current-injection time window of 1 s and we performed 3 to 6 stacks with a quality factor of 1%. We also collected reciprocal measurements to estimate the true data noise level (results in section 5.4). With these parameters, we obtained a good data quality as always when using an IRIS SYSCAL PRO on this specific site. The acquisition procedure for P2 – similar of the one used for P1 – is presented in section 5.4.

Using ERT, we subdivided the syncline into zones that are more or less fractured (Figure 7.4) to which we assigned different hydraulic properties. These zones are oriented along the axis of the syncline and their width ranges between 40 and 120 m. We confirmed the existence and orientation of these more fractured areas with outcrops information of the Mercier quarry that is situated in the extension of the fractured zone A (see section 5.2). We added these three more electrically – and therefore also hydraulically – conductive zones named A, B, and C into the conceptual model of groundwater flow (Figure 7.7).

We also collected SP measurements along the profile P1 which passes on the F11 piezometer position, in September 2011. We measured three points per SP station to estimate the noise level. We spaced every SP station by 5 m, and their positions correspond to the ERT electrodes position. The base electrode is located at a distance of 320 m along the profile. The data noise level is quite low with a maximum value of around 3 mV (Figure 7.5) whereas the SP signal ranges between -10 and 60 mV (Figure 7.6).

The SP signal (Figure 7.6) decreases along the northern flank of the valley – from 0 to 70 m – and reaches a plateau in the center of the syncline – from 70 to 350 m – before increasing along the southern flank with a strong gradient. This behavior seems to be related with the hydraulic gradients related to the flanks of the syncline. Note that the SP signal was multiplied by -1, as in Robert et al. (2011) to facilitate the visual correlation between SP and hydraulic gradients. Three strong anomalies, well correlated with ERT zones A, B, and C are also present in the SP signal. These can be interpreted in terms of preferential flow paths since the electrokinetic effect is the dominant contribution of self-potentials in these calcareous valleys.

We gathered all available information to construct the conceptual model of groundwater flow (Figure 7.7). We used information from both ERT profiles as well as from the SP profile along P1 where we found three hydraulically-active fractured zones A, B, and C oriented along the direction of the syncline axis (Figure 7.8). We decided to subdivide the limestones hydrogeological unit into several zones more or less fractured to which we assigned different hydraulic properties. As an example, we assigned a higher initial hydraulic conductivity to the three A, B, and C hydraulically-active zones than the other limestones units.

7.2. Model precalibration using geophysical and hydrogeological data

Once the groundwater flow model conceptualized, we used the software Grid Builder (McLaren, 2006) to create the grid (Figure 7.9) and the code HydroGeoSphere (Therrien et al., 2005) to simulate groundwater flow. At this stage, we were only interested in permanent and saturated flow. The finite-element mesh is composed of a little bit less than 94000 tetrahedral finite-elements whose sides range between 5 to 10 m in the fractured areas and 20 to 40 m in more compact limestones units or in the sandstones units, respectively.

We used the digital terrain model (DTM) from the Walloon Region of Belgium composed of a square mesh with values every 30 m and GridBuilder to interpolate the elevation on our grid.

We also extended the grid at depth to an elevation of 160 m (Figure 7.10) which corresponds to a depth of approximately 100 m below surface.

The parameters we wanted to calibrate were the four hydraulic conductivity values for the sandstones, shales, fractured, and more compact limestones units. At this stage, we did not incorporate the overburden layer – 5 to 10 m thick – nor distinguished every fractured units or both sandstones and shales units. We also imposed the water recharge for all four units by using the values estimated in Brouyère et al. (2009), namely 20, 110, and 200 mm/year for the shales, sandstones, and limestones hydrogeological units, respectively.

We used hydraulic heads measured in wells of the Havelange calcareous valley to precalibrate the groundwater flow model. To perform the calibration, we used PEST (Doherty, 2004) that allows an automatic calibration based on a typical smoothness-constraint. Without surprise, the model prediction for the four observation points related to the wells situated near the Hoyoux River are imposed by the local boundary condition where we imposed hydraulic head values along the river (Figure 7.11). The observations in the F11 piezometer are however well predicted by the model.

We added a few observation points – one every 40 m – along the ERT and SP profile P1 in order to visualize the water table distribution predicted by the model (Figure 7.12) and then, we correlated it with the measured SP signal. The main trend (red line) corresponds well with the SP signal in the southern flank of the valley but this is not the case in the northern flank. The water table variation along this profile is also quite low with a maximum value below 1 m. Therefore, our first assumption concerning the streaming potential apparent coupling coefficient (C' = 2.7 mV/m) as previously used (sections 5.3 and 6.1) – might be underestimated.

Regarding the probable underestimation of the coupling coefficient C', we tested several values, performing this way a sensitivity analysis. We first doubled, then quadrupled our initial guess (2.7 mV/m), and better results seem to be obtained with values above 10 mV/m. This value is in agreement with Revil et al. (2003). Indeed, authors present the linear relationship existing between C' and the groundwater electrical conductivity in their Figure 3. Reporting the value of groundwater conductivity measured in piezometer F11 (about 0.06 S/m) in their Figure 3 gives us a value of about 10 mV/m.

The difficulty of measuring this apparent coupling coefficient in the field is related to the lack/scarcity of useable piezometric information. Indeed, wherever two piezometers were close enough to perform SP measurements, the difference in hydraulic heads between both wells was generally too low. This is a consequence of the fact that these piezometers were generally drilled close to water exploitation areas which are not far from the Hoyoux River. The apparent coupling coefficient should therefore be another parameter of groundwater flow model calibration in the perspective of using the full SP signal as an additional source of calibration. Indeed, its knowledge is only possible with laboratory measurements or by drilling new piezometers for this purpose. This is not possible at this stage because of the costs of these solutions.

The precalibration using both piezometric heads and the extra hydraulic heads estimated with the water table model (C’ = 10.8 mV/m) applied to the SP signal measured along P1 gave physically-realistic units. Indeed, the fractured limestones are more hydraulically-conductive than the other limestone units whereas the sandstone units present hydraulic conductivity values one order of magnitude lower than the limestone units. Finally, the shales units have very low hydraulic conductivity values as expected.

To improve our groundwater modeling results, the conceptualization of the model could incorporate the overburden. Recent works (e.g., Bolève et al., 2009) show that the full SP signal, and modeling the streaming potentials, could be used instead of the water table model. However, retrieving the space-dependent coupling coefficient might be a challenging task as discussed above.

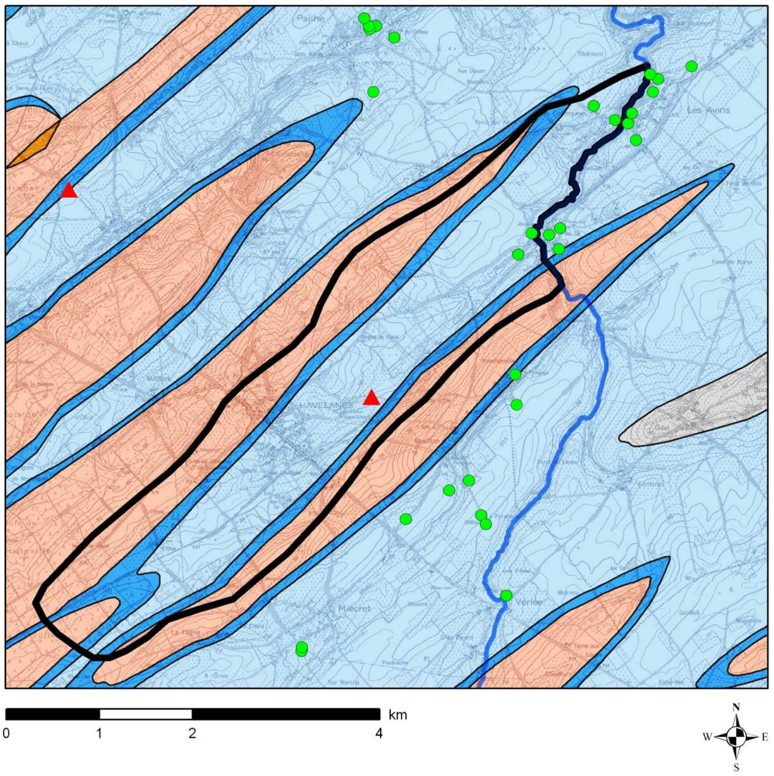

Figure 7.1: We extended the physical limits of the model to account for the best possible boundary conditions. North and south, the physical limits correspond to the sandstones crests. Since groundwater flow follows the topography in the sandstone aquifers, we supposed that the water divides are approximately along the sandstone crests and we imposed there a no-flow boundary condition. The Hoyoux River which imposes a base level to groundwater and flows east, allowed us to impose a hydraulic head value along the river. Only a few wells are present inside the Havelange calcareous valley.

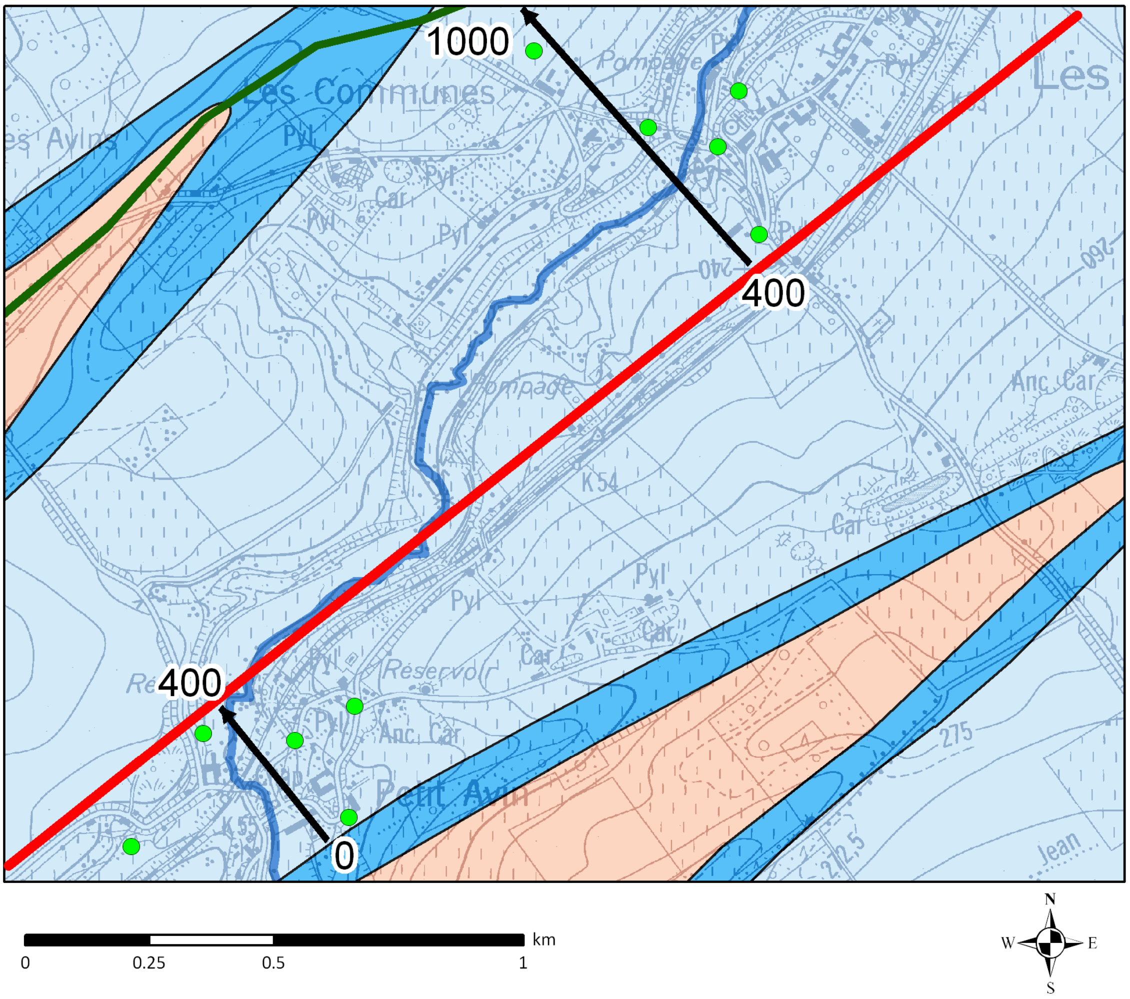

Figure 7.2: By projecting hydraulic head values on a plane (black line) perpendicular to the geological structures direction (red line), we can confirm that the Hoyoux River imposes a base level and therefore, that groundwater in the Havelange syncline flows toward the river (Figure 7.3).

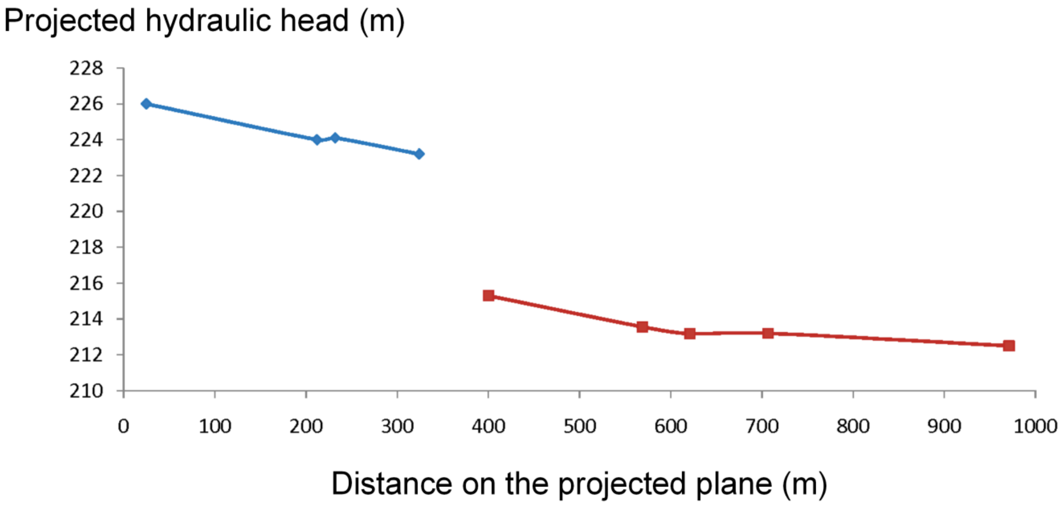

Figure 7.3: The projected hydraulic heads on a plane perpendicular to the geological structures direction (Figure 7.2) present a decrease from south to north, following the decrease of the Hoyoux River water level. As a consequence, the choice of imposing hydraulic head values along the eastern border of the model – the Hoyoux River – is validated by field data.

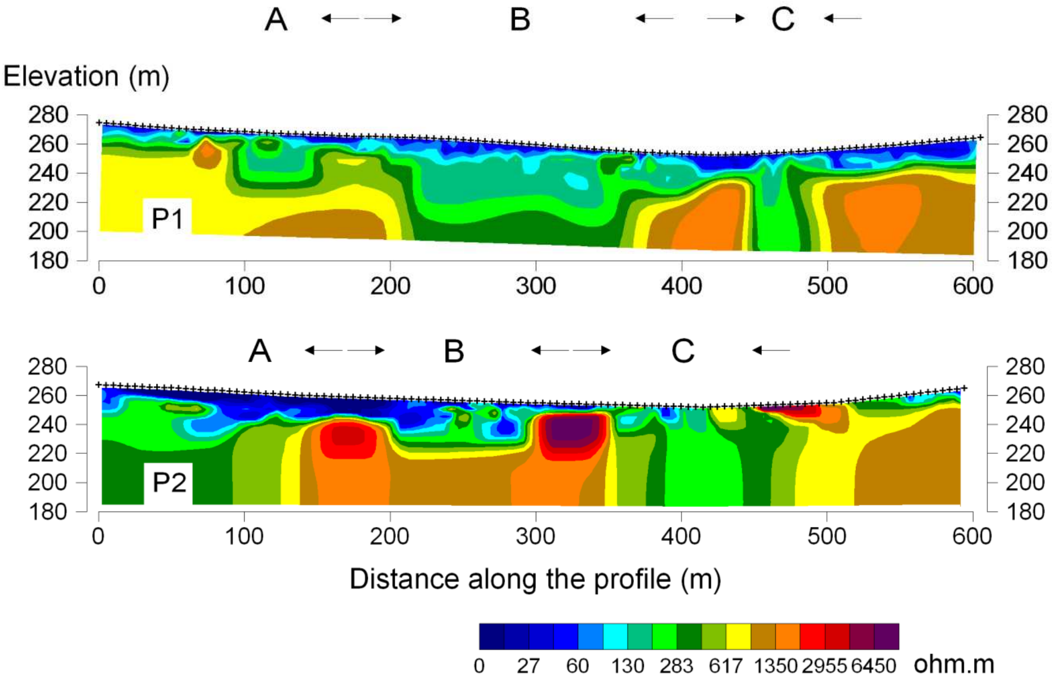

Figure 7.4: Two long parallel ERT profiles separated by 250 m, namely P1 and P2, were taken perpendicular to the geological structures direction. Both profiles present three more conductive zones – A, B, and C – interpreted as fractured areas of the limestone bedrock.

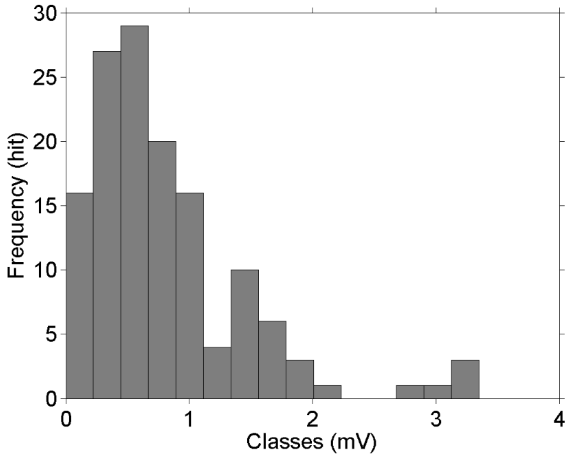

Figure 7.5: We acquired an SP profile along the ERT profile P1 and we measured three points per SP station. The SP error distribution shows a very low data noise level with maximum values around 3 mV whereas the SP signal ranges between -10 and 60 mV.

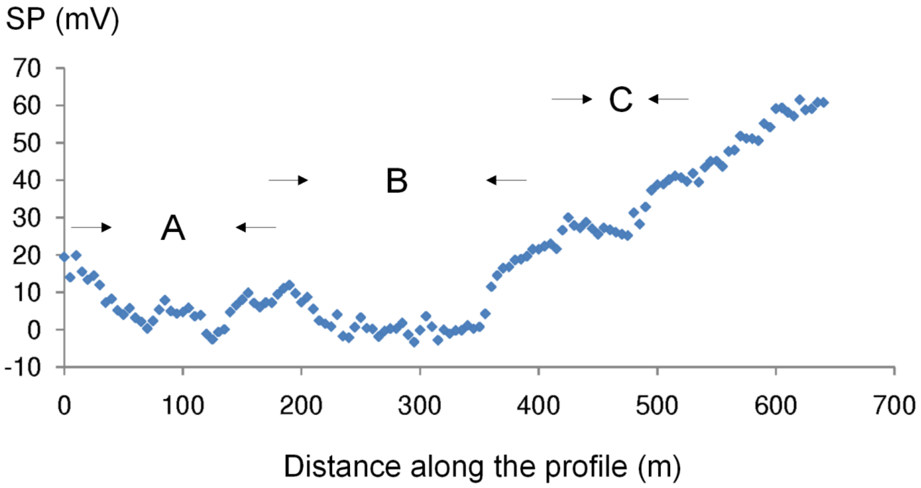

Figure 7.6: The SP signal acquired along profile P1 presents three strong anomalies that are well correlated with the A, B, and C electrical conductive zones found in the ERT inverted models (Figure 7.4). We interpreted these anomalies in terms of preferential groundwater flow paths. The SP signal decreases along the northern flank of the valley – from 0 to 70 m – and reaches a plateau in the center of the syncline – from 70 to 350 m – before increasing along the southern flank with a strong gradient. This behavior seems to be related with the hydraulic gradient related to the flanks of the syncline. The base electrode is located at 320 m along the profile.

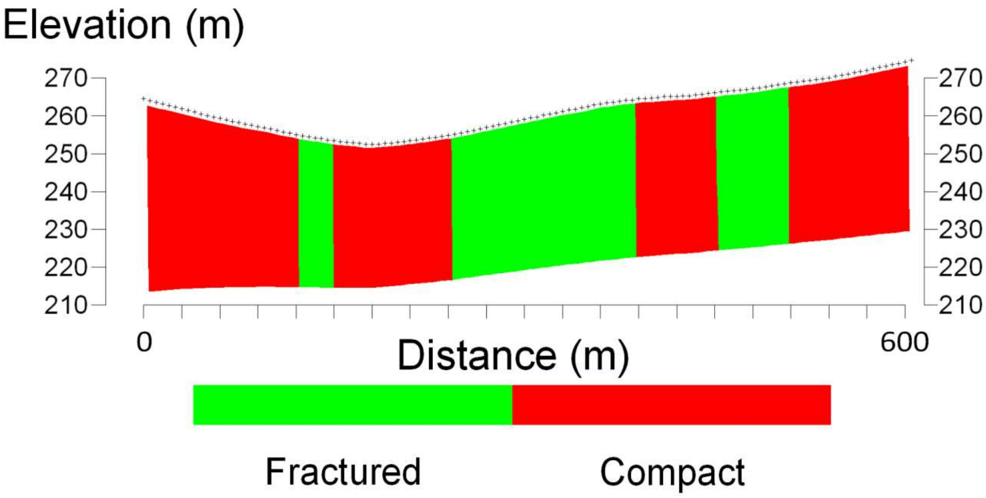

Figure 7.7: With the information gathered from both ERT profiles – the three more conductive areas, namely A, B, and C – as well as from the SP profile along P1 where zones A, B, and C are well correlated with strong SP anomalies, we decided to subdivide the limestone hydrogeological unit into several zones more or less fractured. Therefore, our conceptual groundwater flow model takes into account more hydraulically-active fractured units.

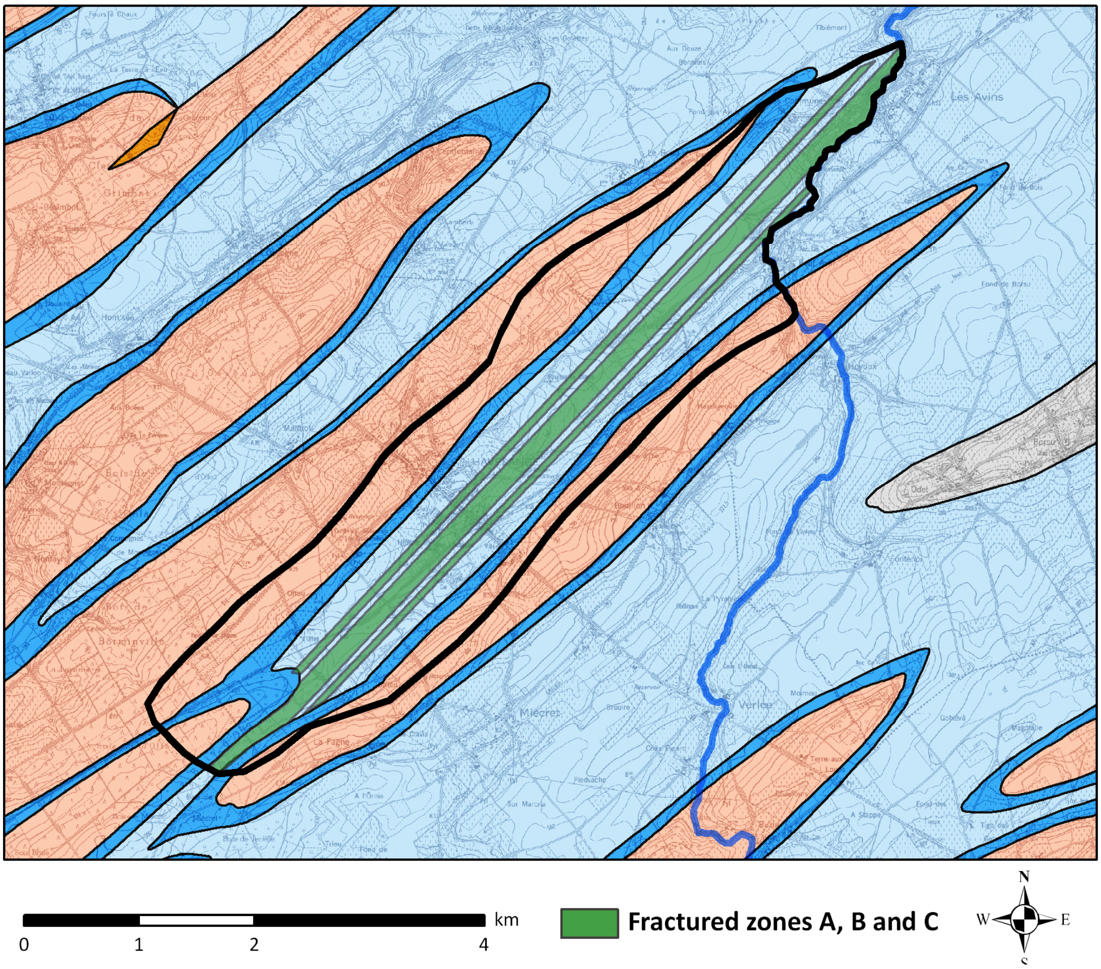

Figure 7.8: The three fractured limestone units A, B, and C were extended through all the syncline with the same direction as the one corresponding to the geological structures. This assumption is valid because we confirmed the fractured unit A with outcrops information from the Mercier quarry (see section 5.2).

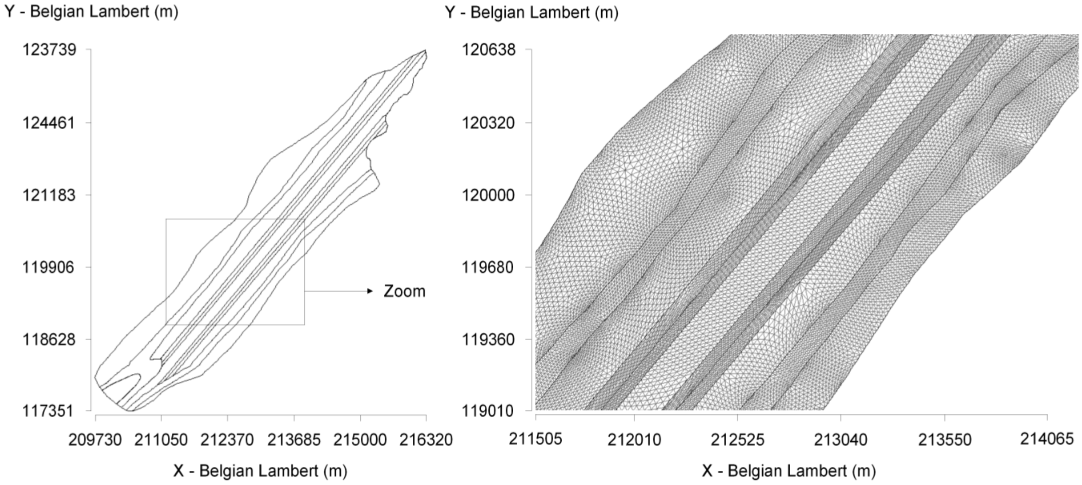

Figure 7.9: We used Grid Builder to create the finite-element mesh composed of just less than 94000 tetrahedral elements whose sides range between 5 to 10 m in the fractured areas and 20 to 40 m in more compact limestone units and the sandstone units, respectively.

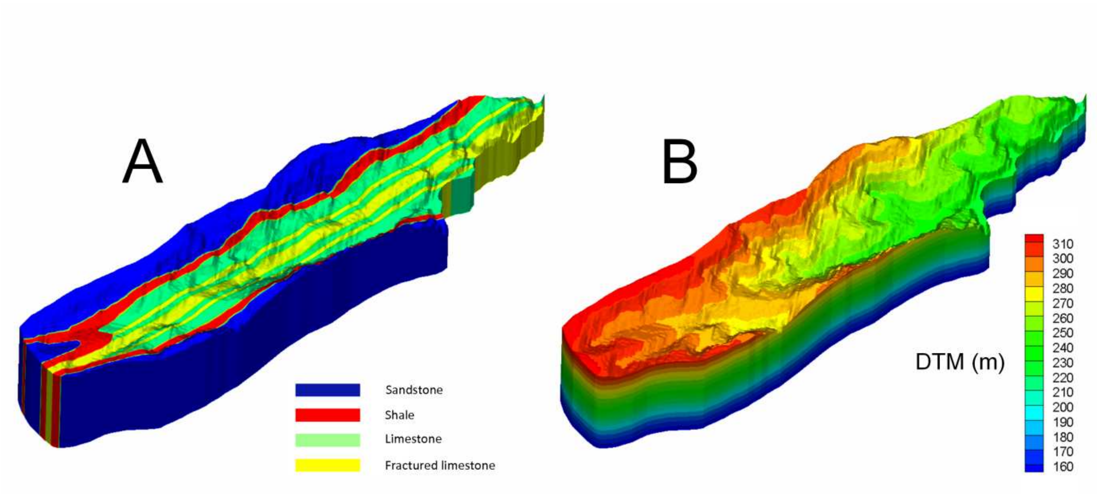

Figure 7.10: We used the digital terrain model (DTM) from the Walloon Region of Belgium, composed of a square mesh with values every 30 m, to incorporate the elevation into the grid (B). We extended the grid at depth to an elevation of 160 m which corresponds to a depth of about 100 m below surface. The model zonation, including the three fractured zones, is also presented (A).

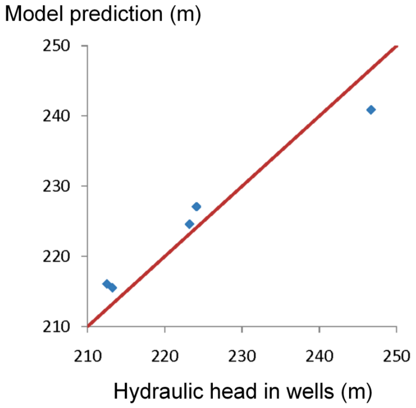

Figure 7.11: We used hydraulic heads measured in wells of the Havelange calcareous valley to precalibrate the groundwater flow model. To do this, we used PEST that allows an automatic calibration based on a standard smoothness-constraint. Without surprise, the model predictions for the four observation points situated near the Hoyoux River are imposed by the local boundary condition, where we imposed hydraulic head values along the river. The fifth observation, in piezometer F11, is well predicted by the model. The next step we carried out was to use the water table model applied to the SP signal measured along profile P1 to obtain new observation points for the model calibration.

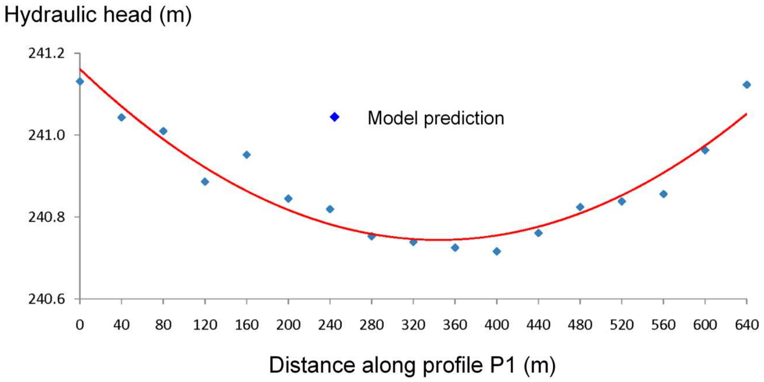

Figure 7.12: We added a few observation points along the ERT and SP profile P1 in order to visualize the water table distribution predicted by the model and then, to correlate it with the measured SP signal. Thus, we obtained interesting information about the SP apparent coupling coefficient. Indeed, the main trend (red line) corresponds well with the SP signal related to the southern flank of the valley but not for the northern flank (see Figure 7.13). However, the water table variation along this profile is quite low with a maximum value below 1 m. Therefore, our assumption concerning the streaming potential apparent coupling coefficient (C' = 2.7 mV/m) may be underestimated.

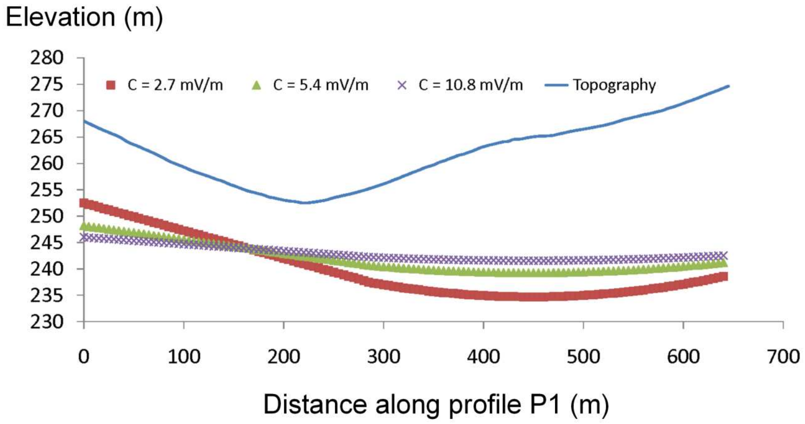

Figure 7.13: We tested several apparent coupling coefficients given the model predictions (Figure 7.12). We first doubled then quadrupled our initial guess (C’ = 2.7 mV/m) and we obtained results more in agreement with the model prediction with C’ above 10 mV/m. The difficulty of measuring this apparent coupling coefficient in the field is related to the lack or scarcity of useable piezometric information. Indeed, when two piezometers were close enough to perform SP measurements, the difference in hydraulic heads between both wells was generally very low (< 1 m). This is a consequence of the fact that these piezometers are generally close to water exploitation areas or near the Hoyoux River. The apparent coupling coefficient should therefore be included as another parameter to calibrate in the perspective of using the full SP signal as an additional source of calibration.

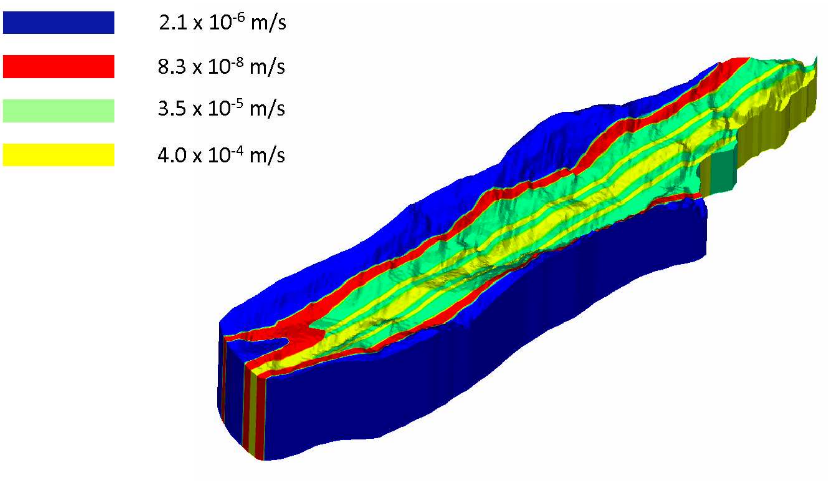

Figure 7.14: The precalibration using both piezometric heads and hydraulic heads estimated with the water table model (C' = 10.8 mV/m) applied to the SP signal measured along P1 gave physically-realistic units, close to what we expected. The fractured zones are more hydraulically-conductive than the other limestones units whereas the sandstones units present hydraulic conductivity values one order of magnitude lower than the limestones units. Finally, the shales units have very low hydraulic conductivity values, as expected.

References

Berkowitz, B., 2002, *Characterizing flow and transport in fractured geological media: A review*, Advances in Water Resources, 25 (8-12), 861-884.

Blessent, D., R. Therrien, and J.-M. Lemieux, 2011, *Inverse modeling of hydraulic tests in fractured crystalline rock based on a transition probability geostatistical approach*, Water Resources Research, 47 (12), W12530, doi:10.1029/2011WR011037.

Bolève, A., A. Revil, F. Janod, J. L. Mattiuzzo, and J. J. Fry, 2009, *Preferential fluid flow pathways in embankment dams imaged by self-potential tomography*, Near Surface Geophysics, 7 (5-6), 447-462.

Brouyère, S., A. Dassargues, G. Lorenzini, and P. Orban, 2009, Caractérisation hydrogéologique et support à la mise en œuvre de la Directive Européenne 2000/60 sur les masses d'eau souterraine en Région Wallonne (Projet Synclin'EAU), *délivrable D.6.1 - Description du modèle conceptuel des trois masses d'eau souterraine RWM011, RWM012 et RWM021*, Convention RW et SPGE-Aquapole.

Brouyère, S., A. Dassargues, J. Couturier, M. Leroy, and P. Orban, 2010, Caractérisation hydrogéologique et support à la mise en œuvre de la Directive Européenne 2000/60 sur les masses d'eau souterraine en Région Wallonne (Projet Synclin'EAU), *délivrable D.6.2 - Travaux de calibration et de validation des modèles d'écoulement et de transport de solutés développés pour les trois masses d'eau souterraine RWM011, RWM012 et RWM021*, Convention RW et SPGE-Aquapole (in French).

Day-Lewis, F. D., J. W. Lane, Jr., J. M. Harris, and S. M. Gorelick, 2003, *Time-lapse imaging of saline-tracer transport in fractured rock using difference-attenuation radar tomography*, Water Resources Research, 39 (10), 1290, doi:10.1029/2002WR001722.

Doherty, J., 2004, *PEST: Model-independent parameter estimation, user manual, version 5*, Watermark Numerical Computing, Brisbane, Australia.

Dorn, C., N. Linde, J. Doetsch, T. Le Borgne, and O. Bour, 2011, *Fracture imaging within a granitic rock aquifer using multiple-offset single-hole and cross-hole GPR reflection data*, Journal of Applied Geophysics, 78 (0), 123-132.

Eaton, T. T., 2006, *On the importance of geological heterogeneity for flow simulation*, Sedimentary Geology, 184 (3-4), 187-201.

Eaton, T. T., M. P. Anderson, and K. R. Bradbury, 2007, *Fracture Control of Ground Water Flow and Water Chemistry in a Rock Aquitard*, Ground Water, 45 (5), 601-615.

Graf, T., and R. Therrien, 2007, *Variable-density groundwater flow and solute transport in irregular 2D fracture networks*, Advances in Water Resources, 30 (3), 455-468.

Graf, T., and R. Therrien, 2008, *A test case for the simulation of three-dimensional variable-density flow and solute transport in discretely-fractured porous media*, Advances in Water Resources, 31 (10), 1352-1363.

Hancock, P. L., 1985, *Brittle microtectonics: principles and practice*, Journal of Structural Geology, 7 (3-4), 437-457.

Hao, Y., T.-C. J. Yeh, J. Xiang, W. A. Illman, K. Ando, K.-C. Hsu, and C.-H. Lee, 2008, *Hydraulic Tomography for Detecting Fracture Zone Connectivity*, Ground Water, 46 (2), 183-192.

Illman, W. A., and D. M. Tartakovsky, 2006, *Asymptotic Analysis of Cross-Hole Hydraulic Tests in Fractured Granite*, Ground Water, 44 (4), 555-563.

Jardani, A., A. Revil, A. Bolève, A. Crespy, J.-P. Dupont, W. Barrash, and B. Malama, 2007, *Tomography of the Darcy velocity from self-potential measurements*, Geophysical Research Letters, 34, L24403, doi:10.1029/2007GL031907.

Jardani, A., and A. Revil, 2009, *Stochastic joint inversion of temperature and self-potential data*, Geophysical Journal International, 179 (1), 640-654.

Krishnamurthy, N. S., D. Kumar, V. Ananda Rao, S. C. Jain, and S. Ahmed, 2003, *Comparison of surface and sub-surface geophysical investigations in delineating fracture zones*, Current Science, 84 (9), 1242-1246.

Le Borgne T., O Bour., J-R. De Dreuzy, P. Davy, and F. Touchard, 2004, *Equivalent mean flow models relevant for fractured aquifers: Insights from a pumping tests scaling interpretation*, Water Resources Research, 40, WO5112, doi:10.1029/2003WR002436.

Le Borgne T., O. Bour, F. L. Paillet, and J-P. Caudal, 2006a, *Assessment of preferential flow path connectivity and hydraulic properties at single-borehole and cross-borehole scales in a fractured aquifer*, Journal of Hydrology, 328 (1-2), 347-359.

Le Borgne, T., F. Paillet, L, O. Bour, and J-P. Caudal, 2006b, *Cross borehole flowmeter tests for transient heads in heterogeneous aquifers*, Ground Water, 44 (3), 444-452.

Lemieux, J.-M., R. Therrien, and D. Kirkwood, 2006, *Small scale study of groundwater flow in a fractured carbonate-rock aquifer at the St-Eustache quarry, Québec, Canada*, Hydrogeology Journal, 14 (4), 603-612.

Lemieux, J.-M., D. Kirkwood, and R. Therrien, 2009, *Fracture network analysis of the St-Eustache quarry, Quebec, Canada, for groundwater resources management*, Canadian Geotechnical Journal, 46 (7), 828-841.

McLaren, R. G., 2006, *GRID BUILDER, A pre-processor for 2-D, triangular element, finite-element programs*, Groundwater Simulations Group, University of Waterloo, Waterloo, Ontario, Canada.

Porsani, J. L., V. R. Elis, and F. Y. Hiodo, 2005, *Geophysical investigations for the characterization of fractured rock aquifers in Itu, SE Brazil*, Journal of Applied Geophysics, 57 (2), 119-128.

Revil, A., V. Naudet, J. Nouzaret, and M. Pessel, 2003, *Principles of electrography applied to self-potential electrokinetic sources and hydrogeological applications*, Water Resources Research, 39 (5), 1114, doi:10.1029/2001WR000916.

Revil, A., and P. Leroy, 2004, *Constitutive equations for ionic transport in porous shales*, Journal of Geophysical Research, 109 (B3), B03208, doi:10.1029/2003JB002755.

Revil, A., P. Leroy, and K. Titov, 2005, *Characterization of transport properties of argillaceous sediments: Application to the Callovo-Oxfordian argillite*, Journal of Geophysical Research, 110 (B6), B06202, doi: 10.1029/2004JB003442.

Robert, T., A. Dassargues, S. Brouyère, O. Kaufmann, V. Hallet, and F. Nguyen, 2011, *Assessing the contribution of electrical resistivity tomography (ERT) and self-potential (SP) methods for a water well drilling program in fractured/karstified limestones*, Journal of Applied Geophysics, 75 (1), 42-53.

Robert, T., D. Caterina, J. Deceuster, O. Kaufmann, and F. Nguyen, 2012, *A salt tracer test monitored with surface ERT to detect preferential flow and transport paths in fractured/karstified limestones*, Geophysics, 77 (2), B55-B67.

Rozycki, A., J. M. Ruiz Fonticiella, and A. Cuadra, 2006, *Detection and evaluation of horizontal fractures in earth dams using the self-potential method*, Engineering Geology, 82 (3), 145-153.

Straface, S., F. Carmine, S. Troisi, E. Rizzo, and A. Revil, 2007, *An Inverse Procedure to Estimate Transmissivity from Heads and SP Signals*, Ground Water, 45 (4), 420-428.

Suski, B., F. Ladner, L. Baron, F. D. Vuataz, F. Philippossian, and K. Holliger, 2008, *Detection and characterization of hydraulically active fractures in a carbonate aquifer: results from self-potential, temperature and fluid electrical conductivity logging in the Combioula hydrothermal system in the southwestern Swiss Alps*, Hydrogeology Journal, 16 (7), 1319-1328.

Titov, K. V., A. Levitski, P. K. Konosavski, A. V. Tarasov, Y. T. Ilyin, and M. A. Bues, 2005, *Combined application of surface geoelectrical methods for groundwater-flow modeling: A case history*, Geophysics, 70 (5), H21-31.

Therrien, R., R. G. McLaren, E. A. Sudicky, and S. M. Panday, 2005, *HydroGeoSphere. A three-dimensional numerical model describing fully-integrated subsurface and surface flow and solute transport*, Groundwater Simulations Group, University of Waterloo, Waterloo, Ontario, Canada.

Vasconcelos, I., and V. Grechka, 2007, *Seismic characterization of multiple fracture sets at Rulison Field, Colorado*, Geophysics, 72 (2), B19-B30.

Wishart, D. N., L. D. Slater, and A. E. Gates, 2006, *Self potential improves characterization of hydraulically-active fractures from azimuthal geoelectrical measurements*, Geophysical Research Letters, 33 (17), L17314, doi:10.1029/2006GL027092.

Wishart, D. N., L. D. Slater, and A. E. Gates, 2008, *Fracture anisotropy characterization in crystalline bedrock using field-scale azimuthal self potential gradient*, Journal of Hydrology, 358 (1-2), 35-45.

Wishart, D. N., L. D. Slater, D. L. Schnell, and G. C. Herman, 2009, *Hydraulic anisotropy characterization of pneumatic-fractured sediments using azimuthal self potential gradient*, Journal of Contaminant Hydrology, 103 (3-4), 134-144.

Yadav, G. S., and S. K. Singh, 2007, *Integrated resistivity surveys for delineation of fractures for ground water exploration in hard rock areas*, Journal of Applied Geophysics, 62 (3), 301-312.

8. Conclusions and perspectives

Fractured media constitute adequate drinking water exploitation areas but also potential contamination paths and their identification and characterization are important issues to consider. In this context, the aims of this study were to identify hydraulically-active fractured areas, to characterize them, and to monitor the dynamics of these systems (groundwater flow and solute transport) with the help of geophysics.

In this thesis, we addressed these objectives from a methodological and an experimental point of view at a scale representative of real world applications. These include the setup of new monitoring wells, the hydrogeological characterization of watersheds, and their hydrogeological modeling. Among the different geophysical methods, we chose to develop the electrical resistivity tomography (ERT) and the self-potential (SP) techniques, described in chapters 2 and 3, respectively. The joint use of both methods allows to image fractured areas (with ERT) and to discriminate hydraulically-active fractured zones from hydraulic barriers (with SP). These methods can also be easily setup for monitoring purposes, unlike electromagnetic methods.

The streaming potential theory, which links self-potentials and groundwater flow, was originally developed for porous media. Our primary focus at the beginning of this thesis was therefore to determine the type and magnitude of streaming potential anomaly associated with preferential flow path in fractured media. The geophysical survey presented in section 5.1 showed that a preferential groundwater flow in fractures created an SP anomaly of about -15 mV, centered on the preferential path. The survey conducted in section 5.1 investigated a shallow fractured quartzites aquitard and the targeted depth was less than 10 meters.

Following this successful result, we conducted a series of ERT and SP investigations (section 5.3) in the calcareous valleys of the Dinant Synclinorium situated in southern Belgium (described in details in chapter 4) at the scale of watersheds. Our measurements provided successfully suitable locations for installing monitoring piezometers in hydraulically-active fractured areas in regions with little hydrogeological information. We found that all wells drilled in more electrically conductive areas (resistivity contrast of about 1 to 10) and/or in negative SP anomalies (from -10 to -30 mV) presented high yields and inversely, that all wells drilled in more resistive areas (no resistivity contrast and resistivities > 1000 Ω.m) or outside SP anomalies were limited in terms of capacity. With this study, we confirmed that the joint use of ERT and SP offers great perspectives in terms of well positioning but not only, since we were also able to estimate the water table distribution along an SP profile.

Estimating the water table distribution from SP signals is certainly an interesting research topic but studying the seasonal dynamics of watersheds with an SP monitoring is much more challenging. We focused our research on the southern flank of a particular calcareous valley (section 6.1). The measured SP signals and a one-year hydraulic head monitoring showed that during low groundwater level periods, the hydraulic and SP gradients related to the southern flank of the valley decrease and inversely, that they increase again during high groundwater level periods. Even if this correlation between the magnitudes of the hydraulic and SP gradients is, at this stage, only qualitative, it offers the possibility to better understand groundwater flow systems along long transects where hydrogeological data can be scarce.

In general, the results of tracer tests strongly depend on the monitoring network available and on the injection strategy. In fractured and/or karstified geological media, conducting classic tracer tests may be a very difficult task if prior information about the preferential paths locations or about the flow and transport rates is not known. In section 6.2, we adapted an existing methodology (up to now, only tested in relatively shallow and homogeneous or layered aquifers) that consists in monitoring a salt tracer test with surface-ERT to obtain the necessary information needed to conduct classic tracer tests in complex fractured systems. The experiment was conducted in a highly fractured and karstified calcareous valley. We faced multiple challenges including our working scale, the lower resolution and depth of investigation of surface ERT compared to crosshole ERT, the inherent smoothing of ERT, and the finite time that is needed to complete the acquisition of an entire sequence. Nevertheless, we were able to image a preferential flow path where a rapid transport (> 10 m/h) occurs through a deep fractured zone (±20 m). This specific study offers great perspectives. Indeed, one can imagine to use more systematically this methodology prior to classic tracer tests to set up efficient monitoring wells and to obtain a prior estimation of flow rates, ideal for optimizing sampling rates.

From a methodological point of view, we performed a numerical benchmark to compare different resolution indicators for electrical tomography, namely the DOI index, the cumulative sensitivity matrix, and the diagonal values of the resolution matrix, in order to appraise the quality of ERT images (section 5.4). We found that the analysis of the cumulative sensitivity matrix and the diagonal values of the resolution matrix led to the best estimation of the depth of investigation. Using these quantities, it was possible to find a cutoff for the cumulative sensitivity values or the diagonal values of the resolution matrix below which the inverted resistivity values do not depend on the surface data anymore, and this in a more straightforward and objective way than using the DOI approach.

To use resolution indicators with real data, we considered two different schemes. The first one is based on ground truth information by using an EM39 log and comparing it to an extracted ERT log. We used the cumulative sensitivity value at the depth where both logs diverge as a cutoff. This approach worked well in the case of the salt tracer experiment because a piezometer was available to conduct EM39 measurements (section 6.2). The second approach consisted in considering the inverted resistivity model as a true synthetic model. A new synthetic data set which resembles the real one – same acquisition sequence – is simulated and then inverted with the same parameters as the real case study. The comparison of this inverted model with the true synthetic model leads to the estimation of the cutoff. This scheme worked remarkably well in the case of a long roll-along profile acquired in the Havelange calcareous valley (section 5.4). Practitioners should systematically appraise the quality of their electrical images (and more generally, all inverted models) in order to only physically interpret the parts of the inverted models that are associated with the measured data.

The synthetic case study (section 5.4) was further exploited to compare different model constraints, namely the standard smoothness-constraint, the blocky inversion, and the minimum-gradient-support (MGS) approach, to best image the sharp limits that exist between fractured areas and compact limestones (as seen in section 5.2). We found, as expected, that both the blocky inversion and the MGS regularization technique outperformed the smoothness-constraint when sharp limits are present in the electrical structures. In the case of section 5.3, those focused inversion techniques were helpful because they allowed a better positioning of the wells. Nevertheless, the choice of a particular regularization technique must always be guided by the prior information we have. Otherwise, misinterpretations of the resulting images are clearly possible.

Noise reduction and data error characterization is a crucial part in data inversion, including in time-lapse ERT inversion. In section 6.4, we demonstrated that an underestimation of the noise level can lead to the presence of strong artifacts that may mask the subsurface process that is monitored or even worse, induce wrong interpretations on the hydrodynamics. This was especially true when inverting the measured resistances as data (independent and cascaded inversions). In contrary, we showed that inverting the resistances differences always resulted in the correct positioning of the preferential path, no matter the chosen error model. However, the noise underestimation still led to numerous artifacts whereas its overestimation resulted in extremely smoothed, but still focused, anomalies.

We also demonstrated in section 6.4, that time-lapse reciprocal errors depend on the mean measured resistances, and in some cases, not taking this into account may lead to physically unrealistic results. To our knowledge, few to no studies pointed this important fact out. As a consequence, we would like to recommend the systematic collection of the reciprocal measurements (or a subset of them) since they serve as a basis for noise characterization.

Noise characterization is primordial in time-lapse inversion and may supplant the choice of the model constraint or the inversion scheme, especially with independent or cascaded inversions. Once the noise level is correctly chosen, focused model constraints, such as applying the MGS approach in data difference inversion, can further improve the time-lapse images (section 6.4). However, a full scan of the β values is still needed to fully benefit the full power of the MGS approach.

The last objective of this study was to gather all the information we acquired on the Havelange calcareous valley in order to build a conceptual groundwater flow model and then, to precalibrate it (chapter 7). We showed that the use of ERT and SP could strongly improve the conceptual model because they allowed us to take large hydraulically-active fractured zones into account. We also pointed out that the use of SP measurements could be useful to calibrate groundwater flow model (section 7.2). Indeed, we found a good correlation between the simulated heads and the estimated heads obtained using the water table model. However, further experiments, either in laboratory or in the field, are necessary to better estimate the streaming potential apparent coupling coefficient.

The use of geophysical data and particularly SP signals as an additional source of calibration is a great perspective of this work. We are currently working in that direction by implementing the streaming potential governing equation into the HydroGeoSphere (HGS) model. Thus, HGS should be able to simulate streaming potentials given a set of electrical parameters and the groundwater fluxes. Incorporating this routine with PEST will hopefully allow the automatic calibration of the model with both measured hydraulic heads and SP measurements in the near future. This approach could lead to other perspectives such as using SP time-series (e.g., from seasonal or pumping tests monitoring) in order to calibrate groundwater flow model for transient flow.